A DOUBLE LAYER-AVERAGED MODEL FOR STRATIFIED SEDIMENT-LADEN FLOW IN OPEN CHANNELS

JI LI

Submitted for the degree of Doctor of Philosophy

Heriot-Watt University

School of Energy, Geoscience, Infrastructure & Society

October 2016

ABSTRACT

Sediment-laden flows in open channels can be sharply stratified vertically, characterized by a double-layer flow structure composed of a subaqueous sediment-laden flow layer immediately over the bed and an upper clear-water flow layer. Typical examples include dam-break flows and reservoir sediment-laden flows featuring turbidity currents. In general, sharply stratified sediment-laden flows involve a number of physical factors, including sharp flow stratification, inter-layer exchange, active sediment transport, and substantial mass exchange with the bed. Double layer-averaged models are attractive in modelling such flows in connection to its vertical structure. However, existing double layer-averaged models have either partly or completely ignored the primary features of stratified open-channel sediment-laden flows and thus are not generally suitable. In the present thesis, a two-dimensional double layer-averaged model has been developed, explicitly incorporating the fundamental physical factors and therefore generally applicable for sharply stratified sediment-laden flows in open channels. First, the governing equations of the new model and the employed numerical algorithm are presented. Then, the model is applied to investigate mobile-bed dam-break flows due to instantaneous full dam break and progressive failure of a dike and landslide dams. Enhanced performance of the new model is demonstrated over the previous models. Most notably, it clearly justifies the physical necessity to incorporate sediment mass conservation. Next, the proposed model is applied to investigate reservoir sediment-laden flows featuring turbidity currents. The model is benchmarked against turbidity currents due to lock-exchange and sustained inflow. It is revealed that an appropriate clear-water outflow is favorable for turbidity current propagation, and also conducive to improving sediment flushing efficiency. As applied to prototype-scale turbidity current in the Xiaolangdi Reservoir in the Yellow River, China, the model successfully resolves the whole process from formation to recession. Following that, the hyperbolicity of the model equations is analyzed as related to dam-break flows and reservoir turbidity currents. The present model is demonstrated to preserve hyperbolicity and thus avoid Kelvin-Helmholtz instability. Computational tests for reservoir turbidity currents reveal that an excessive clear-water outflow would keep the turbidity current from being spoiled, and improves sediment flushing efficiency correspondingly.

ACKNOWLEDGEMENT

Rather than a personal accomplishment and a nice textbook, a thesis is a process, an adventure largely grounded on a network of influences and relationships, that provided motivation, inspiration and help in profusion. Special thanks should be addressed to a series of people that guided or accompanied me during the thesis.

First I wish to deeply thank Professor Zhixian Cao and Professor Gareth Pender, the supervisors of this work, for giving me the opportunity to conduct this research and also for providing expert guidance and precise feedback throughout the research. The confidence and enthusiasm they devote to me, and their great openness to international collaborations and networking, are greatly appreciated.

Thanks are also addressed to my friends and colleagues from Heriot-Watt University and Wuhan University. Their never-ending support and advice made the research journey a joy on a daily basis.

Support from Institute for Infrastructure and Environment of Heriot-Watt University through a PhD Scholarship, which fundraised my study in the last three years, is gratefully acknowledged.

Finally, I would express my deepest gratitude to my parents and girlfriend Hanwen Sun, for their patience, love and encouragement.

ACADEMIC REGISTRY
Research Thesis Submission

Name*:*	JI LI		
School/PGI:	School of Energy, Geoscience, Infrastructure and Society		
Version: *(i.e. First, Resubmission, Final)*	Final	Degree Sought (Award **and** Subject area)	PhD, Civil Engineering

Declaration

In accordance with the appropriate regulations I hereby submit my thesis and I declare that:

1) the thesis embodies the results of my own work and has been composed by myself
2) where appropriate, I have made acknowledgement of the work of others and have made reference to work carried out in collaboration with other persons
3) the thesis is the correct version of the thesis for submission and is the same version as any electronic versions submitted*.
4) my thesis for the award referred to, deposited in the Heriot-Watt University Library, should be made available for loan or photocopying and be available via the Institutional Repository, subject to such conditions as the Librarian may require
5) I understand that as a student of the University I am required to abide by the Regulations of the University and to conform to its discipline.

* *Please note that it is the responsibility of the candidate to ensure that the correct version of the thesis is submitted.*

Signature of Candidate*:*		Date:	

Submission

Submitted By *(name in capitals):*	JI LI
Signature of Individual Submitting:	
Date Submitted:	

For Completion in the Student Service Centre (SSC)

Received in the SSC by *(name in capitals):*			
Method of Submission *(Handed in to SSC; posted through internal/external mail):*			
*E-thesis Submitted (**mandatory for final theses)***			
Signature:		Date:	

CONTENT

LIST OF TABLES

LIST OF FIGURES

GLOSSARY

DL	double layer-averaged model (Li et al. 2013; Cao et al. 2015)
MUSCL	monotonic upstream-centered scheme for conservation laws
SDL	simplified double layer-averaged (SDL) model (Spinewine 2005a).
SL	single layer-averaged model (Cao et al. 2004)
HLLC	Harten-Lax-van Leer Contact Wave approximate Riemann solver (Toro 2001)
SS	a single system
RS	two reduced-order hyperbolic systems

NOTATIONS

Symbol	*Definition*	*First use*
$\mathbf{A}$	matrix in Eq. (6.3)	Section 6.1
$\mathbf{E}$, $\mathbf{F}$, $\mathbf{G}$, $\mathbf{H}$	flux variables	Section 2.4
$\mathbf{R}_b$	interface slope source term	Section 2.4
$\mathbf{R}_f$	interface friction source terms and other terms related to impacts of water entrainment	Section 2.4
$\mathbf{R}_e$	water entrainment source term and variations of interface elevation	Section 2.4
$\mathbf{S}_b$	bed slope source term	Section 2.4
$\mathbf{S}_f$	bed friction source terms and other terms related to the impacts of sediment transport and water entrainment	Section 2.4
$\mathbf{S}_e$	water entrainment source term	Section 2.4
subscripts i, j	spatial node indexes	Section 2.4
subscript m	time level and subscripts	Section 2.4
subscript q	the state after calculating the variables from Eq. (2.37);	Section 2.4
Superscripts L and R	left and right of an edge of two neighbouring cells	Section 2.4
C_b	volumetric sediment concentration of the bed	Section 2.1
c_{bk}	size-specific local near-bed concentration	Section 2.3
c_k	size-specific volumetric sediment concentration of the turbidity current layer	Section 2.2
C_s	total volumetric sediment concentration of sediment-laden flow layer	Section 2.1
d_k	the diameter of the k th size of multi grain sizes of sediments	Section 2.2

E_k , D_k	size-specific sediment entrainment and deposition flux	Section 2.2
E_T , D_T	total sediment entrainment and deposition fluxes respectively	Section 2.1
E_w	mass exchange flux of clear water between the upper and lower layers	Section 2.1
E_{sk}	size-specific near-bed concentration at capacity condition	Section 2.3
E_{sku}	sediment capacity transport for uniform sediment	Section 2.3
e_b	bed erosion rate	Section 2.2
e_w	water entrainment coefficient	Section 2.3
F_{Gs}	pressure force for the sediment-laden flow layer	Section 2.4
F_{Gw}	pressure force for the clear-water flow layer	Section 2.4
F_P	densimetric Froude number at plunge point	Section 4.2
F_{Ps}	downstream gravitational force for the sediment-laden flow layer	Section 2.4
F_{Pw}	downstream gravitational force for the clear-water flow layer	Section 2.4
F_k	areal exposure fraction of the k th sediment on the bed surface	Section 2.3
f_{ak}	fraction of the k th size sediment in the active layer	Section 2.2
f_{Ik}	fraction of the k th size sediment in the interface between the active layer and substrate layer.	Section 2.2
f_{sk}	fraction of the k th size sediment in the substrate layer	Section 2.3
g	gravitational acceleration	Section 2.2
h_p	current thickness at the plunge point	Section 4.2
h_s	depth of sediment-laden flow layer	Section 2.1
h_w	depth of clear-water flow layer	Section 2.1
L_{st}^1 , L_{in}^1 , L_{bd}^1	norms for stage, interface and bed deformation depth respectively.	Section 3
n_w	roughness at the interface between the sediment-laden flow layer and	Section 2.3

	clear-water flow layer	
n_b	bed roughness	Section 2.3
p	bed sediment porosity	Section 2.2
q_{bk}	size-specific unit-width bedload transport rate at transport capacity status	Section 2.3
q_{wx}, q_{wy}	conservative variables in Eq. (2.35);	Section 2.4
q_{sx}, q_{sy}, q_{ck}	conservative variables in Eq. (2.36).	Section 2.4
Ri	Richardson number	Section 2.3
r_{bk}	ratio of the near-bed sediment concentration and layer-averaged concentration	Section 2.3
s	specific gravity of sediment	Section 2.3
t	time	Section 2.2
$\overline{U}_s$	resultant velocity of the sediment-laden flow layer	Section 2.3
$\overline{U}_{ws}$	resultant velocity difference between the two layers	Section 2.3
u_*, v_*	are the bed shear velocities in the x - and y - directions	Section 2.3
u_s	layer-averaged velocity of sediment-laden flow layer in $x-$direction	Section 2.1
u_w	layer-averaged velocity of sediment-laden flow layer in $x-$direction	Section 2.1
v_w	layer-averaged velocities of clear-water layer in the y - directions	Section 2.2
v_s	layer-averaged velocities of turbidity current layer in the y -directions	Section 2.2
V_{si}	bulk sediment volume input from the inlet of the reservoir	Section 4.3
V_{so}	bulk sediment volume carried away through the downstream boundary	Section 4.3
$V_{sc}(t)$	the volume of the sediment contained within the flow	Section 5.1
$V_{sb}(t)$	the volume of the sediment due to bed erosion or deposition	Section 5.1
w^+, w^-, s^+,	the eigenvalues associated with the Jacobian matrix	Section 6.1

s^- , λ_s		
x_p	distance between the plunge point and flume entrance	Section 4.2
x , y	horizontal coordinate	Section 2.2
z_b	bed elevation	Section 2.1
Δt	time step	Section 2.4
Δx , Δy	spatial steps;	Section 2.4
Δz_b	bed deformation depth	Section 3
α_k	correction coefficient	Section 2.3
ϕ_k	modification coefficient	Section 2.3
φ	slope-limited function evaluated at cell (i, j)	Section 2.4
η	stage	Section 2.1
η_s	elevation of the interface between sediment-laden flow layer and clear-water flow layer	Section 2.1
ν	kinematic viscosity of water	Section 2.3
θ	Shields parameter	Section 2.3
θ_{ck}	size-specific threshold Shields parameter for initiation of sediment movement	Section 2.3
ρ_c , ρ_0	densities of water-sediment mixture and saturated bed	Section 2.2
τ_{ix} , τ_{iy}	shear stresses at the interface between the clear-water layer and sediment-laden flow layer in the x- and y- directions	Section 2.2
τ_{bx} , τ_{by}	bed shear stresses in the x- and y- directions	Section 2.2
ω_k	size-specific settling velocity	Section 2.3
Φ	logical parameter	Section 6.1
δ	the thickness of the active layer	Section 2.2

ξ	elevation of the bottom surface of the active layer	Section 2.2

LIST OF PUBLICATIONS

Publications related to this thesis:

1. **Li, J**., Cao, Z., Pender, G., and Liu, Q. (2013). A double layer-averaged model for dam-break flows over mobile bed. *Journal of Hydraulic Research*, *51*(5), 518-534.

2. Cao, Z., **Li, J**., Pender, G., and Liu, Q. (2015). Whole-process modeling of reservoir turbidity currents by a double layer-averaged model. *Journal of Hydraulic Engineering*, *141*(2), 04014069.

3. **Li, J**., Cao, Z., Pender, G., and Liu, Q. (2015). Hyperbolicity analysis of a double layer-averaged model for open-channel sediment-laden flows. SCIENCE CHINA Physics, Mechanics & Astronomy, 45(10), 104705. (in Chinese)

CHAPTER 1 INTRODUCTION

1.1. Sharply Stratified Sediment-laden Flows

Sediment-laden flows, which commonly occur in surface water environments, can be sharply stratified vertically, characterized by a double-layer flow structure composed of subaqueous sediment-laden flow layer immediately over the bed and an upper clear-water layer. Typical examples include the flows induced by dam-break flows and reservoir turbidity currents in open channels, and marine hyperpycnal plumes at river mouth respectively.

Dam break flows are usually highly powerful and capable of triggering active sediment transport and rapid morphological changes, which in turn conspire to modify the flood. In general, strong interactions exist among the flow, sediment and morphology. Through friction, inertial effects and momentum exchanges with the fluid phase, erosion and deposition of bed materials may in turn significantly affect the development of the flood wave in terms of arrival time of the wave front and envelope of maximum attained flood levels, two parameters of utmost importance for emergency planning, risk management and damage assessment. Indeed damages to property and infrastructure resulting directly from sediment erosion, transport and deposition may even be much more serious than those resulting from the water flooding itself. Notably, the amount of sediment material entrained by catastrophic floods due to dam break or dyke failures may be extremely huge (Costa and Schuster 1988; Brooks and Lawrence 1999; Capart 2000), sometimes the same order of magnitude as the initial volume of water in the reservoir. Consequently, the eroded sediments are observed to move collectively as a dense sheet of contact load, occupying a significant portion of the flow depth (Sumer et al. 1996) and thus forming the subaqueous sediment-laden flow layer. In this regard, dam-break induced sediment-laden flows can be sharply stratified, comprising a bedload sediment-laden flow layer immediately over the bed and an upper clear-water flow layer.

Reservoir turbidity current is subaqueous sediment-laden underflow. It is formed when subaerial sediment-laden flow plunges into a reservoir. Like other gravity currents, it is driven by the density difference with respect to the ambient fluid. Obviously, the sediment-laden flows in open channels induced by turbidity currents are sharply stratified, comprising the subaqueous turbidity current layer and the upper clear-water layer. More importantly, the whole process of reservoir turbidity current, i.e., formation, propagation and recession, is generally controlled by the water and sediment inputs from upstream and also the reservoir operational scheme specifying the downstream boundary condition. In this sense, reservoir turbidity currents are distinct from self-accelerating turbidity currents in ocean environments (Parker et al. 1986). In general, turbidity currents can travel remarkable distances carrying large amounts of suspended sediments from the plunge point to the downstream. In reservoirs, turbidity currents are often the governing processes for the transport, entrainment and deposition of sediment (Fan and Morris 1992a). If the turbidity currents manage to arrive at the dam, it will be possible to flush sediment out of the reservoir. Otherwise, severe sedimentation in the reservoir will generally occur. Enhanced understanding of the whole process of reservoir turbidity currents is significant to effective sediment and reservoir management, flood mitigation and fish habitat recovery.

Marine hyperpycnal plume (underflow) is a particular kind of turbidity current flowing under the seawater. It is normally formed at river mouth when the turbid river water, with both high suspended sediment concentrations and varying degrees of mixing with saltwater, enters and then plunges into the seawater with the relatively smaller density. Associated with high-suspended concentrations, hyperpycnal underflows can transport considerable volume of sediments to the ocean basins (Mulder et al. 2003). Such underflows are rare at the mouths of most rivers; however, the extremely high suspended sediment concentrations which issue from the mouth of Yellow River in China are sufficient to favor the occurrence of hyperpycnal underflows for most of the year, which indeed have been considerably investigated (e.g., Wright et al. 1986, 1988, 1990; Li et al. 1998)

The present thesis is mainly focused on two typical types of stratified sediment-laden flow in open channels, featuring dam-break flows and reservoir turbidity currents. Before proceeding, the following definitions in relation to the stratified sediment-laden flow in open channels need to be clarified. First, the buoyancy force for the subaqueous sediment-laden flow is negative, namely towards the bed. Therefore, it demonstrates that the subaqueous sediment-laden flow layer is moving immediately over the bed, which is clearly different from positive buoyance force-driven subaqueous sediment-laden flows (Sequeiros et al. 2009b; Gladstone and Pritchard 2010). Second, the open-channel flow is stratified resulting from the density difference only due to sediment. The present research objective is only a subset of stratified open-channel flows, in which the density excess may be caused by salinity or temperature (Simpson 1997; Huppert 2006). Accordingly a primary feature of the subaqueous sediment-laden flow is its non-conservative nature. This is because subaqueous sediment-laden flow may entrain or deposit sediment, which correspondingly increases or reduces its density and the driving force. Third, the flow region with either low or high sediment concentration can be regarded as subaqueous sediment-laden flow layer in the present study. Thus the upper clear-water layer is merely composed of pure water and the subaqueous sediment-laden flow layer consists of water-sediment mixture. Fourth, the subaqueous sediment-laden flow layer behaves as an effective median with little slip between the upper clear-water layer and the lower erodible bed, and negligible seepage between fluid and solid phases. Based upon the above considerations, interactions exist among two layers and erodible bed. Specifically, the upper layer interacts with the lower layer by exchanging clear water, but the lower layer exchanges both water and sediment with the erodible bed. In general, sharply stratified sediment-laden flows involve a number of primary physical factors, including sharp flow stratification, inter-layer exchange, active sediment transport, and substantial mass exchange with the bed, the bottom boundary that usually undergoes evolution.

1.2. Shallow Water Hydro-sediment-morphodynamics Models

Enhanced understanding of sharply stratified sediment-laden flows and the linked hydro-sediment-morphodynamics has become extremely significant in the fields of water resources, environment protection, ecology management and public safety, given the frequent occurrence of the generally catastrophic floods worldwide. In the past decades, mathematical modelling has become one of the most proactive approaches for improving understanding of sharply stratified sediment-laden flows. In general, there have been two categories of computational models for sharply stratified sediment-laden flows, i.e., depth-resolving models and shallow water (layer-averaged) models. Depth-resolving models, including full three-dimensional and vertical two-dimensional models, can reproduce the evolution process and the vertical structure of sharply stratified sediment-laden flows, induced by dam-break flows (Özgökmen 2007; Hsu et al. 2014; Marsooli and Wu 2014) and turbidity currents (e.g., Bournet et al. 1999; De Cesare et al. 2001; Kassem and Imran 2001; Kassem et al. 2003; Khan et al. 2005; Huang et al. 2007, 2008; Georgoulas et al. 2010; An and Julien 2014). Nevertheless, depth-resolving models require excessively high computational costs and thus are unrealistic for applications to prototype-scale problems such as reservoir turbidity currents in the Xiaolangdi Reservoir. This holds true for general three-dimensional models for fluvial flow and sediment transport (Fang and Wang 2000; Wu et al. 2000). Also, the physics of turbulence, on which the model closures are based, is still poorly understood. In particular, it remains far from clear how to incorporate the effects of sediment into turbulence closures, even for steady and uniform sediment-laden flows in open channels. Comparatively, shallow water (layer-averaged) hydro-sediment-morphodynamics models are easier to formulate and solve, featuring a sensible balance between theoretical integrity and applicability. Layer-averaged refers to the fact that the physical quantities (velocity and sediment concentration) are averaged along the thickness of the sediment-laden flow layer and clear-water layer.

Most shallow water hydro-sediment-morphodynamics models for dam-break flows to date are single layer-averaged models based on conventional shallow water hydrodynamic principles (e.g., Capart and Young 1998; Cao et al. 2004; Leal et al. 2006; Wu and Wang 2007; Leal et al. 2010a, b; Xia et al. 2010), in which the whole water-sediment mixture is regarded as a single layer. Indeed they performed rather well and achieved satisfactory results in modelling dam-break flows. However, dam-break induced sediment-laden flows can be distinctly stratified, comprising a bedload sediment-laden flow layer immediately over the bed and an upper clear-water flow layer, which was first observed by Capart (2002) and thus gave rise to the awareness of developing double layer-averaged model for dam-break flows.

Likewise, most existing layer-averaged models for turbidity currents are also single layer-averaged models, in which only the subaqueous sediment-laden flow layer is modelled, however the upper clear-water flow is neglected (e.g., Fukushima et al. 1985;

Parker et al. 1986; Choi 1998; Bradford and Katopodes 1999a, b; Sequeiros et al. 2009a; Hu et al. 2012; Lai and Wu 2013). Thus they are restricted to modelling the propagation of turbidity currents after their formation. In applications, this category of models hinges upon observed data to specify the upstream boundary conditions (e.g., Hu et al. 2012), which however are not generally available. And indeed, there have been modelling efforts to resolve the formation of turbidity currents (Kassem and Imran 2001; De Cesare et al. 2001; Georgoulas et al. 2010). Critically, single layer-averaged models cannot resolve the formation process characterized by the transition from subaerial open-channel sediment-laden flow to subaqueous turbidity current, or the upper clear-water flow dictated by the operation scheme of the reservoir. In contrast to these limitations, it is fundamentally important to resolve the formation process of reservoir turbidity current, not only scientifically but also practically. Equally importantly the operation scheme of the reservoir has been found to have significant impacts on turbidity currents (Lee and Yu 1997).

Given the above observations, double layer-averaged models hold great promise for analysing sharply stratified sediment-laden flows by resolving the subaqueous sediment-laden flow layer and the upper clear-water flow layer distinctly based on their respective mass and momentum conservation laws.

1.3. Double Layer-averaged Models

Indeed double layer-averaged modelling of sharply stratified sediment-laden flows in open channels is not new at all in the broad field of fluid dynamics. As underpinned by the vertically stratified structure, extensive double layer-averaged models have been proposed for dam-break flows (Fraccarollo and Capart 2002, Capart and Young 2002, Spinewine 2005a, b, Savary and Zech 2007, Zech et al. 2008) and for general gravity currents (Rottman and Simpson 1983; Bonnecaze et al. 1993; Hallworth et al. 2003;

Ungarish and Zemach 2005; Adduce et al. 2012; La Rocca et al. 2012). This is sensible because of the significantly reduced computing cost compared to a vertical two-dimensional (2D) or full three-dimensional (3D) model that fully resolves the vertical flow structure and also the ability to represent reasonably the stratification that is normally ignored in a single layer-averaged (SL) model. Generally, two sets of layer-averaged equations are deployed to describe respectively the lower sediment-laden flow layer and the upper clear-water flow layer. However, the developments and applications of double layer-averaged models for sharply stratified sediment-laden flows have remained in infancy to date, suffering from several major shortcomings.

First, existing double layer-averaged models for dam-break flows are simplified because sediment concentration in the bedload transport layer is presumed constant. For the highly transient and varied dam-break flows, this assumption may be far from generally justified. In principle, sediment concentration is one of the unknowns to be solved by a numerical model, but in existing simplified double layer-averaged (SDL) models (Spinewine 2005a, b, Savary and Zech 2007, Zech et al. 2008, Zech et al. 2009), its value needs to be specified beforehand and thus uncertainty is introduced inevitably. Succinctly, from a physical point of view, the fundamental mass conservation law for sediment is violated. The consequence of this fact can be serious. For example, according to Fraccarollo and Capart (2002), sediment particle size would have no effect on the bed scour induced by dam-break flows, which is questionable from physical intuition. Most plausibly, this stems from the assumption of constant sediment concentration, though the impact of the assumed equal velocities of the two layers is not precluded. Indeed, the extended models by for instance Capart and Young (2002), Spinewine (2005a) and Zech et al. (2009) do not involve the assumption of equal velocities in the two layers. It is also noted that Chen and Peng (2006) have developed double layer-averaged models for distinctly stratified flows of different densities. However, these models are applicable for shallow flows over fixed bed only, without accounting for sediment transport and morphological evolution that are actively involved in dam-break floods over erodible beds.

Second, regarding to turbidity currents, most existing double layer-averaged models have not incorporated sediment transport and morphological evolution, which however are key features of reservoir turbidity currents over mobile bed. The one-dimensional double layer-averaged model by Bonnecaze et al. (1993) takes into account sediment deposition, but ignores bed sediment entrainment and morphological evolution. Also it is limited to lock-exchange gravity currents without inflow from the upstream or outflow at the downstream boundary. Strictly, the lock-exchange gravity current is not a reservoir turbidity current that is normally dictated by the water and sediment inputs from the upstream and outflow at the downstream. Briefly, until now there have been no layer-averaged models capable of modelling the whole process of reservoir turbidity currents, which is critical to effective sediment and reservoir management.

1.4. Present Work

Here a coupled double layer-averaged two-dimensional mathematical model is proposed, explicitly incorporating flow stratification, intel-layer exchange, sediment transport and morphological evolution, and thus generally applicable to sharply stratified sediment-laden flow in open channels. Especially the flow stratification, which is ignored by single layer-averaged model, can be resolved by the present model. Also, the present double layer-averaged model is physically enhanced as sediment mass conservation is explicitly incorporated in lieu of the assumption of constant sediment concentration generic to existing double layer-averaged models for dam-break flows. As compared to most existing double layer-averaged models for general gravity currents, the present model is physically extended by incorporating sediment transport and morphological evolution. The two hyperbolic systems of the governing equations for the two layers are solved separately and synchronously. Each hyperbolic system is solved by a quasi-well-balanced numerical algorithm involving drying and wetting, using a second-order accurate Godunov-type finite volume method in conjunction with the HLLC (Harten-Lax-van Leer Contact Wave) approximate Riemann solver. Employing this numerical strategy, the model is applied to two typical kinds of stratified open-channel sediment-laden flows, i.e., dam-break flows and reservoir turbidity currents. Specifically, the model is first tested against a series of experimental dam-break flows, induced by instantaneous full dam break (Spinewine 2005a) and also due to progressive failure of a single and cascade landslide dams (Cao et al. 2011a, b, Schmocker and Hager 2012). Subsequently, the model is benchmarked against a spectrum of experimental turbidity currents induced by lock-exchange (Bonnecaze et al. 1995) and sustained inflow (Lee and Yu 1997). A pilot study is presented of prototype-scale turbidity current in the Xiaolangdi Reservoir (Li 2004; YRCC 2007), Yellow River in China to demonstrate the capability of the present model. Hyperbolicity of the model equations is further analyzed as related to dam-break flows and reservoir turbidity currents.

1.5. Summary

In Chapter 2, the governing equations, auxiliary relationships and numerical algorithm are presented. The two hyperbolic systems of the governing equations for the two layers are solved separately and synchronously. Each hyperbolic system is solved by a quasi-well-balanced numerical algorithm involving drying and wetting, using a second-order accurate Godunov-type finite volume method in conjunction with the HLLC (Harten-

Lax-van Leer Contact Wave) approximate Riemann solver. In principle, the model features a reasonable balance between the flux gradients and the bed or interface slope source terms and thus applicable to irregular topographies.

In Chapter 3, the model is applied to laboratory experimental data of typical dam break flows due to instantaneous full dam break and progressive failure of a dike and landslide dams, either in a single setting or in cascade.

In Chapter 4, the model is benchmarked against a spectrum of experimental turbidity currents induced by lock-exchange and sustained inflow. Especially, it is concerned with turbidity current formation, evolution and recession, plunging characteristics, impacts of downstream boundary conditions.

Chapter 5 presents a computational study of prototype-scale turbidity currents in the Xiaolangdi Reservoir, Yellow River in China to demonstrate the capability of the present model.

Chapter 6 presents the hyperbolicity analysis of double layer-averaged model as related to the stratified sediment-laden flows induced by dam-break flows and turbidity currents. Computational tests for the turbidity currents are also presented to reveal whether an excessive clear-water outflow would spoil the turbidity current and thus induce the linked Kelvin-Helmholtz instability.

Conclusions and perspectives are summarized in Chapter 7.

CHAPTER 2 MATHEMATICAL FORMULATION

2.1. Introduction

Double layer-averaged modelling of sharply stratified sediment-laden flows has been pursued for several decades. Extensive double layer-averaged models have been proposed for dam-break flows (Fraccarollo and Capart 2002, Capart and Young 2002, Spinewine 2005a, b, Savary and Zech 2007, Zech et al. 2008) and for general gravity currents (Rottman and Simpson 1983; Bonnecaze et al. 1993; Hallworth et al. 2003; Ungarish and Zemach 2005; Adduce et al. 2012; La Rocca et al. 2012). However, the fundamental mass conservation law for sediment is violated in existing double layer-averaged models for dam-break flows. Also, sediment transport and morphological evolution have been neglected in most previous double layer-averaged models for general gravity currents. Here a coupled double layer-averaged two-dimensional mathematical model is proposed, explicitly incorporating flow stratification, inter-layer exchange, sediment transport and morphological evolution. The governing equations are derived from the fundamental conservation laws in fluid dynamics under the framework of shallow water hydrodynamics. For multi grain sizes, the model is based on the concept of the widely used active layer (Hirano 1971; Armanini and di Silvio 1988). A set of auxiliary relationships are introduced to close the model. The governing equations for each layer are cast into a non-homogeneous hyperbolic system, with the interactions between the two layers and the erodible bed as well as the boundary resistance and gravitational action represented as source terms. The two hyperbolic systems of the governing equations for the two layers are solved separately and synchronously. Each hyperbolic system is solved by a quasi-well-balanced numerical algorithm involving drying and wetting, using a second-order accurate Godunov-type finite volume method in conjunction with the HLLC (Harten-Lax-van Leer Contact Wave) approximate Riemann solver.

2.2. Structure of Double Layer-averaged Model

A general sketch of the one-dimensional (1D) double layer-averaged model is presented in Fig. 2.1. The system is represented by two moving layers and one layer at rest. Specifically, it includes (1) an upper clear-water flow layer of depth h_w and layer-averaged velocity u_w; (2) a lower sediment-laden flow layer of depth h_s, layer-averaged velocity u_s and total volumetric sediment concentration C_s; and (3) an erodible bed of volumetric sediment concentration C_b with vanishing velocity. In general, there exist interactions among the upper layer clear water flow, sediment-laden flow and the erodible bed, which are characterized by mass and momentum exchanges. Specifically, the upper layer interacts with the lower layer by exchanging clear water, but the lower layer exchanges both the water and sediment with the erodible bed. In Fig. 2.1, E_T and D_T are the total sediment entrainment and deposition fluxes across the bottom boundary respectively; E_w is the mass exchange flux of clear water across the interface between the two layers; $\eta = h_w + h_s + z_b$ is stage; $\eta_s = h_s + z_b$ is the elevation of interface between the clear-water layer and sediment-laden flow layer; and z_b is bed elevation.

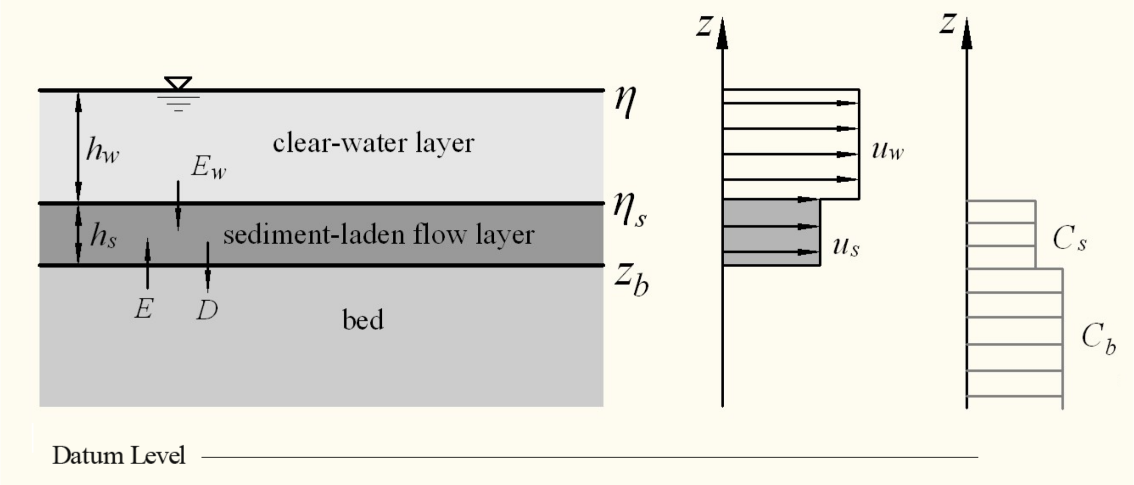

Figure 2.1 Structure of one-dimensional double layer-averaged models

2.3. Governing Equations

2.3.1. One-dimensional double layer-averaged model

Coupled modelling has been implemented in recent single layer-averaged models (Cao et al. 2004; Cao et al. 2011c; Hu and Cao 2009; Hu et al. 2012). This is followed in the present double layer-averaged model. Consider longitudinally one-dimensional double-layer flows over a mobile bed composed of N size classes. Let d_k denote the diameter of the k th size of sediments, where the subscript $k = 1$, 2, ... N. For multi grain sizes, the model is based upon the concept of the widely used active layer (Hirano 1971; Armanini and di Silvio 1988). The active layer lies between the sediment-laden flow layer and the substrate layer, where the sediment is assumed to be distributed uniformly in the vertical direction and can exchange with the upper and lower layers. The substrate layer, also known as the stratigraphy of the deposit, has certain structure in the vertical and may vary in time. Briefly, the governing equations of a double layer-averaged model comprise the mass and momentum conservation equations respectively for the clear-water flow layer and the sediment-laden flow layer, and also the size-specific mass conservation equation for the sediments carried by the flow, the total mass conservation equation for the sediments in the bed and the size-specific mass conservation equation for the sediments in the active layer of the bed surface. These equations can be derived from the fundamental conservation laws in fluid dynamics under the framework of shallow water hydrodynamics (Abbott 1979).

Consider a control volume of length Δx and width B in a channel. According to mass conservation, the variation rate of mass stored within the control volume is equal to net mass inflow rate. Therefore the mass conservation equations for the upper clear-water flow layer, lower sediment-laden layer and size-specific sediments transported by flow are respectively,

$$\frac{\partial \rho_w h_w B\Delta x}{\partial t} = (\rho_w u_w h_w B)\big|_x - (\rho_w u_w h_w B)\big|_{x+\Delta x} - \rho_w E_w B\Delta x \tag{2.1}$$

$$\frac{\partial \rho_c h_s B\Delta x}{\partial t} = (\rho_c h_s u_s B)\big|_x - (\rho_c h_s u_s B)\big|_{x+\Delta x} - \rho_w E_w B\Delta x + \rho_0 \frac{E_T - D_T}{1-p} B\Delta x \tag{2.2}$$

$$\frac{\partial \rho_s h_s c_k B\Delta x}{\partial t} = (\rho_s h_s c_k u_s B)\big|_x - (\rho_c h_s c_k u_s B)\big|_{x+\Delta x} + \rho_s \frac{E_k - D_k}{1-p} B\Delta x \tag{2.3}$$

where t is the time; x is the streamwise coordinate; $p = 1 - C_b$ is the bed sediment porosity; ρ_w, ρ_s are the densities of water and sediment respectively; c_k is the size-specific volumetric sediment concentration of the sediment-laden flow layer and $C_s = \sum c_k$; E_k is the size-specific sediment entrainment flux and $E_T = \sum E_k$; D_k is the size-specific sediment deposition flux and $D_T = \sum D_k$; $\rho_c = \rho_w(1 - C_s) + \rho_s C_s$ is the density of the water-sediment mixture in the sediment-laden flow layer; $\rho_0 = \rho_w p + \rho_s(1-p)$ is the density of the saturated bed.

Based on momentum conservation (essentially the Newton's second law), the variation rate of momentum stored within the control volume is equal to net momentum inflow rate plus sum of forces. Correspondingly, the momentum conservation equations for the upper clear-water flow layer and the lower sediment-laden layer are

$$\begin{aligned}\frac{\partial \rho_w h_w B \Delta x u_w}{\partial t} &= (\rho_w u_w^2 h_w B)\big|_x - (\rho_w u_w^2 h_w B)\big|_{x+\Delta x} - \rho_w E_w u_w B \Delta x \\ &\quad + F_{Gw} - \tau_{ix} B \Delta x + F_{Pw}\big|_x - F_{Pw}\big|_{x+\Delta x}\end{aligned} \tag{2.4}$$

$$\begin{aligned}\frac{\partial \rho_c h_s u_s B \Delta x}{\partial t} &= (\rho_c u_s^2 h_s B)\big|_x - (\rho_c u_s^2 h_s B)\big|_{x+\Delta x} + \rho_w E_w u_w B \Delta x \\ &\quad + F_{Gs} + (\tau_{ix} - \tau_{bx}) B \Delta x + F_{Ps}\big|_x - F_{Ps}\big|_{x+\Delta x}\end{aligned} \tag{2.5}$$

where $F_{Gw} = -\rho_w g h_w B \Delta x \frac{\partial \eta_s}{\partial x}$, $F_{Gs} = -\rho_c g h_s B \Delta x \frac{\partial z_b}{\partial x}$ are the downstream gravitational forces for the clear-water flow layer and the sediment-laden flow layer respectively; g is the gravitational acceleration; τ_{ix} is shear stress in the x- direction at the interface between the clear-water layer and the lower layer; and τ_{bx} is bed shear stress in the x-direction; F_{Pw} and F_{Ps} are the pressure forces for the clear-water flow layer and the sediment-laden flow layer respectively. The flow pressure is assumed to be hydrostatic as the inertial and diffusion effects in the vertical momentum equations can be usually neglected (Wu 2007).

$$P = \begin{cases} \rho_w g(\eta - z) & if \;\; \eta \ge z \ge \eta_s \\ \rho_w g h_w + \rho_c g(z_b + h_s - z) & if \;\; \eta_s \ge z \ge z_b \end{cases} \tag{2.6}$$

Therefore $F_{Pw} = B\int_{\eta_s}^{\eta} P dz = \frac{1}{2}\rho_w g h_w^2 B$, $F_{Ps} = B\int_{z_b}^{\eta_s} P dz = (\rho_w g h_w h_s + \frac{1}{2}\rho_c g h_s^2) B$.

Dividing the Eqs. (2.1-2.5) by the width (B) and the length (Δx) of the control volume and assuming $\Delta x \to 0$ give the governing equations below.

The mass and momentum conservation equations for the clear-water flow layer are

$$\frac{\partial \rho_w h_w}{\partial t}+\frac{\partial \rho_w h_w u_w}{\partial x}=-\rho_w E_w \tag{2.7}$$

$$\frac{\partial \rho_w h_w u_w}{\partial t}+\frac{\partial}{\partial x}(\rho_w h_w u_w^2+\frac{1}{2}\rho_w g h_w^2)=-\rho_w g h_w \frac{\partial (z_b+h_s)}{\partial x}-\tau_{ix}-\rho_w E_w u_w \tag{2.8}$$

The mass and momentum conservation equations for the sediment-laden flow layer are

$$\frac{\partial \rho_c h_s}{\partial t}+\frac{\partial \rho_c h_s u_s}{\partial x}=\rho_w E_w+\rho_0 \frac{E_T-D_T}{1-p} \tag{2.9}$$

$$\frac{\partial \rho_c h_s u_s}{\partial t}+\frac{\partial}{\partial x}(\rho_c h_s u_s^2+\frac{1}{2}\rho_c g h_s^2)=-\rho_c g h_s \frac{\partial z_b}{\partial x}-\frac{\partial}{\partial x}(\rho_w g h_w h_s)+\tau_{ix}-\tau_{bx}+\rho_w E_w u_w \tag{2.10}$$

The size-specific mass conservation for the sediments carried by the flow is

$$\frac{\partial \rho_s h_s c_k}{\partial t}+\frac{\partial \rho_s h_s c_k u_s}{\partial x}=\rho_s (E_k-D_k) \tag{2.11}$$

To expedite numerical solution using conservative variables, it is advisable to recast Eqs. (2.7-2.11), so that the densities do not appear on the left hand side of the equations. Thus the depth-averaged model equations are in standard and well-structured conservative form. They are summarized as follows,

$$\frac{\partial h_w}{\partial t}+\frac{\partial h_w u_w}{\partial x}=-E_w \tag{2.12}$$

$$\frac{\partial h_w u_w}{\partial t}+\frac{\partial}{\partial x}(h_w u_w^2+\frac{1}{2}g h_w^2)=-g h_w \frac{\partial \eta_s}{\partial x}-\frac{\tau_{ix}}{\rho_w}-E_w u_w \tag{2.13}$$

$$\frac{\partial h_s}{\partial t}+\frac{\partial h_s u_s}{\partial x}=E_w+\frac{E_T-D_T}{1-p} \tag{2.14}$$

$$\frac{\partial h_s u_s}{\partial t}+\frac{\partial}{\partial x}(h_s u_s^2+0.5gh_s^2)=\frac{\tau_{wx}-\tau_{bx}}{\rho_c}-gh_s\frac{\partial z_b}{\partial x}-\frac{\rho_w g}{\rho_c}h_s\frac{\partial h_w}{\partial x}$$

$$-\frac{(\rho_s-\rho_w)gh_s^2}{2\rho_c}\frac{\partial C_s}{\partial x}-\frac{(\rho_0-\rho_c)(E_T-D_T)u_s}{(1-p)\rho_c} \tag{2.15}$$

$$+\frac{(\rho_s-\rho_w)C_s E_w u_s}{\rho_c}+\frac{\rho_w E_w u_w}{\rho_c}$$

$$\frac{\partial h_s c_k}{\partial t}+\frac{\partial h_s u_s c_k}{\partial x}=E_k-D_k \tag{2.16}$$

In addition, the total mass conservation equation for the sediments in the bed and the size-specific mass conservation equation for the sediments in the active layer of the bed surface are respectively,

$$\frac{\partial z_b}{\partial t}=-\frac{E_T-D_T}{1-p} \tag{2.17}$$

$$\frac{\partial \delta f_{ak}}{\partial t}+f_{Ik}\frac{\partial \xi}{\partial t}=\frac{D_k-E_k}{1-p} \tag{2.18}$$

Eqs. (2.12) and (2.13) represent the mass and momentum conservation equations for the clear-water layer. The first two terms on the RHS (right hand side) of Eq. (2.13) represent the gravity and interfacial resistance acting on this layer, and the third term on the RHS illustrates the momentum transfer due to clear water exchange across the interface. Eq. (2.14) describes the mass conservation equation for the sediment-laden flow layer. The second term on its RHS quantifies the contribution of mass exchange with the bed. Eq. (2.15) represents momentum conservation for the water-sediment mixture in the lower layer. The first three terms on its RHS feature respectively the interfacial and bed resistances, gravity and hydrostatic pressure gradient of the clear-water layer acting on the lower layer. The fourth term on its RHS indicates the contribution of the spatial variations in sediment concentration. The fifth term represents the momentum transfer due to sediment exchange with the bed. Likewise, the last two terms on its RHS represent the momentum transfer arising from clear water exchange between two moving layers. Eq. (2.16) represents size-specific sediment mass conservation in the lower layer, incorporating sediment exchange with the bed. Eq. (2.17) represents the rate of bed deformation.

The complete set of the governing equations for a single-sized sediment transport can be easily obtained if $N = 1$ in Eqs. (2.12-2.17). For multi grain sizes, the widely used active layer formulation due to Hirano (1971), i.e., Eq. (2.18), is adopted here to resolve the change of bed composition. In Eq. (2.18), δ is the thickness of the active layer, f_{ak} is fraction of the k th size sediment in the active layer; $\xi = z_b - \delta$ is the elevation of the bottom surface of the active layer; and f_{Ik} is the fraction of the k th size sediment in the interface between the active layer and substrate layer.

2.3.2. Comparisons with previous models

Under certain premises, the double layer-averaged model above can be degenerated into two previous layer-averaged models for dam-break flows, i.e., the single layer-averaged (SL) model (Cao et al. 2004) and simplified double layer-averaged (SDL) model (Spinewine 2005a). In both cases above, N is set to be 1.

First, when the clear-water layer vanishes and in line with this status there is no water exchange across the interface, Eqs. (2.12-2.13) are trivial and Eqs. (2.14-2.17) become the same as those of the SL model by Cao et al. (2004).

Second, if sediment concentration C_s in the lower layer is assumed constant as in the SDL model by Spinewine (2005a), Eq. (2.16) is no longer required. When e_b is introduced to quantify the bed erosion rate, instead of the sediment fluxes in Eq. (2.17), bed evolution is quantified by

$$\frac{\partial z_b}{\partial t} = -e_b \tag{2.19}$$

A relationship between e_b and E_w is suggested by Spinewine (2005a) to keep the sediment concentration of sediment-laden layer constant, i.e.,

$$E_w = e_b \frac{C_b - C_s}{C_s} \tag{2.20}$$

By substituting Eqs. (2.19) and (2.20) into the governing equations of the DL model, one obtains the governing equations of the SDL model due to Spinewine (2005a). For the clear-water layer,

$$\frac{\partial h_w}{\partial t} + \frac{\partial h_w u_w}{\partial x} = -e_b \frac{C_b - C_s}{C_s} \tag{2.21}$$

$$\frac{\partial h_w u_w}{\partial t} + \frac{\partial}{\partial x}\left(h_w u_w^2 + \frac{1}{2} g h_w^2 \right) = -\frac{\tau_w}{\rho_w} - g h_w \frac{\partial (z_b + h_s)}{\partial x} - e_b \frac{C_b - C_s}{C_s} u_w \tag{2.22}$$

and for the sediment-laden flow layer:

$$\frac{\partial h_s}{\partial t} + \frac{\partial h_s u_s}{\partial x} = e_b \frac{C_b - C_s}{C_s} + e_b = e_b \frac{C_b}{C_s} \tag{2.23}$$

$$\frac{\partial h_s u_s}{\partial t} + \frac{\partial}{\partial x}\left(h_s u_s^2 + \frac{1}{2} g h_s^2 \right) = \frac{\tau_w - \tau_b}{\rho_c} - g h_s \frac{\partial z_b}{\partial x} - \frac{\rho_w g}{\rho_c} h_s \frac{\partial h_w}{\partial x} + e_b u_w \frac{C_b - C_s}{C_s} \frac{\rho_w}{\rho_c} \tag{2.24}$$

Likewise, if the sediment entrainment and deposition are partly or completely ignored and the bed deformation is neglected, the present double layer-averaged model can readily be reduced to previous double layer-averaged model for general gravity currents (e.g., Rottman and Simpson 1983; Bonnecaze et al. 1993; Hallworth et al.

2003; Ungarish and Zemach 2005; Adduce et al. 2012; La Rocca et al. 2012). However, the governing equations of double layer-averaged model do not reduce to those of a single layer-averaged model for turbidity currents. Succinctly, this is determined by the distinct philosophies and premises in deriving the governing equations of the single and double layer-averaged models. Specifically, when the upper layer vanishes, Eqs. (2.14-2.16) for the lower layer reduce to a system of equations of a traditional shallow water hydrodynamic and sediment model for sediment-laden flows (Cao et al. 2004), rather than that of a single layer-averaged model for turbidity currents (Hu et al. 2012). Similarly, if the flow velocity in the upper layer is assumed to vanish (i.e., the upper clear water is assumed to be static), Eqs. (2.14-2.16) do not reduce the system of equations of a single layer-averaged model for turbidity currents (Hu et al. 2012) either.

2.3.3. Two-dimensional double layer-averaged model

It is straightforward to extend the 1D governing equations to 2D conditions. The governing equations of the model are essentially 2D shallow water equations comprising the mass and momentum conservation equations respectively for the clear-water flow layer and the sediment-laden flow layer, and also the size-specific mass conservation equation for the sediments carried by the flow, the total mass conservation equation for the sediments in the bed and the size-specific mass conservation equation for the sediments in the active layer of the bed surface. Here the water surface elevation and the interface elevation above the datum level are employed as flow variables in the model equations. Specifically, the thickness of the clear-water flow layer h_w and the thickness of the sediment-laden flow layer h_s can be expressed as $(\eta - \eta_s)$ and $(\eta_s - z_b)$ respectively. Thus the terms, i.e., $\frac{1}{2}g(\eta^2 - 2\eta\eta_s)$ and $\frac{1}{2}g(\eta_s^2 - 2\eta_s z_b)$, arise from the simple algebraic manipulation to achieve a mathematical balance between fluxes and the source terms. Accordingly, these are

$$\frac{\partial \eta}{\partial t}+\frac{\partial h_w u_w}{\partial x}+\frac{\partial h_w v_w}{\partial y}=-E_w+\frac{\partial \eta_s}{\partial t} \tag{2.25}$$

$$\frac{\partial h_w u_w}{\partial t}+\frac{\partial}{\partial x}[h_w u_w^2+\frac{1}{2}g(\eta^2-2\eta\eta_s)]+\frac{\partial}{\partial y}(h_w u_w v_w)=-\frac{\tau_{ix}}{\rho_w}-g\eta\frac{\partial \eta_s}{\partial x}-E_w u_w \tag{2.26}$$

$$\frac{\partial h_w v_w}{\partial t}++\frac{\partial}{\partial x}(h_w u_w v_w)+\frac{\partial}{\partial y}[h_w u_w^2+\frac{1}{2}g(\eta^2-2\eta\eta_s)]=-\frac{\tau_{iy}}{\rho_w}-g\eta\frac{\partial \eta_s}{\partial y}-E_w v_w \tag{2.27}$$

$$\frac{\partial \eta_s}{\partial t}+\frac{\partial h_s u_s}{\partial x}+\frac{\partial h_s v_s}{\partial y}=E_w \tag{2.28}$$

$$\begin{aligned}\frac{\partial h_s u_s}{\partial t}+\frac{\partial}{\partial x}[h_s u_s^2+\frac{1}{2}g(\eta_s^2-2\eta_s z_b)]+\frac{\partial}{\partial y}(h_s u_s v_s)=\frac{\tau_{ix}-\tau_{bx}}{\rho_c}-g\eta_s\frac{\partial z_b}{\partial x}-\frac{\rho_w g}{\rho_c}h_s\frac{\partial h_w}{\partial x}\\ -\frac{(\rho_0-\rho_c)(E_T-D_T)u_s}{(1-p)\rho_c}+\frac{(\rho_s-\rho_w)C_s u_s E_w}{\rho_c}\\ +\frac{\rho_w E_w u_w}{\rho_c}-\frac{(\rho_s-\rho_w)gh_s^2}{2\rho_c}\frac{\partial C_s}{\partial x}\end{aligned} \tag{2.29}$$

$$\begin{aligned}\frac{\partial h_s v_s}{\partial t}+\frac{\partial}{\partial x}(h_s u_s v_s)+\frac{\partial}{\partial y}[h_s v_s^2+\frac{1}{2}g(\eta_s^2-2\eta_s z_b)]=\frac{\tau_{iy}-\tau_{by}}{\rho_c}-g\eta_s\frac{\partial z_b}{\partial y}-\frac{\rho_w g}{\rho_c}h_s\frac{\partial h_w}{\partial y}\\ -\frac{(\rho_0-\rho_c)(E_T-D_T)v_s}{(1-p)\rho_c}+\frac{(\rho_s-\rho_w)C_s v_s E_w}{\rho_c}\\ +\frac{\rho_w E_w v_w}{\rho_c}-\frac{(\rho_s-\rho_w)gh_s^2}{2\rho_c}\frac{\partial C_s}{\partial y}\end{aligned} \tag{2.30}$$

$$\frac{\partial h_s c_k}{\partial t}+\frac{\partial h_s u_s c_k}{\partial x}+\frac{\partial h_s v_s c_k}{\partial y}=E_k-D_k \tag{2.31}$$

$$\frac{\partial z_b}{\partial t}=-\frac{E_T-D_T}{1-p} \tag{2.32}$$

$$\frac{\partial \delta f_{ak}}{\partial t}+f_{Ik}\frac{\partial \xi}{\partial t}=\frac{D_k-E_k}{1-p} \tag{2.33}$$

where v_w is the layer-averaged horizontal velocity component of clear-water layer in the y - direction; v_s is the layer-averaged horizontal velocity component of sediment-laden layer flow in the y -direction; τ_{wy} are the shear stresses at the interface between the clear-water flow layer and the sediment-laden flow layer in the y - direction; and τ_{by} are bed shear stresses in the y - direction.

2.4. Auxiliary Relationships

To close the governing equations of the present 2D double layer-averaged model, a set of relationships has to be introduced to determine the bed boundary resistance, interface shear stress and water entrainment, and sediment exchange (entrainment and deposition) fluxes.

2.4.1. Resistance

Generally, unsteady and non-uniform flows may experience bed boundary resistances substantially different from those of steady and uniform flows. This is more pronounced when sediment transport is involved, which renders the bed movable and bedforms generated. However, no generally applicable relationships are currently available to represent boundary resistance in such flows. This is also the case for the interface shear stress, for which there has been different empirical relationships (Chen and Peng 2006; Kim and LeVeque 2008; Zech et al. 2008; Lee et al. 2014). Consequently, computational studies of stratified sediment-laden flows over fixed and mobile beds continue to use resistance relationships initially developed for steady and uniform flows, which are usually based on the Manning's equation. This practice is followed for the present 2D double layer-averaged model by virtue of the conventional empirical relations

$$\tau_{ix} = \rho_w g n_i (u_w - u_s)\overline{U}_{ws} \big/ h_w^{1/3} \tag{2.34a}$$

$$\tau_{iy} = \rho_w g n_i (v_w - v_s)\overline{U}_{ws} \big/ h_w^{1/3} \tag{2.34b}$$

$$\tau_{bx} = \rho_c g n_b^2 u_s \overline{U}_s / h_s^{1/3} \tag{2.35a}$$

$$\tau_{by} = \rho_c g n_b^2 v_s \overline{U}_s \big/ h_s^{1/3} \tag{2.35b}$$

where n_i is the roughness at the interface between the sediment-laden flow layer and clear-water flow layer; n_b is the roughness of the bed; $\overline{U}_s = \sqrt{u_s^2 + v_s^2}$, the resultant velocity of the sediment-laden flow layer; and $\overline{U}_{ws} = \sqrt{(u_w - u_s)^2 + (v_w - v_s)^2}$, the resultant velocity difference between the two layers.

2.4.2. Mass exchange

During the evolution process of stratified sediment-laden flows, mass exchange will occur in the lower and upper surface of sediment-laden flow layer. At the upper interface of sediment-laden flow layer, the mass flux of water entrainment E_w physically represents the mixing of the sediment-laden flow with the clear water across the interface of two layers. Due to the upward decreasing trend of vertical sediment concentration profiles, sediment concentration near the upper surface of lower sediment-laden flow layer is generally very small. Therefore only mass exchange of clear water is considered between the clear-water layer and lower sediment-laden flow layer. According to laboratory observations and numerical experiments, water exchange is critical for the evolution of sediment-laden flow layer and has been quantified through the bulk Richardson number. Following Parker et al. (1986), the water exchange is determined by

$$E_w = e_w \overline{U}_{ws} \tag{2.36}$$

where the water entrainment coefficient e_w is calculated empirically using the Richardson number $\mathrm{Ri} = g' h_s / \overline{U}_{ws}^2$ and the submerged gravitational acceleration $g' = sgc_s$ with specific gravity of sediment $s = (\rho_s / \rho_w) - 1$,

$$e_w = \frac{0.00153}{0.0204 + \mathrm{Ri}} \tag{2.37}$$

According to Eq. (2.37), as Ri approaches zero, e_w approaches a value of 0.075, appropriate for non-stratified flows. As Ri becomes much larger than 0.0204, the formula of Egashira (1980), extensively supported by data for density-driven flows, is obtained.

While at the lower interface of sediment-laden flow layer, two distinct mechanisms are generally involved in sediment exchange with the bed, i.e., bed sediment entrainment due to turbulence and sediment deposition by gravitational action, though sediment inter-particle interactions may modify the exchange to some extent. The determination of the entrainment and deposition fluxes continues to be one of the pivotal components of computational models for fluvial sediment transport and morphological evolution. Nevertheless, current formulations hinge upon a series of premises, as addressed by Cao and Carling (2002). There is little dispute that the deposition flux can be determined practically by using the local near-bed sediment concentration and hindered settling velocity. One of the most widely used approaches to specifying bed sediment entrainment flux is based on the assumption that entrainment always occurs at the same rate as it does under capacity regime. In capacity conditions, the entrainment flux is equal to the deposition flux. Therefore, bed sediment entrainment flux can be computed by using near-bed sediment concentration at capacity and settling velocity. Accordingly, the entrainment and deposition fluxes are estimated by

$$E_k = \omega_k E_{sk}\,,\ D_k = \omega_k c_{bk} \tag{2.38}$$

where ω_k is the size-specific settling velocity calculated by the formula of Zhang and Xie (1993)

$$\omega_k = \sqrt{(13.95\frac{\nu}{d_k})^2 + 1.09sgd_k} - 13.95\frac{\nu}{d_k} \tag{2.39}$$

where ν is the kinematic viscosity of water; $c_{bk} = r_{bk}c_k$ is the size-specific local near-bed concentration, r_{bk} is the ratio of the near-bed sediment concentration to layer-averaged concentration. The parameter $E_{sk} = F_k E_{sku}$ is the size-specific near-bed concentration at capacity condition, E_{sku} is the sediment capacity transport for uniform sediment, F_k is the areal exposure fraction of the k th sediment on the bed surface given by Parker (1991a, b) as below

$$F_k = \frac{f_{ak}\big/\sqrt{d_k}}{\sum(f_{ak}\big/\sqrt{d_k})} \tag{2.40}$$

With regard to suspended sediment transport, r_{bk} can be determined by evaluating the near-bed concentration at a distance of $0.05\,h_s$ from the bed surface (Parker et al. 1986)

$$r_{bk} = 1 + 31.5(\sqrt{u_*^2 + v_*^2}\big/\omega_k)^{-1.46} \tag{2.41}$$

where u_* and v_* are the bed shear velocities in the x - and y - directions. Although many empirical formulations are available for estimating the near-bed sediment concentration under capacity condition for sediment-laden open channel, only a few empirical formulae for E_{sku} are available for subaqueous turbidity currents. Parker et al. (1986) introduced the following empirical formulation,

$$E_{sku} = \begin{cases} 0.3 & \psi_k \geq 13.2 \\ 3\times10^{-12}\psi_k^{10}(1-5\psi_k^{-1}) & 5.0 < \psi_k < 13.2 \\ 0 & \psi_k \leq 5.0 \end{cases} \tag{2.42}$$

where $\psi_k = \sqrt{(u_*^2 + v_*^2)\sqrt{sgd_k^3}\big/\nu}\Big/\omega_k$. In the present study, the Zhang and Xie formula is also adopted, which is well tested and widely used for suspended sediment transport of open channel flow in the Yellow River (Zhang and Xie 1993). A correction coefficient α_k is introduced because the present study is concerned with turbidity currents. Currently there is no evidence to show that the computed results by determining each α_k for size group are better than those by using a unified parameter α. Thus a unified parameter α is used and it is estimated by calibration in the simulation. Following the logarithmic-matching treatment of Guo (2002) and using the resultant velocity $\overline{U}_s$ of the sediment-laden flow layer, one yields the adapted version of the Zhang and Xie formula

$$E_{sku} = \alpha_k \frac{1}{20\rho_s} \frac{\left(\overline{U}_s^3 / gh_s\omega_k\right)^{1.5}}{1+\left(\overline{U}_s^3 / 45gh_s\omega_k\right)^{1.15}} \tag{2.43}$$

As for the bedload sediment transport in double layer-averaged model, bedload sediment concentration typically varies very little vertically within the lower layer, as compared to its longitudinal variation. In this regard, the near-bed concentration can be represented by the average concentration of the lower layer, thus $r_{bk} = 1$. The bedload sediment transport capacity c_e is determined by

$$E_{sku} = q_{bk}/h_s\overline{U}_s \tag{2.44a}$$

$$q_{bk} = \phi_\kappa 8\sqrt{sgd_k^3}\left(\theta - \theta_{ck}\right)^{1.5} \tag{2.44b}$$

where q_{bk} is the size-specific unit-width bedload transport rate at transport capacity status; ϕ_κ is the modification coefficient; $\theta = \sqrt{u_*^2 + v_*^2} / sgd$ is the Shields parameter; and θ_{ck} is the size-specific critical Shields parameter for initiation of sediment movement. Usually, the threshold Shields parameter can be empirically determined over sufficiently mild slopes using the Shields diagram (Chien and Wan 1999). Yet, for dam-break processes that may feature steep slopes, θ_c is determined following Cao et al. (2011c). Although a plethora of empirical formulations is available for calculating q_{bk}, they are derived under steady and uniform flows, and therefore the entrainment flux based on these formulations may not be directly applicable to dam-break flows. A slightly modified version of the MPM (Meyer-Peter and Müller 1948) formula is introduced here (MMPM), with a modification coefficient ϕ_k to be calibrated using measured data. This is necessary as the Shields parameter in dam-break floods can go far beyond the range in which the MPM formula was initially derived. In essence, it is a functional form of bedload transport rate introduced based on the MPM formula, especially when the modification by Wong and Parker (2006) is considered.

The following relation is employed to evaluate f_{Ik} (Hoey and Ferguson, 1994; Toro-Escobar et al., 1996)

$$f_{Ik} = \begin{cases} f_{sk} & \partial\xi/\partial t \le 0 \\ \phi c_k/C_T + (1-\phi) f_{ak} & \partial\xi/\partial t > 0 \end{cases} \tag{2.45}$$

where f_{sk} is the fraction of the k th size sediment in the substrate layer; ϕ is the empirical weighting parameter.

In the present work, the closure relationships for the SL model for dam-break flows are in principle the special version of those for the DL model as the upper clear-water flow layer vanishes. To close the SDL model for dam-break flows, an empirical relationship is proposed to determine directly the bed erosion rate e_b using a lower and upper value of the shear stress at the bed (Spinewine 2005a), instead of the entrainment and deposition fluxes in Eq. (2.27).

Mathematical modelling has become one of the most proactive approaches in the context of hydraulic research and engineering practice. Yet concerns over its reliability have so far remained, especially when sediment transport and morphological evolution are involved. One of the most viable strategies to address these concerns is to incorporate in the governing equations of a model as much physics as possible and thereby minimize its uncertainty (uncertainty is inevitable because of the empirical relationships introduced to close the model). The present work is just one example with respect to this philosophy, i.e., eliminating the assumption of constant sediment concentration in the lower layer in SDL models for dam-break flows by applying the fundamental mass conservation law for sediment, i.e., Eq. (2.16). It is this fact that distinguishes the present DL model from the existing SDL model for dam-break flows (Spinewine 2005a). Equally importantly, this must not be confused with the empirical relationships introduced to close the governing equations of the models, which are far from generally applicable and inevitably feature uncertainty. The latter fact certainly necessitates systematic, fundamental investigations of the mechanisms of sediment transport in complex flows, i.e., highly unsteady and rapidly varied flows. Before new established closure formulations are available, model uncertainty has to be dealt with by empiricism that can be accrued through practice using measured datasets.

2.5. Numerical Algorithm

The numerical solution of two-layer shallow water equations has been research objects of intensive studies during the last years (e.g., Macías et al. 1999; Abgrall and Karni 2009). This interest is due, on the one hand, to the applicability of these models to the simulation of stratified geophysical flows. On the other hand, they can be considered as a prototype of partial differential equations involving similar difficulties, as it is the case for a number of two-phase flow models (e.g., Pitman and Le 2005; Pudasaini 2012). The main difficulty of double layer-averaged model in terms of numerical computation comes from the presence of non-conservative products. Thus, the solutions of the system may develop discontinuities and, due to the non-divergence form of the equations, the notion of weak solution in the sense of distributions cannot be used. Equally importantly, the system is conditionally hyperbolic due to the presence of the non-conservative products, i.e., the inter-layer interactions (Bouchut and Morales 2008). If the difference of the velocities of two layers exceeds a threshold, the system suffers hyperbolicity loss and the linked Kelvin-Helmholtz instability is expected (Armi 1986; Kim and LeVeque 2008). In this situation, its eigenstructure cannot be obtained in an explicit form. The loss of hyperbolicity is related to the appearance of shear instabilities that may lead, in real flows, to intense mixing of the two layers. While, in practice, this mixture partially dissipates the energy, and in numerical experiments these interface disturbances may grow and overwhelm the solution. Accordingly, some special treatments have to be developed. Castro et al. (2010) introduces an intermediate layer to recover the hyperbolicity. And Castro et al. (2011) adds locally and automatically an optimal amount of shear stress to make the flow to remain in the hyperbolicity region. Another interesting approach is proposed by Abgrall and Karni (2009), where two artificial equations are added into the system to make the extended system hyperbolic and thus it could be solved by a second-order Roe-type scheme in a rather straightforward manner. Yet the present model involves more equations than analyzed previously. Overall it is too complicated to be solved numerically as a single system presently, which is reserved for future studies.

Given the above observations, an alternative solution strategy has to be developed. As the bed deformation is entirely determined by local entrainment and deposition fluxes under the non-capacity framework for sediment transport, Eq. (2.32) is separated from the remaining equations and can be readily solved. Further, from physical perspectives, it is proposed that either the upper clear-water flow layer or the lower sediment-laden flow layer is dictated by its own inertia, gravity and boundary resistance, whilst the inter-layer interactions (mainly the second term on the RHS of Eq. (2.26-2.27) and the third term on the RHS of Eq. (2.29-2.30)) play a secondary role and can therefore be set as source terms in the momentum equations. In fact, the inter-layer interactions can be confirmed to be negligible post priori, i.e., after the numerical solution of a specific case has been achieved.

The above solution strategy facilitates the decomposition of Eqs. (2.25) to (2.31) to two reduced-order hyperbolic systems that represent respectively the upper clear-water flow layer and the lower sediment-laden flow layer, and are much easier to solve than the single system of Eqs. (2.25) to (2.31), i.e.,

$$\frac{\partial \mathbf{T}}{\partial t}+\frac{\partial \mathbf{E}}{\partial x}+\frac{\partial \mathbf{F}}{\partial y}=\mathbf{R}_b+\mathbf{R}_f+\mathbf{R}_e \tag{2.46}$$

$$\frac{\partial \mathbf{U}}{\partial t}+\frac{\partial \mathbf{G}}{\partial x}+\frac{\partial \mathbf{H}}{\partial y}=\mathbf{S}_b+\mathbf{S}_f+\mathbf{S}_e \tag{2.47}$$

$$\mathbf{T}=\begin{bmatrix}\eta\\ q_{wx}\\ q_{wy}\end{bmatrix}=\begin{bmatrix}\eta\\ h_w u_w\\ h_w v_w\end{bmatrix}\tag{2.48a}$$

$$\mathbf{E}=\begin{bmatrix}h_w u_w\\ h_w u_w^2+\frac{1}{2}g(\eta^2-2\eta\eta_s)\\ h_w u_w v_w\end{bmatrix},\ \mathbf{F}=\begin{bmatrix}h_w u_w\\ h_w u_w v_w\\ h_w v_w^2+\frac{1}{2}g(\eta^2-2\eta\eta_s)\end{bmatrix}\tag{2.48b, c}$$

$$\mathbf{R}_b=\begin{bmatrix}0\\ -g\eta\dfrac{\partial\eta_s}{\partial x}\\ -g\eta\dfrac{\partial\eta_s}{\partial y}\end{bmatrix},\ \mathbf{R}_f=\begin{bmatrix}0\\ -\dfrac{\tau_{wx}}{\rho_w}-E_w u_w\\ -\dfrac{\tau_{wy}}{\rho_w}-E_w v_w\end{bmatrix},\ \mathbf{R}_e=\begin{bmatrix}-E_w+\dfrac{\partial\eta_s}{\partial t}\\ 0\\ 0\end{bmatrix}\tag{2.48d, e, f}$$

$$\mathbf{U}=\begin{bmatrix}\eta_s\\ q_{sx}\\ q_{sy}\\ q_{ck}\end{bmatrix}=\begin{bmatrix}\eta_s\\ h_s u_s\\ h_s v_s\\ h_s c_k\end{bmatrix}\tag{2.49a}$$

$$\mathbf{G}=\begin{bmatrix}h_s u_s\\ h_s u_s^2+\frac{1}{2}g(\eta_s^2-2\eta_s z_b)\\ h_s u_s v_s\\ h_s u_s c_k\end{bmatrix},\ \mathbf{H}=\begin{bmatrix}h_s u_s\\ h_s u_s v_s\\ h_s u_s^2+\frac{1}{2}g(\eta_s^2-2\eta_s z_b)\\ h_s v_s c_k\end{bmatrix}\tag{2.49b, c}$$

$$\mathbf{S}_b=\begin{bmatrix}0\\ -g\eta_s\dfrac{\partial z_b}{\partial x}\\ -g\eta_s\dfrac{\partial z_b}{\partial y}\\ 0\end{bmatrix},\ \mathbf{S}_f=\begin{bmatrix}0\\ N_x\\ N_y\\ E_k-D_k\end{bmatrix},\ \mathbf{S}_e=\begin{bmatrix}E_w\\ 0\\ 0\\ 0\end{bmatrix}\tag{2.49d, e, f}$$

$$\begin{aligned}N_x=&\frac{\tau_{wx}-\tau_{bx}}{\rho_c}-\frac{\rho_w g}{\rho_c}h_s\frac{\partial h_w}{\partial x}-\frac{(\rho_0-\rho_c)(E_T-D_T)u_s}{(1-p)\rho_c}+\frac{(\rho_s-\rho_w)u_s E_w C_s}{\rho_c}\\ &+\frac{\rho_w E_w v_w}{\rho_c}-\frac{(\rho_s-\rho_w)gh_s^2}{2\rho_c}\frac{\partial C}{\partial x}\end{aligned}\tag{2.49g}$$

$$\begin{aligned} N_y = {} & \frac{\tau_{wy}-\tau_{by}}{\rho_c}-\frac{\rho_w g}{\rho_c}h_s\frac{\partial h_w}{\partial y}-\frac{(\rho_0-\rho_c)(E_T-D_T)v_s}{(1-p)\rho_c}+\frac{(\rho_s-\rho_w)v_s E_w C_s}{\rho_c} \\ & +\frac{\rho_w E_w v_w}{\rho_c}-\frac{(\rho_s-\rho_w)g h_s^2}{2\rho_c}\frac{\partial C}{\partial y} \end{aligned} \tag{2.49h}$$

where $\mathbf{T}$ and $\mathbf{U}$ are vectors of conserved variables; $\mathbf{E}$, $\mathbf{F}$, $\mathbf{G}$ and $\mathbf{H}$ are vectors of the flux variables. For the sediment-laden flow layer, $\mathbf{S}_b$ denotes vector of bed slope source term, $\mathbf{S}_f$ represents vector of bed friction source terms and other terms related to the impacts of sediment transport and water entrainment, $\mathbf{S}_e$ represents vector of water entrainment source term. Similarly, for the clear-water flow layer, $\mathbf{R}_b$ features vector of interface slope source term, $\mathbf{R}_f$ comprises vector of interface friction source terms and other terms related to impacts of water entrainment, $\mathbf{R}_e$ represents vector of water entrainment source term and variations of interface elevation; q_{wx}, q_{wy} are conservative variables in Eq. (2.48); q_{sx}, q_{sy}, q_{ck} are conservative variables in Eq. (2.49).

The two non-homogeneous hyperbolic systems constituted by Eqs. (2.46) and (2.47) can be solved separately and synchronously (Li et al. 2013; Cao et al. 2015) using one of a hierarchy of numerical algorithms that can capture shock waves and contact discontinuities properly. The numerical algorithm employed in the present double layer-averaged mobile model is an extension of that in the 2D model originally developed for single-layer clear-water flow over fixed bed (Liang 2010). Take Eq. (2.46) as an example. It can be solved numerically by an accurate finite volume Godunov-type approach in conjunction with the HLLC (Harten-Lax-van Leer contact wave) approximate Riemann solver (Toro 2001) on a fixed rectangular mesh. In principle, the present model is well-balanced as the inter-layer interactions play secondary roles and are negligible compared to inertia and gravitation.

2.5.1. FVM discretization

The following time-marching formulas are used to update flow and sediment variables to a new time step ($m+1$)

$$\mathbf{U}_{i,j}^{q}=\mathbf{U}_{i,j}^{m}-\frac{\Delta t(\mathbf{G}_{i+1/2,j}-\mathbf{G}_{i-1/2,j})^{m}}{\Delta x}-\frac{\Delta t(\mathbf{H}_{i,j+1/2}-\mathbf{H}_{i,j-1/2})^{m}}{\Delta x}+\Delta t\mathbf{S}_{bi,j}^{m} \tag{2.50}$$

$$\mathbf{U}_{i,j}^{m+1}=\mathbf{U}_{i,j}^{q}+\Delta t(\mathbf{S}_{f\,i,j}^{RK}+\mathbf{S}_{e\,i,j}^{RK}) \tag{2.51}$$

where the subscript m represents the time level and q indicates the state after calculating the variables from Eq. (2.50); subscripts i, j are the spatial node indexes; Δt is the time step; Δx, Δy are the spatial steps; $\mathbf{G}_{i+1/2,j}$, $\mathbf{G}_{i-1/2,j}$, $\mathbf{H}_{i,j+1/2}$ and $\mathbf{H}_{i,j-1/2}$ are the interface flux vectors.

In Eq. (2.51), the friction source term vector $\mathbf{S}_{f}^{RK}$, $\mathbf{S}_{e}^{RK}$ are computed by the third-order Runge-Kutta (RK) method (Gottlieb and Shu 1998). Take $\mathbf{S}_{f}^{RK}$ as an example,

$$\mathbf{S}_{f}^{RK}=\frac{1}{6}[\mathbf{S}_{f}(\mathbf{U}_{i,j}^{*1})+4\mathbf{S}_{f}(\mathbf{U}_{i,j}^{*2})+\mathbf{S}_{f}(\mathbf{U}_{i,j}^{*3})] \tag{2.52}$$

where $\mathbf{U}_{i,j}^{*1}=\mathbf{U}_{i,j}^{q}$, $\mathbf{U}_{i,j}^{*2}=\mathbf{U}_{i,j}^{*1}+\frac{\Delta t}{2}\mathbf{S}_{f}(\mathbf{U}_{i,j}^{*1})$, $\mathbf{U}_{i,j}^{*3}=2[\mathbf{U}_{i,j}^{*1}+\Delta t\mathbf{S}_{f}(\mathbf{U}_{i,j}^{*2})]-[\mathbf{U}_{i,j}^{*1}+\Delta t\mathbf{S}_{f}(\mathbf{U}_{i,j}^{*1})]$.

The current numerical scheme is explicit and its stability is controlled by the Courant-Friedrichs-Lewy condition. The time step is given by

$$\Delta t=C_r\min\left(\frac{\Delta x}{\left|u_{wi,j}\right|+\left(gh_{wi,j}\right)^{1/2}},\frac{\Delta y}{\left|v_{wi,j}\right|+\left(gh_{wi,j}\right)^{1/2}},\frac{\Delta x}{\left|u_{si,j}\right|+\left(gh_{si,j}\right)^{1/2}},\frac{\Delta y}{\left|v_{si,j}\right|+\left(gh_{si,j}\right)^{1/2}}\right) \tag{2.53}$$

2.5.2. HLLC scheme

Step 1 Nonnegative reconstruction of Riemann states

The interface fluxes $\mathbf{G}_{i+1/2,j}$, $\mathbf{G}_{i-1/2,j}$, $\mathbf{H}_{i+1/2,j}$ and $\mathbf{H}_{i-1/2,j}$ are computed using the HLLC Riemann solver (Toro 2001), which needs correct reconstruction of the Riemann states. The MUSCL (monotonic upstream-centered scheme for conservation laws) method is used to achieve second-order accuracy in space. The Riemann states are defined from the face values of flow variables obtained from the cell-centered flow information by applying a linear slope-limited reconstruction. At the left hand side of the cell interface $(i+1/2, j)$, the values are evaluated by

$$\bar{\eta}^{L}_{i+1/2,j} = \eta_{i,j} + \frac{1}{2}\varphi(\eta_{i,j} - \eta_{i-1,j}), \ \bar{h}^{L}_{si+1/2,j} = h_{si,j} + \frac{1}{2}\varphi(h_{si,j} - h_{si-1,j}) \qquad (2.54\text{a, b})$$

$$\bar{z}^{L}_{bi+1/2,j} = z_{bi,j} + \frac{1}{2}\varphi(z_{bi,j} - z_{bi-1,j}), \ \bar{q}^{L}_{sxi+1/2,j} = q_{sxi,j} + \frac{1}{2}\varphi(q_{sxi,j} - q_{sxi-1,j}) \qquad (2.54\text{c, d})$$

$$\bar{q}^{L}_{syi+1/2,j} = q_{syi,j} + \frac{1}{2}\varphi(q_{syi,j} - q_{syi-1,j}), \ \bar{q}^{L}_{ci+1/2,j} = q_{ci,j} + \frac{1}{2}\varphi(q_{ci,j} - q_{ci-1,j}) \qquad (2.54\text{e, f})$$

where φ represents the slope-limited function evaluated at cell (i, j) based on the flow and sediment data at the cell and its upwind and downwind neighbours, and the minmod slope limiter is used for better numerical stability (Hirsch 1990)

$$\varphi(r) = \max[0, \min(r, 1)] \qquad (2.55)$$

where r is the ratio of successive gradients of the flow to the variable under consideration; for example, e.g., for η

$$r = \frac{\eta_{i+1,j} - \eta_{i,j}}{\eta_{i,j} - \eta_{i-1,j}} \qquad (2.56)$$

Similar expressions can defined for q_{sx}, q_{sy}, q_{ck} and h_s.

The interface values of the right-hand side of the cell interface $(i+1/2, j)$ are calculated in a similar way,

$$\bar{\eta}^R_{i+1/2,j} = \eta_{i,j} + \frac{1}{2}\varphi(\eta_{i+1,j} - \eta_{i,j}), \; \bar{h}^R_{si+1/2,j} = h_{si,j} + \frac{1}{2}\varphi(h_{si+1,j} - h_{si,j}) \qquad (2.57a, b)$$

$$\bar{z}^R_{bi+1/2,j} = z_{bi,j} + \frac{1}{2}\varphi(z_{bi+1,j} - z_{bi,j}), \; \bar{q}^R_{sxi+1/2,j} = q_{sxi,j} + \frac{1}{2}\varphi(q_{sxi+1,j} - q_{sxi,j}) \qquad (2.57c, d)$$

$$\bar{q}^R_{syi+1/2,j} = q_{syi,j} + \frac{1}{2}\varphi(q_{syi+1,j} - q_{syi,j}), \; \bar{q}^R_{ci+1/2,j} = q_{ci,j} + \frac{1}{2}\varphi(q_{ci+1,j} - q_{ci,j}) \qquad (2.57e, f)$$

where φ is evaluated at cell $(i+1, j)$. The velocity components and volumetric sediment concentration are then calculated by

$$\bar{u}^L_{si+1/2,j} = \bar{q}^L_{sx\,i+1/2,j} \Big/ \bar{h}^L_{s\,i+1/2,j}, \; \bar{u}^R_{si+1/2,j} = \bar{q}^R_{sx\,i+1/2,j} \Big/ \bar{h}^R_{s\,i+1/2,j} \qquad (2.58a, b)$$

$$\bar{v}^L_{si+1/2,j} = \bar{q}^L_{sy\,i+1/2,j} \Big/ \bar{h}^L_{s\,i+1/2,j}, \; \bar{v}^R_{si+1/2,j} = \bar{q}^R_{sy\,i+1/2,j} \Big/ \bar{h}^R_{s\,i+1/2,j} \qquad (2.58c, d)$$

$$\bar{c}^L_{si+1/2,j} = \bar{q}^L_{c\,i+1/2,j} \Big/ \bar{h}^L_{s\,i+1/2,j}, \; \bar{c}^R_{si+1/2,j} = \bar{q}^R_{c\,i+1/2,j} \Big/ \bar{h}^R_{s\,i+1/2,j} \qquad (2.58e, f)$$

In a dry cell or a wet cell next to a dry cell, the face values are assumed to be the same as the corresponding flow data at the cell center. This essentially reduces the accuracy of the second-order scheme to first-order, which is normal for a slope limiting process.

Based on the above interface values, the Riemann states can be sought for designing the non-negativity of water depth. As suggested by Liang (2010), a single bed elevation at the cell interface $(i+1/2, j)$ may be defined as

$$z_{b\,i+1/2,j} = \max(\bar{z}^L_{b\,i+1/2,j}, \bar{z}^R_{b\,i+1/2,j}) \qquad (2.59)$$

The depth components of the Riemann states are then defined by

$$h^L_{s\,i+1/2,j} = \max(0,\, \bar{\eta}^L_{s\,i+1/2,j} - z_{b\,i+1/2,j}),\ h^R_{s\,i+1/2,j} = \max(0,\, \bar{\eta}^R_{s\,i+1/2,j} - z_{b\,i+1/2,j}) \qquad (2.60)$$

which preserves positive water depth. The Riemann states of other flow variables can be obtained accordingly

$$\eta^L_{s\,i+1/2,j} = h^L_{s\,i+1/2,j} + z_{b\,i+1/2,j}\,,\ q^L_{sx\,i+1/2,j} = \bar{u}^L_{s\,i+1/2,j} h^L_{s\,i+1/2,j} \qquad (2.61a, b)$$

$$q^L_{sy\,i+1/2,j} = \bar{v}^L_{s\,i+1/2,j} h^L_{s\,i+1/2,j}\,,\ q^L_{c\,i+1/2,j} = \bar{c}^L_{s\,i+1/2,j} h^L_{s\,i+1/2,j} \qquad (2.61c, d)$$

$$\eta^R_{s\,i+1/2,j} = h^R_{s\,i+1/2,j} + z_{b\,i+1/2,j}\,,\ q^R_{sx\,i+1/2,j} = \bar{u}^R_{s\,i+1/2,j} h^R_{s\,i+1/2,j} \qquad (2.61e, f)$$

$$q^R_{sy\,i+1/2,j} = \bar{v}^R_{s\,i+1/2,j} h^R_{s\,i+1/2,j}\,,\ q^R_{c\,i+1/2,j} = \bar{c}^R_{s\,i+1/2,j} h^R_{s\,i+1/2,j} \qquad (2.61g, h)$$

According to Liang (2010), it is easy to prove that the well-balancing property of the governing equations and the corresponding numerical algorithm would not be spoiled by the above reconstruction of the Riemann states if a wet-bed case is simulated. However, for a dry-bed application, a numerical technique is needed to preserve the well-balanced solutions. For example, the bed elevation and the stage component of Riemann states are locally and instantaneously modified by subtracting Δz from the original values. And $\Delta z = \max[0, (z_{b\,i+1/2,j} - \bar{\eta}^L_{s\,i+1/2,j})]$ denotes the difference between the actual and pseudo water surface level at the cell interface $(i+1/2, j)$.

$$z_{b\,i+1/2,j} \leftarrow z_{bi+1/2,j} - \Delta z \qquad (2.62a)$$

$$\eta^L_{s\,i+1/2,j} \leftarrow \eta^L_{s\,i+1/2,j} - \Delta z\,,\ \eta^R_{s\,i+1/2,j} \leftarrow \eta^R_{s\,i+1/2,j} - \Delta z \qquad (2.62b, c)$$

Local bed modification (Eq. 2.62) completes the non-negative reconstruction of Riemann states, which are then directly applied by the HLLC approximate Riemann solver to compute the interface fluxes ($\mathbf{G}_{i+1/2,\,j}$). The Riemann states at the other cell interfaces and the corresponding fluxes ($\mathbf{G}_{i-1/2,j}$, $\mathbf{H}_{i+1/2,j}$ and $\mathbf{H}_{i-1/2,j}$) are computed in the same way.

Step 2 Numerical flux estimation

Referring to the solution structure of the HLLC approximate Riemann solver, the interface flux, for instance $\mathbf{G}_{i+1/2,\,j}$, is computed from

$$\mathbf{G}_{i+1/2,\,j} = \begin{cases} \mathbf{G}^{L}_{i+1/2,\,j} & if \quad 0 \le S_L \\ \mathbf{G}^{*L}_{i+1/2,\,j} & if \quad S_L \le 0 \le S_M \\ \mathbf{G}^{*R}_{i+1/2,\,j} & if \quad S_M \le 0 \le S_R \\ \mathbf{G}^{R}_{i+1/2,\,j} & if \quad 0 \ge S_R \end{cases} \tag{2.63}$$

where $\mathbf{G}^{L}_{i+1/2,\,j} = \mathbf{G}(\mathbf{U}^{L}_{i+1/2,\,j})$ and $\mathbf{G}^{R}_{i+1/2,\,j} = \mathbf{G}(\mathbf{U}^{R}_{i+1/2,\,j})$ are calculated from the left and right Riemann states $\mathbf{U}^{L}_{i+1/2,\,j}$ and $\mathbf{U}^{R}_{i+1/2,\,j}$ for a local problem. The fluxes $\mathbf{G}^{*L}_{i+1/2,\,j}$ and $\mathbf{G}^{*R}_{i+1/2,\,j}$ correspond to the left and right sides of the middle (contact) wave and S_L, S_M and S_R are estimates of the speeds of the left, middle (contact) and right waves. When evaluating fluxes in the x-direction, it should be noted that the middle wave arising from the presence of the y-direction momentum equation is always a shear wave, across which the tangential velocity component v_s changes discontinuously while normal velocity component u_s and water depth h_s remain constant. Another passive component, sediment concentration component c_s, can be dealt with the identical way.

$$\mathbf{G}^{*}_{i+1/2,\,j} = \frac{S_R \mathbf{G}^{L}_{i+1/2,\,j} - S_L \mathbf{G}^{R}_{i+1/2,\,j} + S_L S_R (\mathbf{U}^{R}_{i+1/2,\,j} - \mathbf{U}^{L}_{i+1/2,\,j})}{S_R - S_L} \tag{2.64}$$

Different choices of wave speed estimates are possible. Fraccarollo and Toro (1995) suggest the following approximations including dry-bed options from the two-rarefaction approximate Riemann solver, whereby the left and right wave speeds are determined from

$$S_L = \begin{cases} \bar{u}^{R}_{si+1/2,\,j} - 2\sqrt{g\bar{h}^{R}_{si+1/2,\,j}} & if\ \bar{h}^{L}_{si+1/2,\,j} = 0 \\ \min(\bar{u}^{L}_{si+1/2,\,j} - \sqrt{g\bar{h}^{L}_{si+1/2,\,j}}, u^{*}_{si+1/2,\,j} - \sqrt{gh^{*}_{si+1/2,\,j}}) & if\ \bar{h}^{L}_{si+1/2,\,j} > 0 \end{cases} \tag{2.65}$$

and

$$S_R = \begin{cases} \bar{u}^{L}_{si+1/2,\,j} - 2\sqrt{g\bar{h}^{L}_{si+1/2,\,j}} & if\ \bar{h}^{R}_{si+1/2,\,j} = 0 \\ \min(\bar{u}^{R}_{si+1/2,\,j} - \sqrt{g\bar{h}^{R}_{si+1/2,\,j}}, u^{*}_{si+1/2,\,j} - \sqrt{gh^{*}_{si+1/2,\,j}}) & if\ \bar{h}^{R}_{si+1/2,\,j} > 0 \end{cases} \tag{2.66}$$

where, and are calculated from

$$u^{*}_{si+1/2,\,j} = \frac{1}{2}(\bar{u}^{L}_{si+1/2,\,j} + \bar{u}^{R}_{si+1/2,\,j}) + \sqrt{g\bar{h}^{L}_{si+1/2,\,j}} - \sqrt{g\bar{h}^{R}_{si+1/2,\,j}} \tag{2.67}$$

and

$$h^{*}_{si+1/2,\,j} = \frac{1}{g}[+\frac{1}{2}(\sqrt{g\bar{h}^{L}_{si+1/2,\,j}} + \sqrt{g\bar{h}^{R}_{si+1/2,\,j}}) + \frac{1}{4}(\bar{u}^{L}_{si+1/2,\,j} - \bar{u}^{R}_{si+1/2,\,j})] \tag{2.68}$$

For general problems including dry-bed cases, the middle wave speed is calculated by (Toro 2001)

$$S_M = \frac{S_L \bar{h}^{R}_{si+1/2,\,j}(\bar{u}^{R}_{si+1/2,\,j} - S_R) - S_R \bar{h}^{L}_{si+1/2,\,j}(\bar{u}^{L}_{si+1/2,\,j} - S_L)}{\bar{h}^{R}_{si+1/2,\,j}(\bar{u}^{R}_{si+1/2,\,j} - S_R) - \bar{h}^{L}_{si+1/2,\,j}(\bar{u}^{L}_{si+1/2,\,j} - S_L)} \tag{2.69}$$

Similar formulae are used to calculate $\mathbf{G}_{i-1/2,j}$, $\mathbf{H}_{i+1/2,j}$ and $\mathbf{H}_{i-1/2,j}$.

The bed slope term S_b^k is discretized using the method proposed by Liang (2010). The procedure for the x-direction is outlined below; that for the y-direction is similar.

$$-g\eta_s \frac{\partial z_b}{\partial x} = -g\overline{\eta}_s \left(\frac{z_{b\,i+1/2,j} - z_{b\,i-1/2,j}}{\Delta x} \right) \tag{2.70}$$

where $\overline{\eta}_s = 0.5\left(\eta^R_{s\,i-1/2,j} + \eta^L_{s\,i+1/2,j}\right)$

Eq. (2.47) for the clear-water flow layer can be solved in a similar procedure as Eq. (2.46).

While the governing equations are presented for both 1D and 2D, the numerical algorithm presented above applies solely to the 2D governing equations. To solve the 1D coupled model, the total-variation-diminishing version (TVD) of the second-order weighted-average-flux (WAF) method is used along with HLLC (Harten-Lax–van Leer Contact Wave) approximate Riemann solvers for the homogeneous equations. A Runge-Kutta scheme is applied to solve the ordinary differential equations composed of the source terms (Li et al. 2013). The imbalanced 1D coupled model was applied to resolve the dam-break flows in Chapter 3. The 1D model was later extended to the 2D condition and made quasi-well-balanced for the turbidity currents in Chapters 4, 5 and 6. Nevertheless, the dam-break flows are revisited by the quasi-well-balanced 2D coupled model and the numerical discriminations are trivial between the computed results by 1D and 2D models.

Additionally, the governing equations of the SDL model for dam-break flows, i.e., Eqs. (2.21) to (2.24), are cast into a single system, which may suffer hyperbolicity loss, and then solved numerically using the same algorithm as previously proposed by Spinewine (2005a), i.e., a second-order Godunov finite-volume scheme along with the LHLL (Lateralized Harten-Lax-van Leer) Riemann solver (Fraccarollo et al. 2003). However, this numerical algorithm is selected and used to construct the solution based on the optimistic but unjustified assumption that the loss of hyperbolicity will not invalidate the results. Thus previously, this model is merely restricted to modelling the small-scale laboratory experiments.

2.6. Summary

Here a coupled double layer-averaged two-dimensional mathematical model has been developed, explicitly incorporating flow stratification, inter-layer exchange, sediment transport and morphological evolution, and thus generally applicable for the stratified sediment-laden flow in open channels. Especially the flow stratification, which is ignored by single layer-averaged model, is resolved by the present model. Also, the present double layer-averaged model is physically enhanced as sediment mass conservation is explicitly incorporated in lieu of the assumption of constant sediment concentration generic to existing double layer-averaged models for dam-break flows. In comparison to most existing double layer-averaged model for general gravity currents, the present model is physically extended by incorporating sediment transport and morphological evolution. Within the present model, the governing equations for each layer are cast into a non-homogeneous hyperbolic system, with the interactions between the two layers and the erodible bed as well as the boundary resistance and gravitational action represented as source terms. A set of relationships has to be introduced to determine the bed boundary resistance, interface shear stress, water entrainment and sediment exchange (entrainment and deposition) fluxes. The two hyperbolic systems of the governing equations for the two layers are solved separately and synchronously. Each hyperbolic system is solved by a quasi-well-balanced numerical algorithm involving drying and wetting, using a second-order accurate Godunov-type finite volume method in conjunction with the HLLC (Harten-Lax-van Leer Contact Wave) approximate Riemann solver. Admittedly, the sediment-laden flow layer with high contents of fine sediments may behave as non-Newtonian fluids, which necessitate physically improved constitutive relationships to be incorporated in the model. Technically, the great computational cost is of major concern when applied to prototype-scale cases as a fixed uniform mesh is adopted. In this regard, the technique of adaptive mesh refining can be incorporated, which can greatly save computational time by an order of magnitude.

CHAPTER 3 MODELLING DAM-BREAK FLOWS

3.1. Introduction

Dam-break flows are generally energetic and may induce active sediment transport and rapid morphological changes, which in turn conspire to modify the flows. In general, strong interaction exists among the flow, sediment transport and channel morphology. Enhanced understanding of dam-break floods and the linked hydraulics has become extremely significant in the fields of water resources, environment protection, ecology management and public safety, given the occurrence of crumbling dams and the generally catastrophic floods worldwide. Typical examples of dam-break include the October 1999 case in Poerua River in Westland, South Island, New Zealand (Davies et al. 2007) and the June 1967 case in the Yalong River in China (Li et al. 1986; Chen et al. 1992). In addition, unpredictable massive earthquakes or other violent disturbances to dam infrastructure may induce major dam-break. It is also believed that reservoirs may be connected to seismic activities to some extent (Dalton 2010), implying that reservoirs could be responsible for the occurrence of earthquakes. For example, there is concern over the Three Gorges Dam in the Yangtze River, China (Stone 2008). Field observation is undoubtedly the most straightforward and direct method to study dam-break flows, from which significant understanding of the related physics can be derived. However, the field observations of dam-break flows have still remained so far rare. It is largely because the observations are extremely hard to conduct due to the destructive power and unpredictable occurrence. In this regard, the information from these observations is rather limited and thus adds little to the systematic understanding of the physics. Comparatively, laboratory experiments provide a well-controlled way to understand the natural phenomena systematically. Extensive laboratory experiments have been undertaken to study dam-break flows.

In general, dam-break experiments include two categories, i.e., full and sudden release of an idealized vertical “dam”, and progressive failure of a single or cascade dams. In regard to full and sudden dam break, the regions on both sides of the “dam” may consist of a single horizontal “layer” or a succession of “layers” at rest, usually made of fluid or granular material, each having homogeneous properties and extending far from the “dam”. After removal of the “dam”, the two distinct regions are set in contact and a dam-break wave results. Most commonly, the physical mechanism responsible for the initiation of movement is gravity, transforming potential energy accumulated behind the dam into kinetic energy of the propagating wave. Experimental investigations of the geomorphic impacts of dam-break floods can be traced back to the pioneering work of Chen and Simons (1979), where the backward erosional rarefaction wave is induced by the sudden removal of a submerged barrage in a steady flow. The first idealized sudden and full dam-break experiment is performed by Capart and Young (1998) in a typical dam-break configuration, in which a kind of very light sediment with specific density 1.048 is used. Leal et al. (2002) performed experiments with granular material of two distinct densities, sand and pumice. They also investigated the variety of flow patterns observed when changing the initial conditions, by varying the bed level and water level upstream of the gate, but in the absence of a sediment bed downstream of the gate. At the laboratory of the Civil Engineering department of the Université catholique de Louvain (UCL), dam-break experiments have previously been performed by Capart (2000), Spinewine and Zech (2002). These experiments have been conducted in a multi-purpose tilting flume equipped with a rising gate simulating the dam-break. The flume was found to have several limitations that induced substantial perturbations of the flow during gate removal and altered the quality of the attainable experimental conditions. In order to solve this problem, a novel experimental flume, equipped with a rapidly lowering gate for the purpose of achieving better-defined initial conditions, is adopted by Spinewine (2005a), Spinewine and Zech (2007), and Goutière et al. (2011). Such method can approach the idealization of an instantaneous dam collapse and thus provide a clear-cut initial-value problem to investigate the physical mechanisms of sediment entrainment and transport in highly transient conditions. Essentially, the double-layer structure of dam-break flows, i.e., a bedload sediment transport layer and the upper clear-water flow layer, is clearly observed.

In contrast to full and sudden dam-break experiments, numerous physical experiments on landslide dam failure have been performed (e.g., Coleman et al. 2002; Chinnarasri et al. 2003; Rozov 2003; Balmforth et al. 2008, 2009; Schmocker and Hager 2009). Specifically, Coleman et al. (2002) conducted flume experiments on overtopping breaching of non-cohesive homogenous embankments, which investigated the breach erosion process, the breach geometry and the breach discharge, allowing for flood prediction due to dike failure. Chinnarasri et al. (2003) studied the flow patterns and the progressive damage of dike overtopping. It revealed four stages of dike damage and the degradation rate of the dike crest. Rozov (2003) conducted laboratory experiments to investigate the process of dam breach erosion, in which the physical mechanism of dam failure is described. However, these physical experiments are constrained by the comparatively small spatial scales and thus may not be able to fully reveal the complicated mechanism of the flood flow. In addition, these experimental studies have mostly focused on the dam failure process, while the flood hydrographs are sparsely observed. For example, Coleman et al (2002) simply measured the outflow discharge of the breach, but neglected the flow conditions at the upstream and downstream of the dam. Chinnarasri et al. (2003), and Balmfroth et al. (2008, 2009) measured the geometry of the failing dam, but ignored the flow measurements. Indeed, a range of factors involving dam structure as well as hydrodynamic actions may affect the rate and size of breach formation (Morris 2009). In this connection, the experiments by Coleman et al. (2002) and Chinnarasri et al. (2003) are limited to the failure of the dams under the action of a single inflow discharge. It is certainly critical to understand the influences of the inflow discharge, dam height, and composition on the dam failure and flood processes. Importantly, a series of relatively large-scale physical experiments were conducted to study landslide dam failure and the flood by Cao et al. (2011a, b). The experiments were carried out in a flume of 80 m × 1.2 m × 0.8 m. An array of twelve automatic water-level probes was set at the center of each cross-section along the flume to record the transient stages. Compared to previous experiments on small-scale facilities (e.g., Coleman et al. 2002; Chinnarasri et al. 2003; Balmfroth et al. 2008, 2009; Schmocker and Hager 2009), these experiments covered a wide range of inflow discharges from the upstream, initial dam height, and initial breach dimension. The stage hydrographs and video recordings of the dam failure processes for each run of the experiments were obtained. The data help reveal the mechanisms of dam failure and flood propagation.

The present model is applied to a series of typical cases, including laboratory experiments on flows induced by instantaneous full dam break (Spinewine 2005a) and also flows due to progressive failure of a single and cascade landslide dams (Cao et al. 2011a, b, Schmocker and Hager 2012). The model has also been compared with two existing models, including the SDL model of Spinewine (2005a) and the SL model by Cao et al. (2004). To quantify the error of a numerical solution as compared against measured data, the non-dimensional discrepancy is defined based on the L^1 norm

$$L_{st}^{1}=\frac{\sum abs(\eta_i-\widehat{\eta}_i)}{\sum(h_w+h_s)_i} \tag{3.1a}$$

$$L_{in}^{1}=\frac{\sum abs[(h_s+z_b)_i-(\widehat{h}_s+\widehat{z}_b)_i]}{\sum(h_s)_i} \tag{3.1b}$$

$$L_{bd}^{1}=\frac{\sum abs\left(\Delta z_{bi}-\Delta\widehat{z}_{bi}\right)}{\sum abs\left(\Delta z_{bi}\right)} \tag{3.1c}$$

where L_{st}^{1}, L_{in}^{1} and L_{bd}^{1} are L^{1} norms for stage, interface between the two layers, and bed deformation depth. The bed deformation depth is defined by $\Delta z_{bi}=z_b-z_b(t=0)$, and $\widehat{\eta}$, $\widehat{h}_s+\widehat{z}_b$ and $\Delta\widehat{z}_b$ are measured stage, interface elevation and bed deformation respectively, while h_s+z_b and Δz_b are the stage, interface elevation and bed deformation from a numerical solution. In the present chapter, a fixed uniform mesh is adopted, and the spatial step is sufficiently fine to ensure mesh independence of the solution, i.e., essentially equivalent solutions are obtained with an even finer mesh. The spatial step Δx is set to be 0.02 m and the Courant number C_r is 0.5. Bed porosity p = 0.4 is adopted for all the test cases.

3.2. Instantaneous Full Dam-break

Mobile-bed dam-break experiments were carried out in a transparent flume at the Université Catholique de Louvain, Belgium (Spinewine 2005a). The flume was 6 m long, 0.25 m wide and 0.70 m high. Dam break was simulated by the rapid downward removal of a thin gate at the middle of the flume. The experiments were conducted over an initially horizontal bed composed of non-cohesive sediments, saturated with water and extending on both sides of the idealized “dam” represented by the gate. Here, one experimental case is revisited, labelled as Test Case 3.1, with an initial water depth

$h_0 = 35$ cm upstream the dam. The median diameter of the bed material composed of PVC pellets was 3.92 mm and the density was 1580 kg/m^3. Numerical modelling was performed within the time period before the forward and backward waves reached the downstream and upstream boundaries, thus the boundary conditions can be simply set at the initial static status. For the SDL model, sediment concentration C_s in the lower layer is set to be 0.22 following Spinewine (2005a), except otherwise specified. The bed roughness n_b is set to be 0.026 m$^{-1/3}$ s following Zech et al. (2008). The modification coefficient ϕ adopted in the DL and SL models and the interface roughness n_w are determined by fitting to the measured stage. It is found that $\phi = 2.0$ for the DL model, $\phi = 3.0$ for the SL model and $n_i = 0.006$ m$^{-1/3}$ s for the DL and SDL models lead to satisfactory agreement with the measured data.

Fig. 3.1 shows water surface and bed profiles measured and computed by the DL, SDL and SL models. The bed scour depth and flood wave fronts are reproduced well by the three models as trivial difference is identified. Fig. 3.2 illustrates the water surface and bed profiles along with the interface computed from the DL and SDL models. Undesirable non-physical oscillations of the water surface profiles and interfaces from the SDL model are spotted (Fig. 3.2b). Quantitatively, the values of the L^1 norms of the DL, SDL and SL models for this case are similar (Table 3.1). The temporal and spatial scales of the flow, sediment transport and bed evolution in this particular case are so small that the performances of the three models are hardly distinguishable from Table 3.1, except the oscillations due to the SDL model in Fig. 3.2(b).

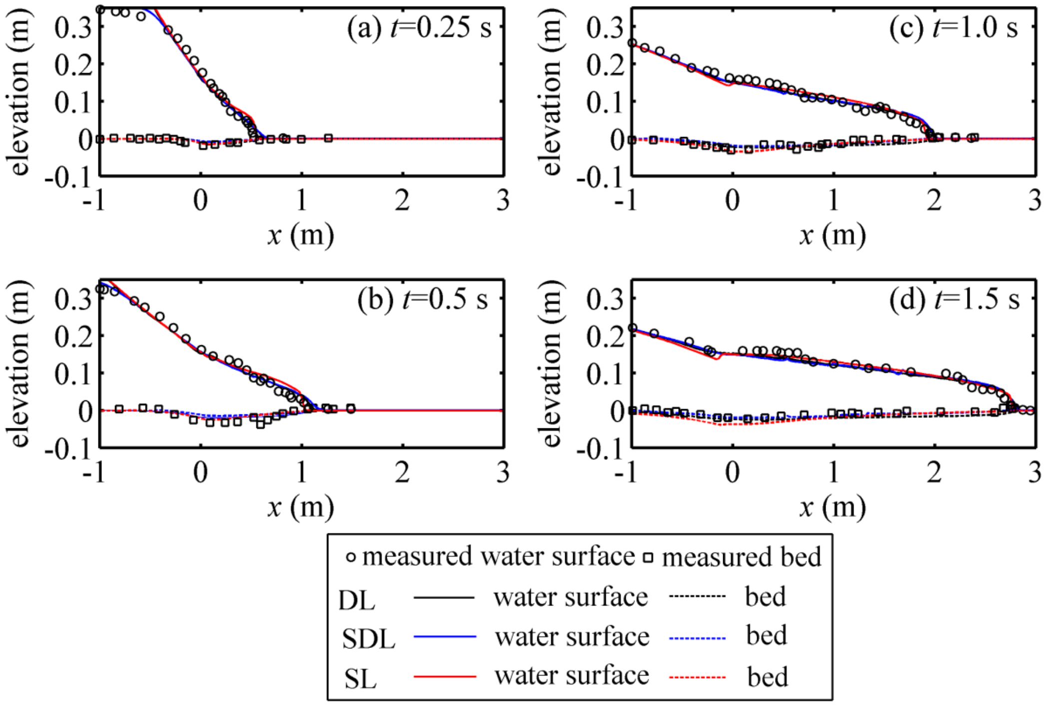

Figure 3.1 Computed water surface and bed profiles compared with measured data

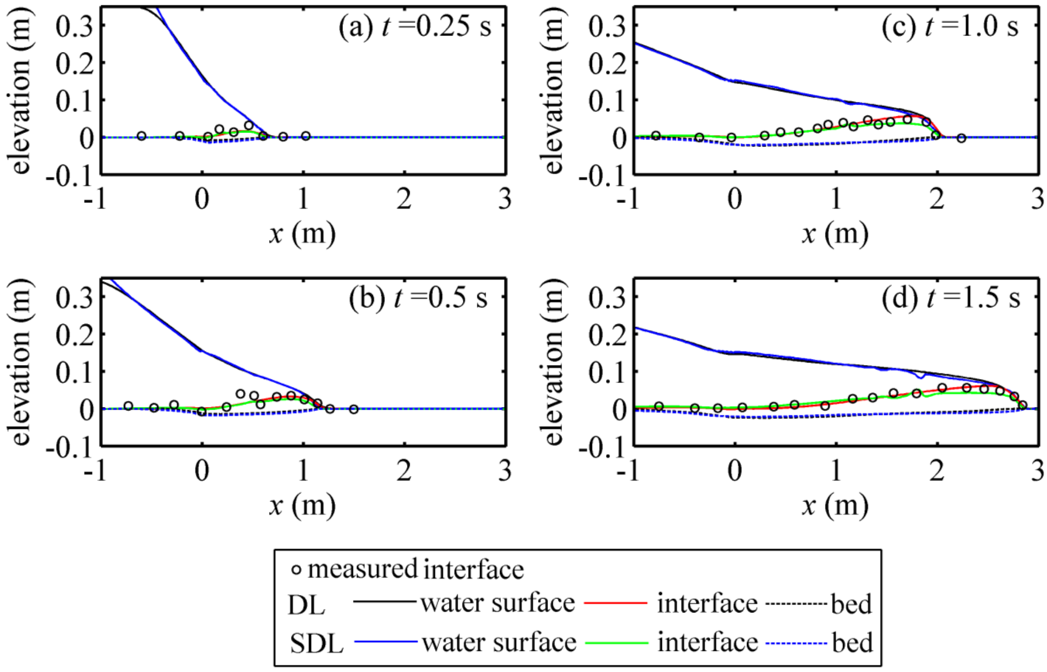

Figure 3.2 Water surface and bed profiles along with the interface from DL and SDL model

Table 3.1 L^1 Norm of the DL, SDL and SL models for instantaneous and full dam break (Test Case 3.1)

Time	t =0.25 s			t =1.5 s		
L^1	DL	SDL	SL	DL	SDL	SL
L^1_{st}	2.68%	2.75%	2.71%	3.72%	3.93%	3.89%
L^1_{in}	3.12%	3.11%	n/a	3.46%	3.52%	n/a
L^1_{bd}	4.45%	4.78%	3.89%	4.47%	4.84%	5.22%

3.3. Progressive Failure of a Single and Cascade Landslide Dams

In contrast to instantaneous full dam break (Test Case 3.1) considered above, A series of flume experiments on landslide dam breach and the resulting floods are documented by Cao et al. (2011a, b). These experiments were carried out in a flume of dimensions 80 m×1.2 m×0.8 m (Figure 3.3) and bed slope 0.001 in Wuhan University. A set of 12 automatic water-level probes was used to measure the stage hydrographs at 12 cross-sections along the flume. In the experiments, the dams failed by virtue of erosion of the overtopping flow when there was no initial breach. The experiments provided a unique and systematic set of observed data for testing mathematical models for dam breach and the resulting floods.

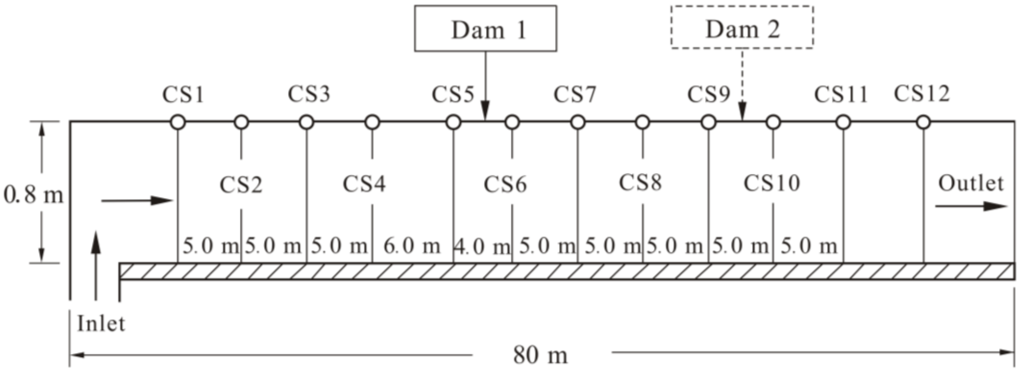

Figure 3.3 Experimental setup for landslide dam failure

To demonstrate the performance of the models, two experimental runs are revisited, i.e., F-Case 11 and T-Case 2 without initial dam breach (Cao et al. 2011a, b), which are labelled as Test Cases 3.2 and 3.3 in this Chapter respectively. In both cases, the initial upstream and downstream slopes of the dam were 1/2 and 1/3, respectively. The median diameter of the non-cohesive dam material was 0.8 mm and the specific gravity of the sediment was 1.65. For F-Case 11 (Test Case 3.2), the single dam was initially 0.4 m high, located at about 41 m from the inlet of the flume. The inlet flow discharge was 0.042 m^3/s. The initial static water depths immediately upstream and downstream of the dam were 0.054 m and 0.048 m, respectively. For T-Case 2 (Test Case 3.3) that involved two dams in cascade, both dams were 0.4 m high initially, and located at 41 m and 60.3 m respectively from the inlet of the flume. The inlet discharge was 0.025 m^3/s. The initial static water depth was 0.054 m immediately upstream the first dam, while it was 0.048 m immediately upstream and downstream the second dam. At the inlet boundary, flow discharge was specified, and the water depth and velocity were determined by the method of characteristics. There was no sediment-laden flow layer at the inlet. Besides, a 0.15-m high-weir was set at the flume outlet. Observation during the course of the experiments showed that a hydraulic drop occurred downstream of the weir, so the outflow did not affect the flow upstream of the weir. Here, a transmissive condition (Toro 2001) was imposed at the downstream boundary (80 m), and all the primitive variables in the outlet nodes were equal to those of internal nodes closest to the boundary.

For this modelling exercise, the modification coefficient ϕ adopted in the DL and SL models, the interface roughness n_i for the DL and SDL models as well as the lower-layer sediment concentration C_s in the SDL model are first calibrated using the measured stage hydrographs from the experiments for a single dam failure F-Case 11, and then directly applied for T-Case 2 of cascade dam failure. It is found that the modification coefficient $\phi = 4.5$ for the DL model, $\phi = 6.0$ for the SL model, interface roughness $n_w = 0.006$ m$^{-1/3}$ s for the DL and SDL models, and sediment concentration $C_s = 0.1$ for the SDL model lead to satisfactory agreements with measured data. For all the three models, bed roughness $n_b = 0.012$ m$^{-1/3}$ s.

Figs. 3.4 and 3.5 show the computed stage hydrographs by the DL, SDL, SL models and the measured data in both cases at selected cross-sections. The cross sections CS1, CS5, CS8 and CS12 are located at 19 m, 40 m, 54 m and 73.5 m respectively from the inlet of the flume (Fig. 3.3). For F-Case 11, CS5 and CS12 are located upstream and downstream the dam respectively. For T-Case 2, CS1 and CS5 are upstream the first dam, CS8 is between the two dams and CS12 is downstream the second dam. It is seen from Figs. 3.4 and 3.5 that the computed stages by the three models are in fairly good agreement with the measured data while slight discrepancies are observed.

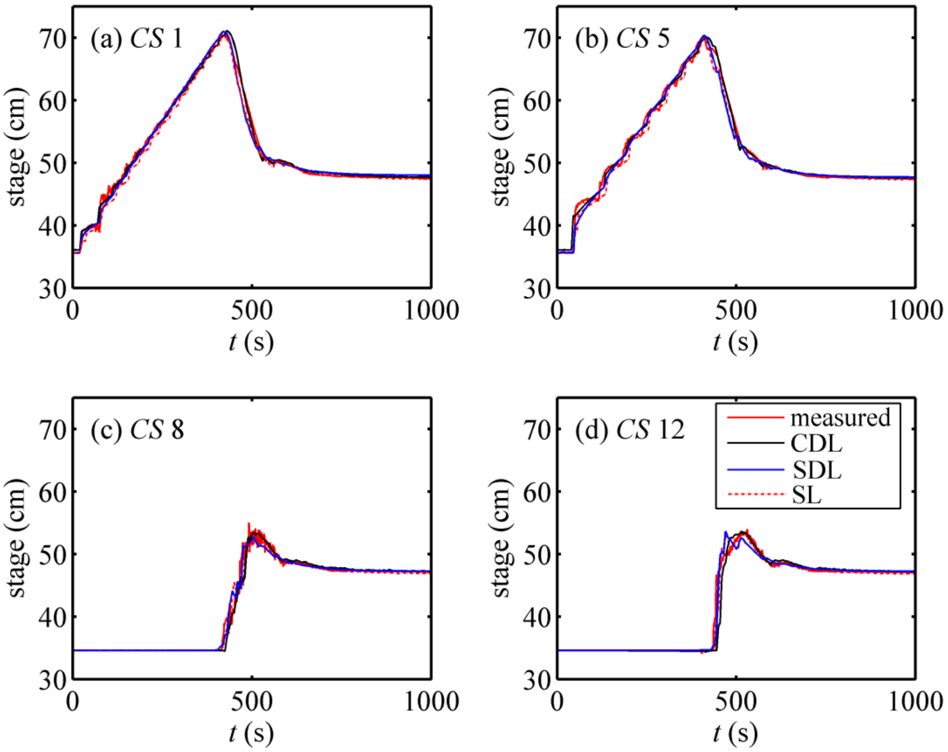

Figure 3.4 Stage hydrographs for a single landslide dam breach

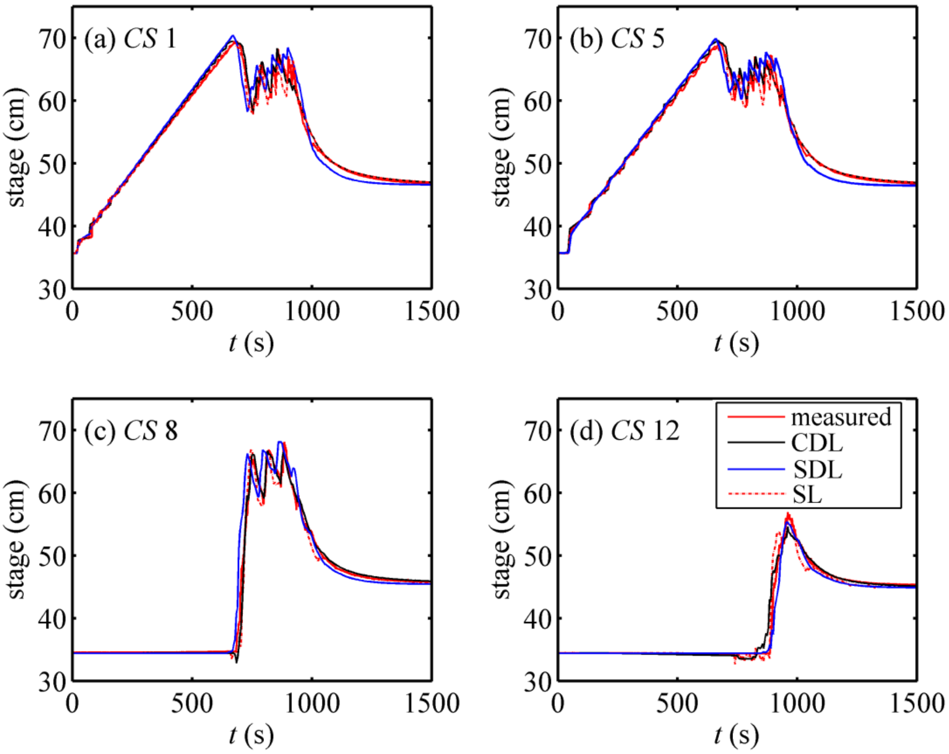

Figure 3.5 Stage hydrographs for cascade landslide dam breach

Figs. 3.6 and 3.7 illustrate the water surface and bed profiles computed from the DL, SDL and SL models, along with the measured data for the water surface elevation and the interface from the DL and SDL models. In fact, the progressive failure of the dams is explicitly represented by the evolution of the bed profile. Regardless of the fact that the stage hydrographs at selected cross-sections by the SDL model match the measured data fairly well (Figs. 3.4 and 3.5), the computed bed and water surface profiles by the SDL model exhibit serious non-physical oscillations and may deviate from the measured data significantly [Figs. 3.6(a2-d2) and 3.7(a2-e2)]. Obviously, the numerical results from the SDL model are badly spoiled, rendering the sediment-laden flow layer hardly recognizable when compared against the results from the DL model [Figs. 3.6(a1-d1) and 3.7(a1-e1)]. It is critical to point out that the numerical oscillations are inherent to the SDL model, as the use of a reduced or increased Courant number (e.g., $C_r = 0.1$, 0.9) does not eliminate the oscillations (not shown). Yet, it is premature to conclude if the numerical oscillations result from the assumption of constant sediment concentration embedded in the SDL model or the loss of hyperbolicity. Indeed, immediately following the onset of the dam breach (e.g., at 410 s in Fig. 3.6 and 675 s in Fig. 3.7), the SDL model performs similarly well to the DL and SL models when compared with the measured water surface elevation. However, at other instants when the flow is rapidly varied longitudinally and clearly exhibits complex structure such as subcritical-to-supercritical transitions and hydraulic jumps (e.g., at 430 s and 450 s in Fig. 3.6 and 700 s and 900 s in Fig. 3.7), the SDL model performs poorly when compared to the measured data, in sharp contrast to the DL and SL models. Comparatively, the DL model performs appreciably better than the traditional SL model in resolving the complex flow structures (hydraulic jumps), as shown in Figs. 3.6 and 3.7.

Echoing Figs. 3.6 and 3.7, the values of the norm for stage L_{st}^1 (Tables 3.2 and 3.3) provide further testament for the improved performance of the DL model over the SDL and SL models in comparison with measured data. Specifically, the DL and SDL models feature respectively the minimum and maximum L_{st}^1 values, while the SL model lies in between the two, consistently through time. Particularly, when the flow is rapidly varied (e.g., 430 s in Fig. 3.6 and 700 s in Fig. 3.7), the L_{st}^1 values of the SDL model are twice or even greater than those of the DL model (Tables 3.2 and 3.3). These observations lead one to comment, if only briefly, that the DL model is physically enhanced over the SL and SDL models and therefore performs the best, though the computational cost is appreciably increased by approximately 40% and 8% as compared to SL and SDL models respectively.

The whole processes of the dam failure, flow, sediment transport and bed evolution resolved by the DL model is now briefly interpreted. For F-Case 11 (Test Case 3.2), at $t = 410$ s, the water flows over the top of the dam and starts to erode the toe [Fig. 3.6(a1)]. At $t = 430$ s, the overtopping flow erodes the downstream surface of the dam, causing the formation of the sediment-laden flow layer [Fig. 3.6(b1)], and a hydraulic jump is formed around the dam site, which is characterized by the variation of Froude number (not shown). Compared to that at $t = 430$ s, the dam is further eroded at $t = 450$ s [Fig. 3.6(c1)], and the sediment-laden flow layer further develops more fully. Besides, there exist two hydraulic jumps downstream of the dam. After $t > 600$ s, the free surface of the flow is nearly horizontal, unable to further erode the dam, and the dam failure process essentially terminates [Figs. 3.6(d1)]. For T-Case 2 (Test Case 3.3), at $t = 675$ s, the water flows over the first dam, of which the toe starts to be eroded [Fig. 3.7(a1)]. At $t = 700$ s, the overtopping flow further erodes the first dam and the sediment-laden flow layer forms [Fig. 3.7(b1)]. Two hydraulic jumps occur between the two dams. At

$t = 875$ s [Fig. 3.7(c1)], the erosion of the first dam increases and the sediment-laden flow layer between the two dams develops further. Additionally, the overtopping flow starts to erode the downstream surface of the second dam and thus the sediment-laden flow layer forms downstream. At $t = 900$ s, the second dam is further eroded, leading to the amplification of the sediment-laden flow layer downstream, while a hydraulic jump is also formed around the second dam site [Fig.3.7(d1)]. After $t > 1200$ s, the water surface tends to be rather smooth and the dam failure process almost terminates. Clearly, the second dam is not eroded as fully as the first dam due to the energy dissipation downstream [Fig. 3.7(e1)].

Overall, the SL model performs well compared to the measured water surface elevation, as previously stated in regard to its extended version (Cao et al. 2011a, c). The DL model clearly shows promise for successful modelling of the highly transient and complex flows due to progressive failure landslide dams, either in a single setting or in a cascade. It resolves in a more detailed manner the physical phenomenon, facilitating a resolution of the sediment-laden flow layer, which is unavailable from the SL model. The SDL model performs poorly compared to measurements. Theoretically, the latter fact arises from the assumption of constant sediment concentration in the lower layer, which essentially breaks the fundamental mass conservation law for sediment.

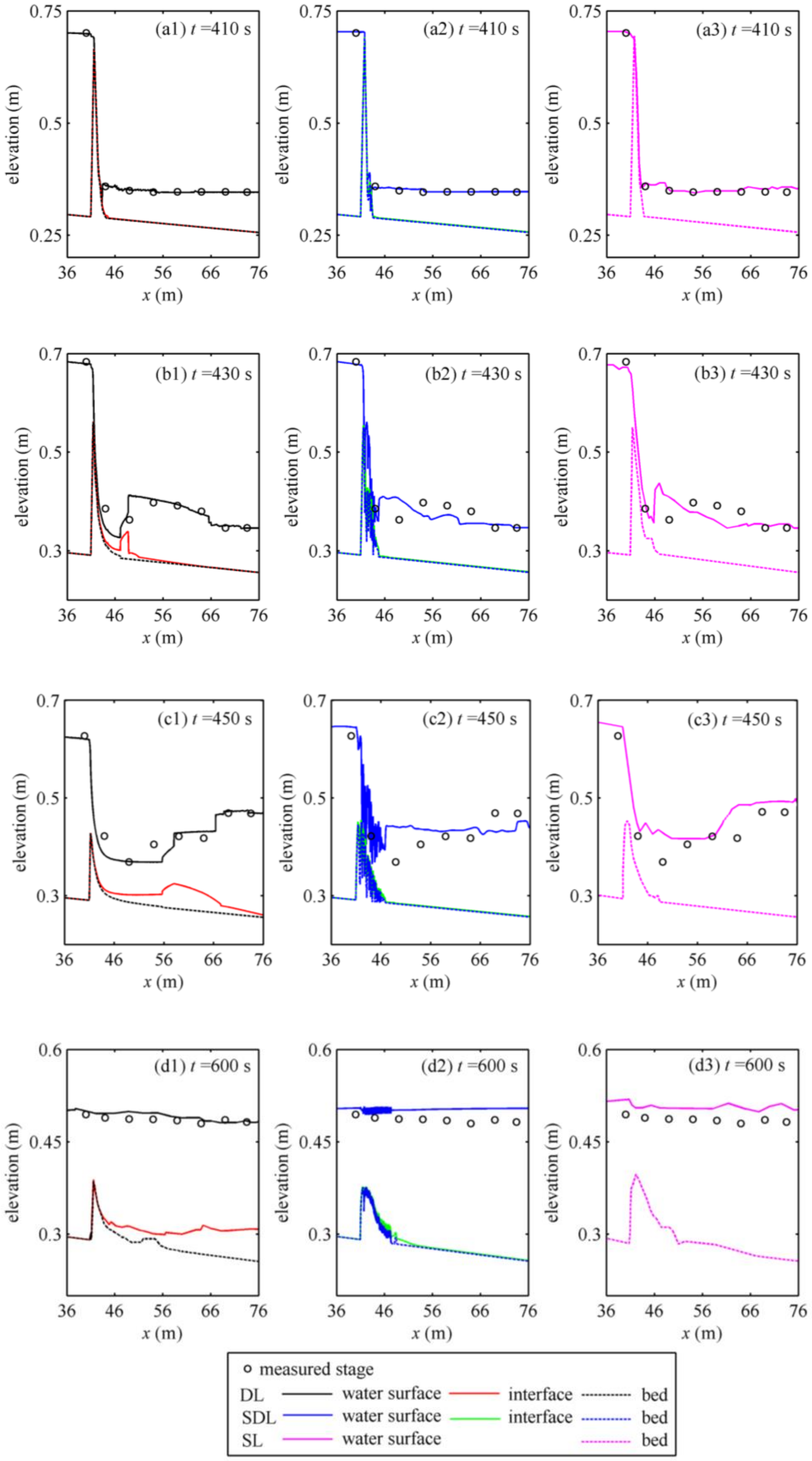

Figure 3.6 Water surface, interface and bed profiles for a single landslide dam failure

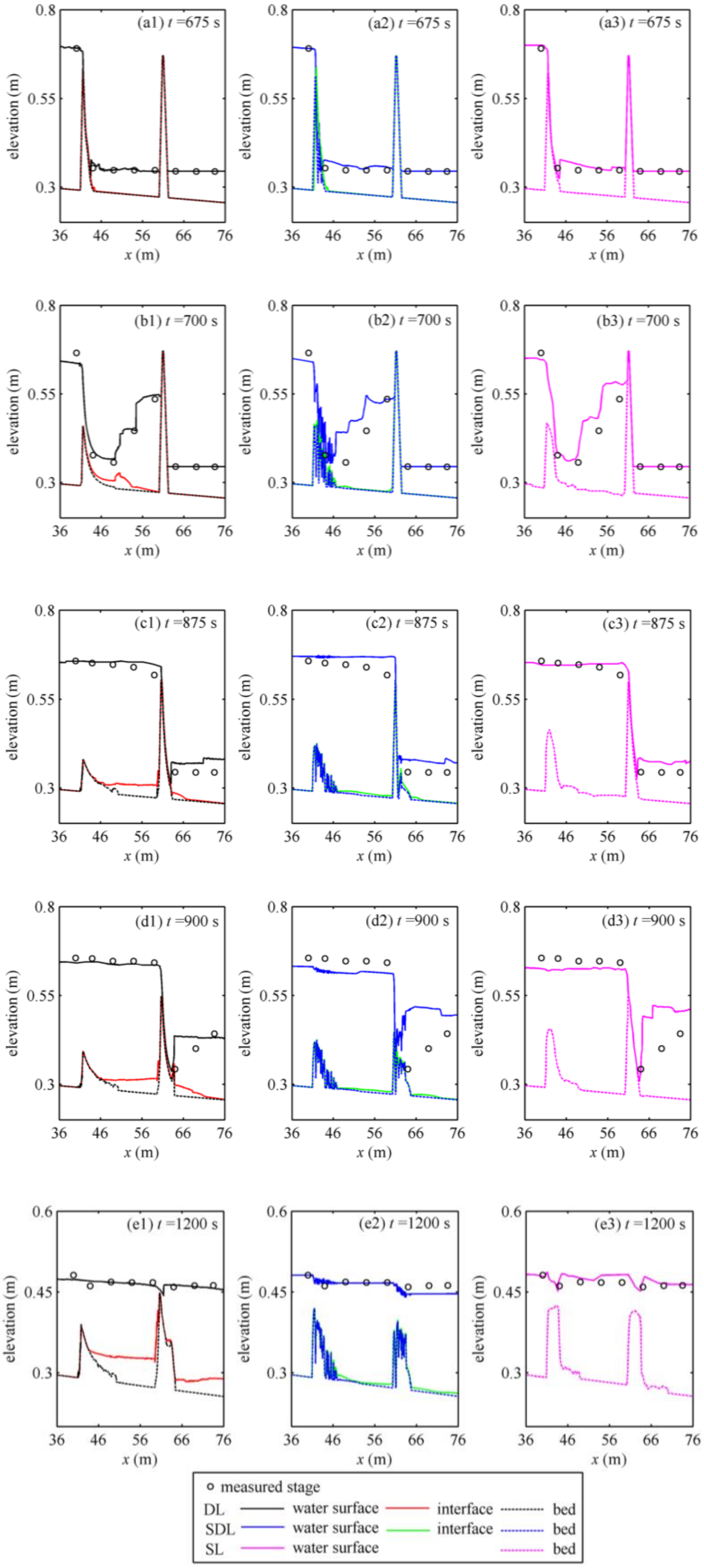

Figure 3.7 Water surface, interface and bed profiles for cascade landslide dam failure

Table 3.2 L_{st}^{1} of DL, SDL and SL models for a single landslide dam failure (Test Case 3.2)

Time	t =410 s	t =430 s	t =450 s	t =600 s	Average
DL	0.12%	6.52%	8.54%	4.43%	4.90%
SDL	0.13%	13.89%	16.35%	6.85%	9.31%
SL	0.13%	8.53%	11.45%	6.45%	6.64%

Table 3.3 L_{st}^{1} of DL, SDL and SL models for cascade landslide dam failure (Test Case 3.3)

Time	t =675 s	t =700 s	t =875 s	t =900 s	t =1200 s	Average
DL	0.9%	4.26%	8.19%	11.18%	3.72%	5.65%
SDL	1.52%	13.48%	11.45%	16.68%	4.05%	9.44%
SL	1.02%	5.24%	9.06%	14.84%	3.89%	6.81%

3.4. Progressive Failure of a Dike

This subsection aims to evaluate the three models' ability to reproduce the morphological evolution of a breaching dike. An experimental test (Test-18) is revisited, labelled as Test Case 3.4 presently, which was carried out by Schmocker and Hager (2012) in a flume 8 m long, 0.4 m wide and 0.70 m high. In this case, the initial single dike was 0.2 m high, 0.2 m wide and located at about 1.0 m from the inlet of the flume. The initial upstream and downstream slopes of the dike were both 1:2. The median diameter of the non-cohesive dike material was 2.0 mm and the specific gravity of the sediment was 1.65. The inlet unit-width discharge was 0.08 m^2/s. The initial water depths immediately upstream and downstream of the dike were 0.2 m and 0.0 m, respectively. At the inlet boundary, flow discharge was specified, and the water depth and velocity were determined by the method of characteristics. A free flow was imposed at the channel end as the downstream boundary condition, following Pontillo et al. (2010) for similar test cases using the two-phase model developed by Greco et al.

(2008).

For the SDL model, sediment concentration C_s of the sediment-laden layer is assumed to be 0.1. The modification coefficients ϕ adopted in the DL and SL models are both 6.0. The interface roughness n_i adopted in the DL and SDL models is set to be 0.006 m$^{-1/3}$ s. For the three models, bed roughness n_b is 0.015 m$^{-1/3}$ s.

Fig. 3.8 shows the water surface and bed profiles computed from the DL, SDL and SL models, along with the measured bed elevation and interface computed from the DL and SDL models. Overall, both the DL and SL models can reasonably reproduce the breaching process of the dike. As seen from Fig. 3.8, the DL model performs the best, followed by the SL model, and the SDL model performs the worst due to serious non-physical oscillations. Actually this observation is corroborated quantitatively by the values of L_{bd}^1 (Table 3.4). The average L_{bd}^1 value of the DL, SDL, SL models are 10.63%, 13.83% and 10.94% respectively. Obviously, the maximum error is due to the SDL model. Pontillo et al. (2010) modelled similar experimental cases, and the root-mean-square error, instead of the L^1 norm, was used to measure the discrepancies between computational results and measured data. Therefore, a comparison of the performances of the DL and two-phase models may not be strictly justified. Nevertheless, purely from illustrations, the agreement of the DL and SL models with the measured bed profile (Fig. 9) is essentially equivalent to or appreciably better than its counterpart shown in Pontillo et al. (2010, Figs. 2 to 5), which was claimed to be an improvement over the traditional De Saint-Venant-Exner model.

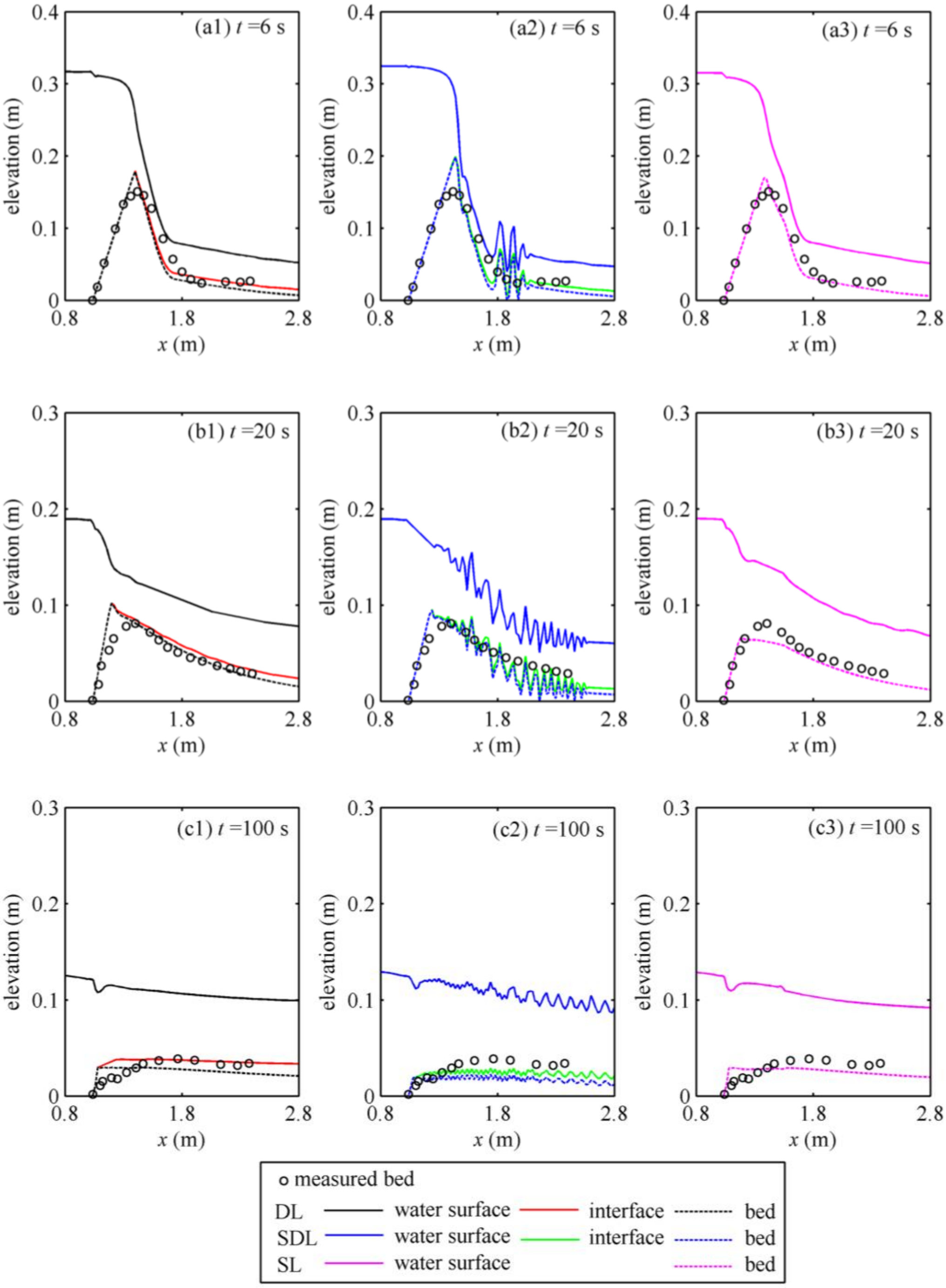

Figure 3.8 Water surface, interface and bed profiles for a dike breach

Table 3.4 L_{bd}^{1} of DL, SDL and SL models for Test Case 3.4

Time	*t* =6 s	*t* =20 s	*t* =100 s	Average
DL	13.64%	9.94%	8.36%	10.64%
SDL	17.52%	11.42%	12.56%	13.83%
SL	12.67%	10.15%	9.89%	10.90%

3.5. Discussion

3.5.1. Sensitivity analysis

Numerical tests are conducted to evaluate the sensitivity of the computational results to model parameters. In general, the results with tuned parameters are qualitatively similar to those shown in Figs. 3.1-3.2 and Figs. 3.4-3.8 when compared with the measured data.

Specifically, for Test Case 3.1, sediment concentration C_s of the lower layer in the SDL model is tuned by about 22% of the calibrated value (i.e., $C_s = 0.22 \pm 0.05$). Shown in Fig. 3.9 are the water surface and bed profiles along with the interface computed from the SDL model, corresponding to different sediment concentrations presumed for the lower sediment-laden flow layer. In Table 3.5 the corresponding L^1 values are provided. From Fig. 3.9, it is found that the computational results of the SDL model are very sensitive to the presumed value of C_s. This is apparently echoed by the L^1 values (Table 3.5). Comparatively, L^1_{in} is most sensitive to C_s, whilst L^1_{st} and L^1_{bd} are less sensitive. At $t = 1.5$ s, L^1_{in} is nearly doubled in response to a variation of C_s by 22% (Table 3.5). It is also shown in Table 5 that the sensitivity of the L^1 values to C_s would increase with time.

Likewise, the modification coefficient ϕ in the DL model is tuned by 50% of its calibrated value (i.e., $\phi = 2.0 \pm 1.0$), and the results are shown in Figure 3.10 and Table 3.6. Indeed, the results are appreciably sensitive to the tuned parameter ϕ. As seen from Fig. 3.10, the bed deformation seems to be relatively more sensitive to the value of ϕ than the stage and interface, which is clearly supported by the L^1 values in Table 3.6.

This is in contrast to the observation that the interface profile is most sensitive to C_s in the SDL model (Fig. 3.9 and Table 3.5). Physically, it is determined by the fact that ϕ is directly embedded in the relationships for sediment entrainment in the DL model, i.e., Eqs. (2.38) and (2.44), and therefore in the bed deformation Eq. (2.32), whereas C_s is explicitly involved in the equations of the two layers of the SDL model, i.e., Eqs. (2.21-2.24), instead of the bed evolution Eq. (2.19). Most notably, the sensitivity to ϕ in the DL model is considerably constrained compared with that to C_s in the SDL model. This is substantiated by the fact that the increase of L_{st}^1, L_{in}^1, L_{bd}^1 of the DL model in response to the change of ϕ (by 50 %) is considerably smaller than its counterpart of the SDL model in connection with the change of C_s (by 22%), see Tables 3.5 and 3.6. Consequently, the computational results are more sensitive to the presumed sediment concentration C_s in the SDL model than to the modification coefficient ϕ in the DL model, by which a major limitation of the SDL model is characterized.

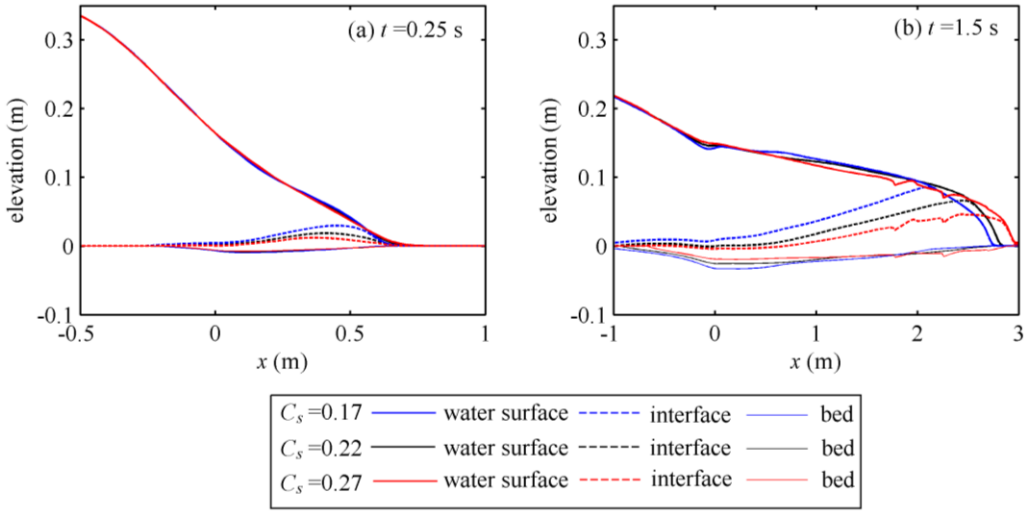

Figure 3.9 Water surface and bed profiles along with interface from the SDL model assuming different sediment concentrations

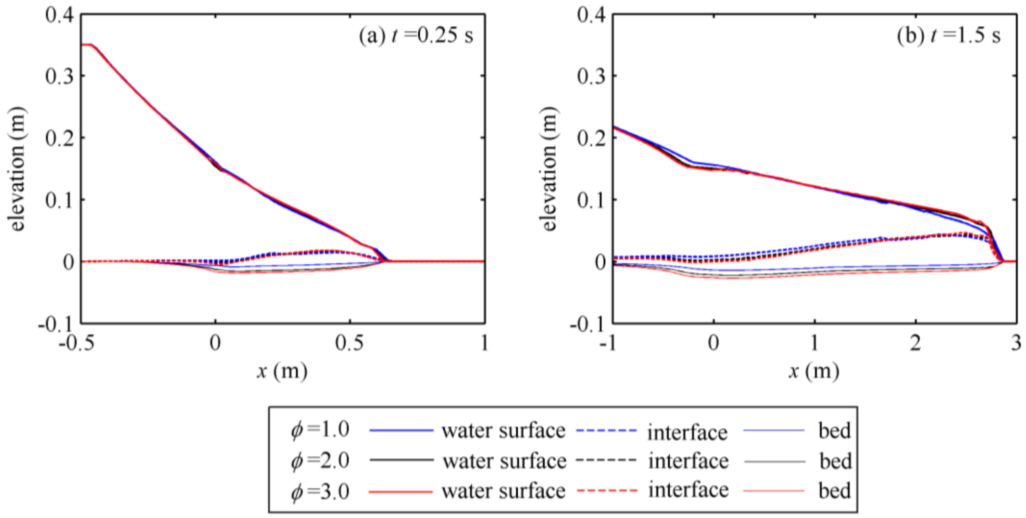

Figure 3.10 Water surface and bed profiles along with interface from the DL model assuming different modification coefficient ϕ

Table 3.5 L^1 Norm of SDL model with different C_s for Test Case 3

L^1	C_s	L^1 Norm	
		t =0.25 s	t =1.5 s
L^1_{st}	0.17	2.88%	6.19%
	0.22	2.75%	3.93%
	0.27	3.02%	5.97%
L^1_{in}	0.17	4.45%	7.16%
	0.22	3.11%	3.52%
	0.27	4.47%	7.09%
L^1_{bd}	0.17	5.01%	7.74%
	0.22	4.92%	5.04%
	0.27	5.49%	7.88%

Table 3.6 L^1 Norm of DL model with different ϕ for Test Case 3.1

L^1	ϕ	L^1 Norm	
		t =0.25 s	t =1.5 s
L^1_{st}	1.0	2.71%	4.13%
	2.0	2.68%	3.72%
	3.0	2.73%	3.91%
L^1_{in}	1.0	3.27%	4.34%
	2.0	3.12%	3.46%
	3.0	3.18%	4.15%
L^1_{bd}	1.0	6.33%	6.21%
	2.0	4.45%	4.47%
	3.0	5.89%	5.64%

For Test Cases 3.2, 3.3 and 3.4, numerical experiments are carried out to ascertain the sensitivity of the computational results of the DL model to the parameter ϕ. Generally, the stage, interface and bed deformation related to the tuned parameter ϕ are similar to those illustrated in Figs. 3.1-3.2 and 3.4-3.8 qualitatively. However, the L^1 values increase to a certain extent, as given in Tables 3.7, 3.8 and 3.9. Typically, as the modification coefficient ϕ of the DL model is tuned by one-third of the calibrated values for Test Cases 3.2, 3.3 and 3.4, the average values of L^1_{st} for Test Cases 3.2 and 3.3 and of L^1_{bd} for Test Case 3.4 increase by approximately 30-40%.

Table 3.7 L^1_{st} of DL model with different ϕ for Test Case 3.2

ϕ	t =410 s	t =430 s	t =450 s	t =600 s	Average
3.0	0.15%	9.32%	11.27%	7.11%	6.96%
4.5	0.12%	6.52%	8.54%	4.43%	4.90%
6.0	4.43%	8.83%	8.56%	4.52%	6.59%

Table 3.8 L^1_{st} of DL model with different ϕ for Test Case 3.3

ϕ	t =675 s	t =700 s	t =875 s	t =900 s	t =1200 s	Average
3.0	1.05%	6.22%	11.88%	13.28%	4.68%	7.42%
4.5	0.9%	4.26%	8.19%	11.18%	3.72%	5.65%
6.0	4.54%	6.67%	11.06%	12.09%	3.83%	7.66%

Table 3.9 L^1_{bd} of DL model with different ϕ for Test Case 3.4

ϕ	t =6 s	t =20 s	t =100 s	Average
4.0	18.62%	13.56%	9.69%	13.96%
6.0	13.64%	9.94%	8.36%	10.64%
8.0	17.69%	14.27%	10.83%	14.26%

3.5.2. Variation of sediment concentration

Theoretically, both the DL and SL models are built upon the fundamental mass conservation law for sediment, so they can reflect the variation of sediment concentration in space and time. To illustrate this, the sediment concentration profiles from the DL, SDL and SL models for the instantaneous full dam-break case (Test Case 3.1) are shown in Fig. 3.11. Here, for the DL and SDL models, the averaged sediment concentration over the whole flow depth is defined as $C_h = C_s h_s / (h_w + h_s)$. According to the DL model, at 0.25 s following the dam-break, sediment concentration C_s in the lower layer has attained a rather high value of approximately 0.3, and at 1.5 s it is characterized by spatial expansion and also considerable decrease except around the forefront of the flood wave. It is apparent that C_s varies substantially in space and time, as resolved by the DL model. Hence, the assumption of a constant sediment concentration C_s in the lower layer is not justified for the SDL model. The qualitative similarity of the longitudinal profiles of the whole depth-averaged sediment concentration C_h from the SDL model to those due to the DL model does not justify the SDL because it is the C_s, rather than C_h, that is directly embedded in the SDL model.

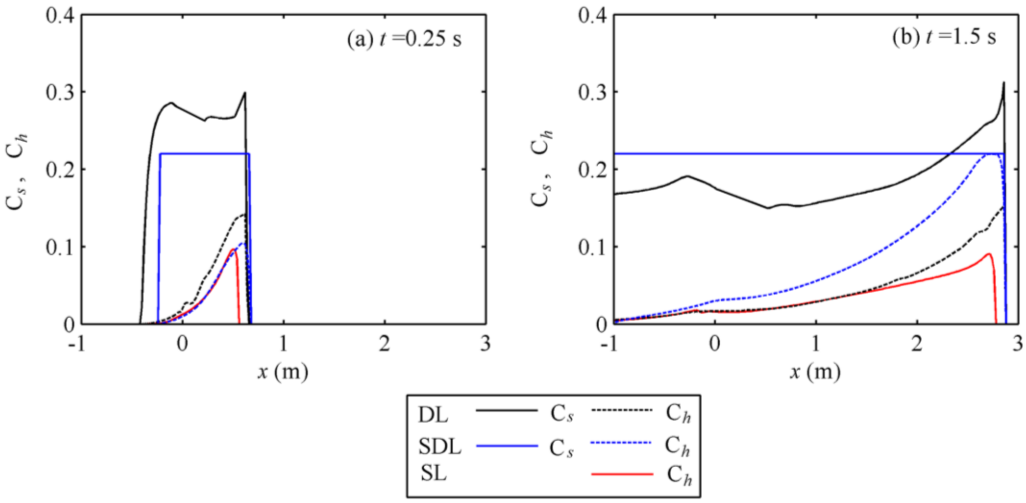

Figure 3.11 Sediment concentration profiles from the DL, SDL and SL models

3.6. Conclusion

The double layer-averaged model is applied for dam break flows over erodible bed due to instantaneous full dam break and progressive failures of a dike and landslide dams, either in a single setting or in cascade. Enhanced performance of the new model is demonstrated over a simplified double layer-averaged model and a single layer-averaged model. It justifies the physical necessity to incorporate sediment mass conservation in lieu of the assumption of constant sediment concentration generic to existing double layer-averaged models. The numerical algorithm proposed for the new model is effective and satisfactorily accurate.

CHAPTER 4 MODELLING RESERVOIR TURBIDITY CURRENTS AT LABORATORY-SCALE

4.1. Introduction

Reservoir turbidity current is formed as subaerial open-channel sediment-laden flow plunges into a reservoir. In general, turbidity currents can travel remarkable distances carrying large amounts of suspended sediment from the plunge point to the downstream. In reservoirs, turbidity currents are often the governing processes for the transport, entrainment and deposition of sediment (Fan and Morris 1992a). If the turbidity currents manage to arrive at the dam, it will be possible to flush sediment out of the reservoir. Otherwise, severe sedimentation in the reservoir will generally occur. Enhanced understanding of the whole process of reservoir turbidity currents, i.e., formation, propagation and recession, is critical to effective sediment and reservoir management, flood mitigation and fish habitat recovery.

Previous studies have focused on the threshold condition for the formation of turbidity current based on the densimetric Froude number at the plunge point, derived from laboratory experiments (Fan 1960; Singh and Shah 1971) or analytical models (Savage and Brimberg 1975; Akiyama and Stefan 1984; Parker and Toniolo 2007; Dai and Garcia 2009; Li et al. 2011). However, these cannot provide sufficient effective information to quantify the whole process of reservoir turbidity currents. Also, extensive laboratory experiments have greatly enhanced the understanding of turbidity current physics. In general, generating turbidity currents in the laboratory involves two classical approaches: 1) lock-exchange turbidity currents with release of a finite volume of water-sediment mixture; and 2) continuous turbidity currents with sustained inflow of water-sediment mixture. In both configurations, a reservoir of static or flowing clear water is first established. Water-sediment mixture is then introduced into the reservoir, either by withdrawal of the lock gate or by feeding water-sediment mixture continuously. Experimental lock-exchange turbidity currents are mainly deployed to understand their depositional characteristics and the propagation rate of the current front (e.g., Bonnecaze et al. 1993, 1995; Dade and Huppert 1995; Hallworth and Huppert 1998; De Rooij and Dalziel 2009); and the durations and features of the three stages of lock-exchange turbidity currents themselves (Simpson 1997). Nevertheless, it is recognized that lock-exchange turbidity currents substantially differ from reservoir turbidity currents that are generally controlled by both the upstream and downstream boundary conditions. However, they contribute greatly to enhanced understanding of turbidity current physics and provide valuable data to test the model. Experimental continuous turbidity currents have been mainly used to investigate the depositional and evolutional characteristics of turbidity (Hürzeler et al. 1996; Lee and Yu 1997; Gladstone et al. 1998), the vertical structure of the currents (Altinakar et al. 1996; Nourmohammadi et al. 2011; Eggenhuisen and McCaffrey 2012), and the effects of turbulence structure on sediment distribution (Baas et al. 2005). Especially, Lee and Yu (1997) performed a series of tests to investigate the formation and propagation of turbidity currents due to sustained inflow and in particular demonstrated the impacts of various upstream and downstream boundary conditions. Also, they investigated the densimetric Froude number at both the incipient and stable plunge points. In addition, experiments on saline/brine density currents have also been conducted to add to the understanding of turbidity currents, such as the vertical velocity profiles (Kneller et al. 1997, 1999; Sequeiros et al. 2010) and current structure in meandering and sinuous channels (Keevil et al. 2006, 2007), sediment entrainment estimation (Garcia and Parker 1993), water entrainment estimation (Hallworth et al. 1993), evolution mechanism of lock-exchange turbidity currents (Huppert and Simpson 1980; Amy et al. 2005) etc. As the shear stress and structure for experimental density and turbidity currents are physically similar (Cossu and Wells 2012), it adds to the understanding of turbidity current physics through saline/brine density current.

The model is benchmarked against a spectrum of experimental turbidity currents induced by lock-exchange (Bonnecaze et al. 1995; Hallworth and Huppert 1998) and sustained inflow (Lee and Yu 1997).

4.2. Lock-exchange Turbidity Currents

4.2.1. One-dimensional lock-exchange turbidity currents

A systematic series of experiments on one-dimensional lock-exchange turbidity currents were conducted by Hallworth and Huppert (1998) at University of Cambridge. The horizontal channel was 2 m long, 0.2 m wide and 0.25 m high. The location of lock gate was 0.03 m. Initially, static water-sediment mixture and clear water with both depths of 0.10 m stand on the left and right of the lock gate, respectively. The median diameter of sediment was 9 µm and the density was 3270 kg/m^3. Here two experimental cases with relatively low initial sediment concentrations ($c_{s0} =$ 0.025 and $c_{s0} =$ 0.15) were revisited, thus the effects of non-Newtonian fluid is precluded. The upstream and downstream boundary conditions for both the clear-water flow layer and the turbidity current layer were set as rigid boundary conditions. E_s is calculated using Eq. (2.42). The spatial step Δx is 0.005 m. The bed roughness n_b and the interface roughness n_i are determined by fitting to the measured front location. It is found that $n_b =$ 0.015 m$^{-1/3}$ and $n_i =$ 0.005 m$^{-1/3}$ lead to satisfactory agreement with measured data.

Fig. 4.1 shows the computed turbidity current front location against time and final deposition density D/M_0 against distance along with measured data, respectively. The final deposition density has been normalized by initial mass loading, M_0. From Fig. 4.1, the computed advance of the current front and final deposition density are in fairly good agreements with measured data. It is seen from Fig. 4.1(a) that the turbidity currents propagate fast at the beginning and the speed decreases gradually along with time. Moreover, the larger the sediment concentration (corresponding to higher driving force), the faster turbidity currents propagate. Fig. 4.1(b) illustrates that turbidity currents deposit more sediment as the initial sediment concentration increases. And the final deposition density has a maximum value near the release point and decreases asymptotically along the channel.

Fig. 4.2 illustrates the evolution process of 1D lock-exchange turbidity current for c_{s0} = 0.15, as represented by the interface profiles at several times. After the initial collapse due to the withdrawal of lock gate, turbidity currents are formed as the turbidity volume slumps and plunges into the standing clear water because of the driving force arising from the density difference [Fig. 4.2(a)]. As the current propagates further downstream, the thickness of the current decreases greatly [Fig. 4.2(b)].

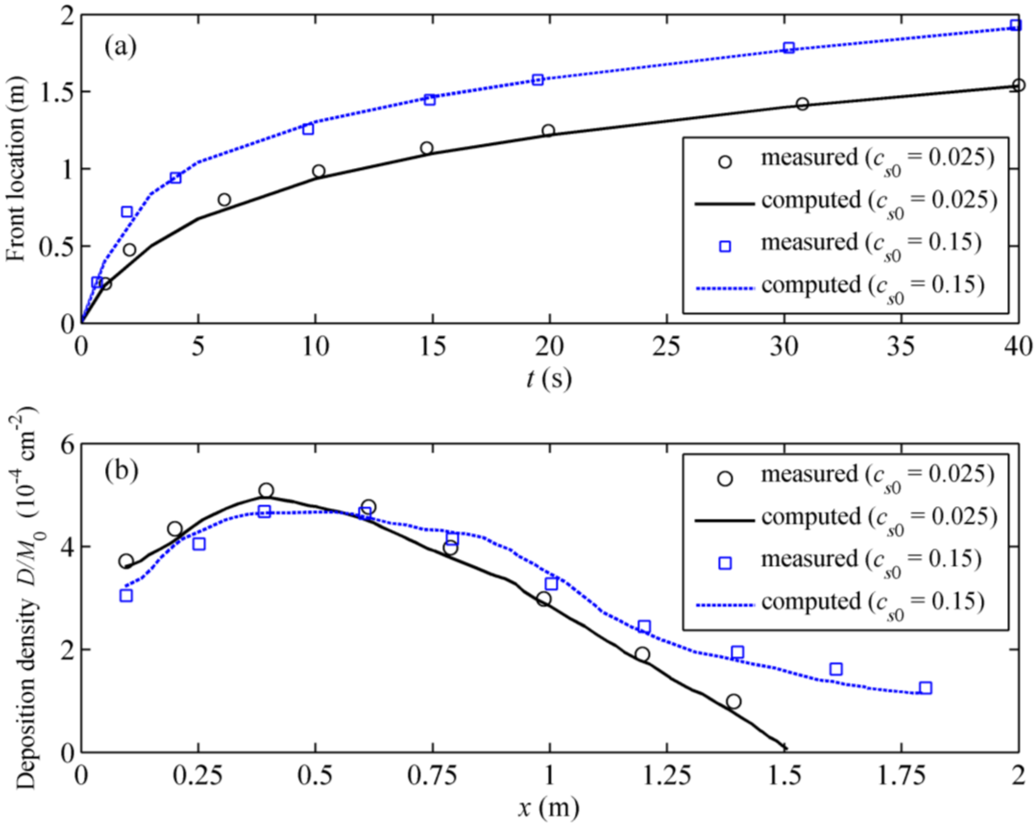

Figure 4.1 Numerical solutions compared with measured data for 1D lock-exchange turbidity current: (a) front location, and (b) final deposition density

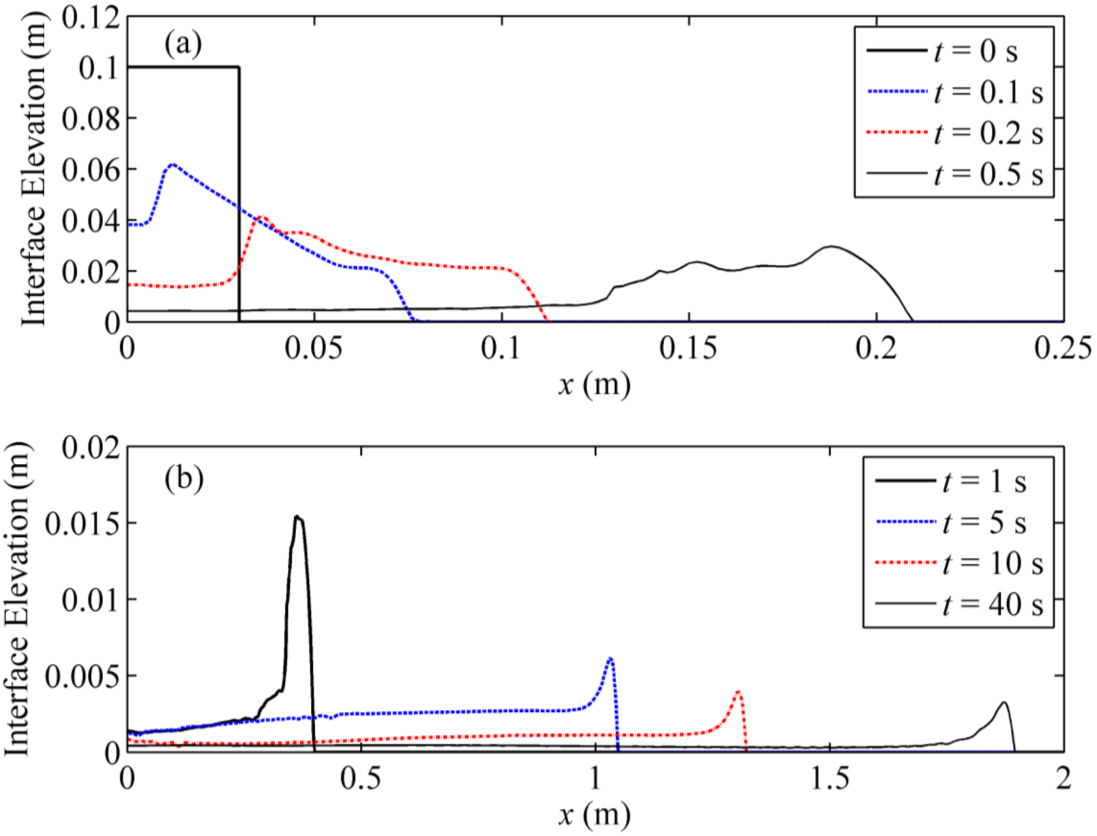

Figure 4.2 Interface profiles showing the evolution of 1D lock-exchange turbidity current (c_{s0} = 0.15)

4.2.2. Two-dimensional lock-exchange turbidity currents

The two-dimensional (2D) experimental axisymmetric turbidity currents tested by Bonnecaze et al. (1995) at University of Cambridge are numerically revisited to further test the present 2D double layer-averaged model. A plan view sketch of the flume is given in Figure 4.3. The flume consists of a rectangular part (0.038 m wide and 0.306 m long) and a radial part (the width expands from 0.038 to 0.294 m within 1.83 m). A lock gate is placed at the centre of the rectangular part, which separates the flume-filled water-sediment mixture on the left side and clear water on the right side. The initial thickness of the turbidity volume and clear water is 0.14 m. Turbidity currents are initiated by instantaneous vertical withdrawal of the lock gate. The median diameter of the sediment was 37 μm and its density was 3217 kg/m^3. Three runs are conducted with different initial sediment concentrations: c_{s0} = 0.019, 0.01 and 0.005. E_s is calculated using Eq. (2.42). The spatial steps Δx and Δy are both 0.005 m. The bed roughness n_b and the interface roughness n_w are determined by fitting to measured front location. It is found that n_b = 0.015 m$^{-1/3}$ and n_i = 0.005 m$^{-1/3}$ lead to satisfactory agreements with measured data.

Fig. 4.4 shows the turbidity current front location against time and the final deposit density plotted versus the radial distance, respectively. The radial distance is measured from the ghost origin as indicated in Fig. 4.3, which is set to be the intersection of the extended walls of the radial flume. From Fig. 4.4, the computed advance of current front and the final deposition density by the present model agree with measured values rather well. Fig. 4.5 demonstrates the evolution process of 2D lock-exchange turbidity current for c_{s0} = 0.01, as indicated by the interfaces at several times.

Similar to the 1D cases above, when the lock gate is removed, the plunging of turbidity volume leads to the formation of turbidity currents [Fig. 4.5(b)]. The thickness of the current decreases sharply with the propagation of the current [Fig. 4.5(c and d)]. Initially the turbidity current advances fast, but decelerates gradually in time [Fig. 4.4(a)]. The higher the initial sediment concentration, the faster the turbidity current propagates, and naturally more sediment is deposited [Fig. 4.4 (b)]. The final deposition density has a maximum value near the ghost origin point and decreases asymptotically along the channel.

Lock-exchange turbidity currents are formed by the sudden release of a fixed volume of turbid water, and driven by difference in density from the ambient water, without any inflow at the upstream or outflow at the downstream boundary. Physically, double layer-averaged models are generally applicable, though a single layer-averaged model has been suggested to be approximately workable in deep ambient water (Bonnecaze et al. 1993). Nevertheless, it is recognized that lock-exchange turbidity currents substantially differ from reservoir turbidity currents that are generally controlled by both the upstream and downstream boundary conditions. Thus the following test is warranted of the present model against reservoir turbidity currents subject to sustained inflow (and in some cases outflow) at a laboratory scale.

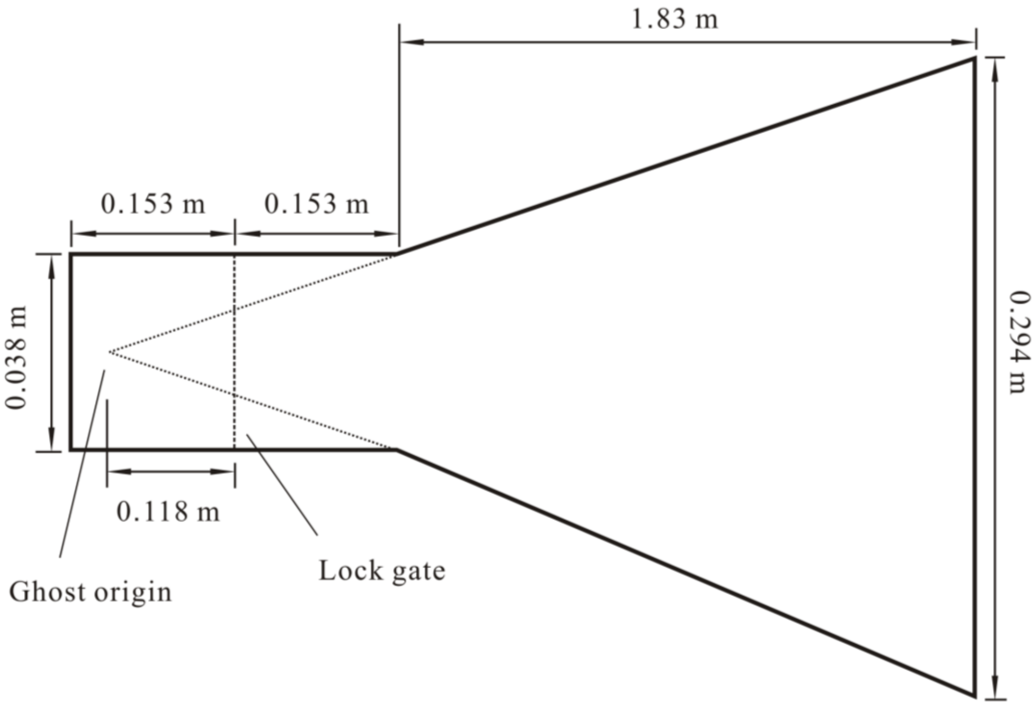

Figure 4.3 Plan view sketch of experimental flume (adapted from Bonnecaze et al. 1995)

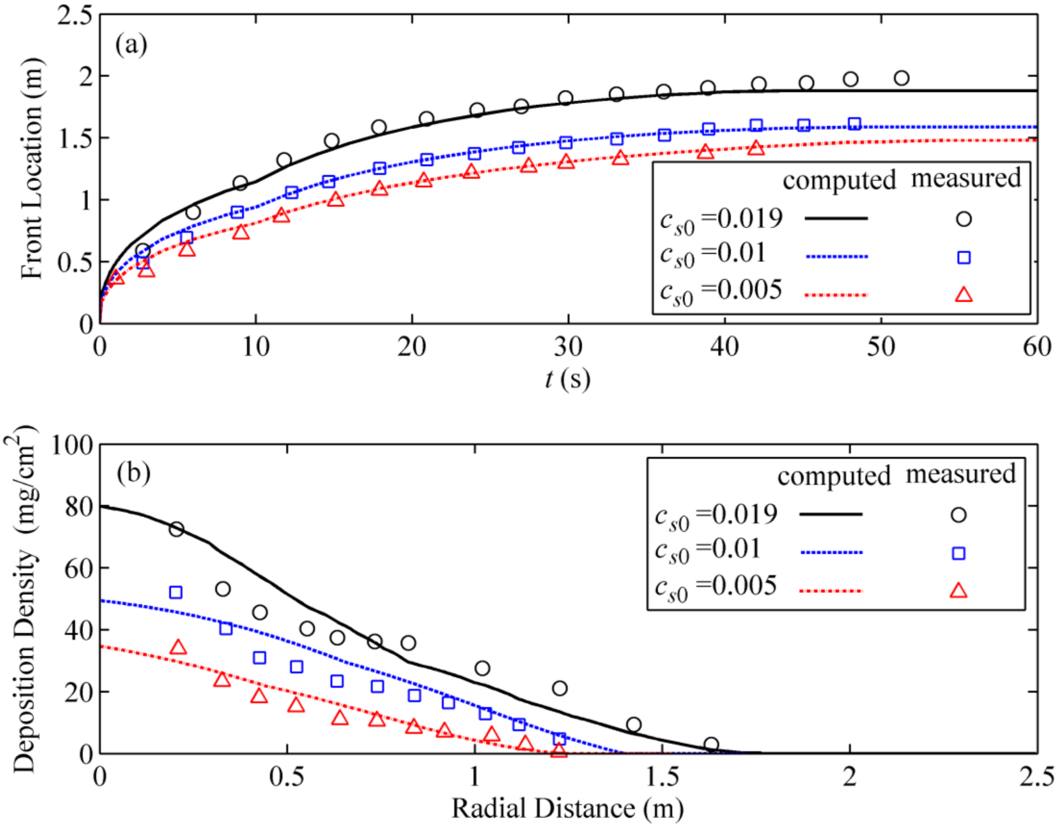

Figure 4.4 Numerical solutions compared with measured data for 2D lock-exchange turbidity current: (a) front location, and (b) final deposition density

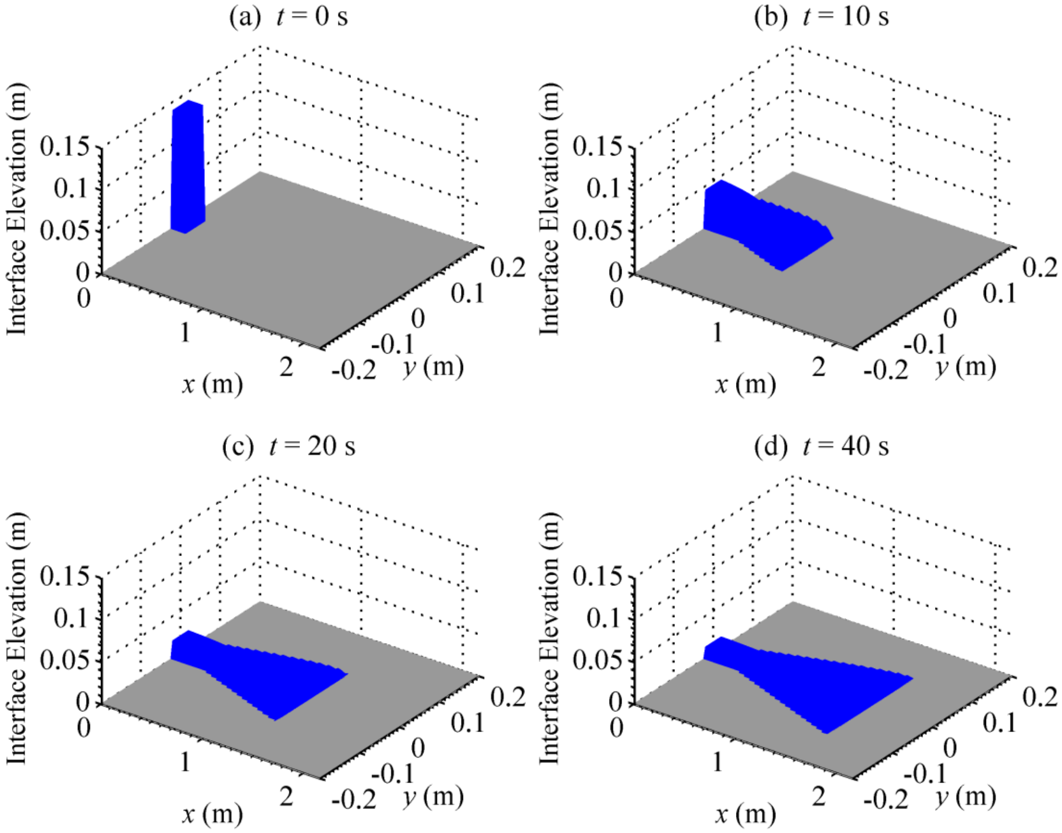

Figure 4.5 Evolution of 2D lock-exchange turbidity current (c_{s0} = 0.01)

4.3. Turbidity Currents Due to Sustained Inflow

This subsection focuses on the turbidity currents due to sustained inflow from the upstream, and in some cases subject to an outflow at the downstream, in contrast to lock-exchange turbidity currents considered above. A series of flume experiments were documented by Lee and Yu (1997) at National University of Taiwan. These experiments were carried out in a transparent flume of dimensions 20 m×0.2 m×0.6 m and bed slope 0.02. A receiving tank was installed at the end of sloping section. The suspended material was kaolin having a specific gravity of 2.65 and a mean particle size of 6.8 μm. During the experimental process, the flume was first filled with clear water to form a reservoir, and then open-channel sediment-laden flow was released from the head tank. In most runs, the outflow discharge q_{out} was set equal to the inflow discharge q_{in}, while in some other runs, q_{out} was kept zero all the time or from some instant. The inflow discharge and its sediment concentration were kept constant in each run of the experiments.

To demonstrate the performance of the model, Series B and C are revisited. Series B was performed to investigate the migration of the plunge point and corresponding variations of the plunge criteria, while Series C was designed to investigate the length of the plunge region and the hydraulic characteristics of the turbidity current over a long distance. The inflow conditions for all revisited experimental runs are summarized in Table 4.1.

In this connection, it is noted that the significant value of the systematic experiments by Lee and Yu (1997) has not been sufficiently exploited to support the development of analytical and computational models for reservoir turbidity currents. Only one run (Series C- TC 8) has ever been simulated with a vertical 2D model based on the Reynolds-averaged Navier-Stokes equations and κ-ε turbulence closure (Kassem and Imran 2001). In principle, the formation of the turbidity current could be resolved by this model, which, however, was not explicitly evaluated. Also, the impacts of the outflow as related to Series B - PP4 were not resolved at all, possibly because the flow system becomes unsteady and the computing cost is too high. There has been a plethora of single layer-averaged models (e.g., Choi 1998; Bradford and Katopodes 1999a, b; Sequeiros et al. 2009b; Hu et al. 2012; Lai and Wu 2013), but none has been verified against the observed data of Lee and Yu (1997).

Table 4.1 Summary of inflow conditions for all revisited experimental runs

Run	Series B Inflow conditions q_{in} (cm^2/s)	 c_s (10^{-3})	Run	Series C Inflow conditions q_{in} (cm^2/s)	 c_s (10^{-3})
PP 1	23.5	3.71	TC 1	24.23	4.36
PP 2	42.25	3.71	TC 2	24.76	7.16
PP 3	70.56	2.51	TC 3	42.25	3.63
PP 4	85.10	2.00	TC 4	41.63	7.27
PP 5	86.74	3.86	TC 5	41.78	10.78
PP 6	100.21	3.27	TC 6	68.01	2.36
PP 7	86.01	5.61	TC 7	68.22	4.27
PP 8	99.64	4.98	TC 8	67.90	6.67
PP 9	101.20	6.60	TC 9	68.28	8.59
PP 10	134.46	4.85	TC 10	85.27	2.10
			TC 11	85.45	3.88
			TC 12	85.21	5.43
			TC 13	84.70	7.37
			TC 14	97.56	3.10
			TC 15	97.52	4.73
			TC 16	97.40	5.99
			TC 17	96.47	7.81
			TC 18	116.07	6.81

For this modelling exercise, the computational domain consists of the sloping section without including the receiving tank at the far downstream end of the flume. It is assumed that the discharge at the end of the sloping section is equal to the outflow discharge because the receiving tank is rather short. At the inlet boundary, there was no clear-water flow layer; and as the inflow discharge was specified, the depth and velocity of the sediment-laden flow were determined by the method of characteristics. A downstream boundary condition is not required for the turbidity current as the computation is automatically terminated once the current reaches the downstream boundary. For the outlet boundary condition of the clear-water flow layer, the depth and velocity were determined by the method of characteristics as the outflow discharge was specified. The spatial step Δx is 0.025 m. The bed roughness n_b and the interface roughness n_w are first calibrated using measured data from Series B - PP 1, and then directly applied for the other cases. It is found that interface roughness $n_i =$ 0.005 m$^{-1/3}$ s and bed roughness $n_b =$ 0.015 m$^{-1/3}$ s lead to satisfactory agreement with measured data. E_s is determined according to Eq. (2.42) as ψ ranges between 4.0 and 20.0, which means partial erosion and deposition. It is also found that the maximum value of bed deformation is merely 3.4×10^{-5} m (not shown). Here, x_p is the distance between the plunge point and flume entrance, h_p is the current thickness at the plunge point and $\mathrm{F}_p = u_s / \sqrt{g'_p h_p}$, is the corresponding densimetric Froude number.

4.3.1. Turbidity current formation and propagation

Fig. 4.6 illustrates the formation and propagation processes of the turbidity current with unit-width inflow discharge 97.52 cm^2/s and volumetric sediment concentration 4.73×10^{-3}, corresponding to Run TC 15 (Table 4.1). It is noted that upstream of the plunge point, the interface is actually the water surface, characterizing that there is no clear water flow and thus the flow is essentially subaerial open-channel sediment-laden flow. As the turbid water flows forward, a separation becomes pronounced from the clear water in the reservoir [Fig. 4.6(b)]. Then the sediment-laden flow plunges to the bottom and begins to move as an underflow, i.e., turbidity current [Fig. 4.6(c-d)], of which the upper boundary is indicated by the “interface.” Succinctly, the formation process of reservoir turbidity current is characterized by the transition from subaerial open-channel sediment-laden flow to subaqueous turbid flow. At this stage, the plunge point is unstable and still moves forward. By $t > 160$ s approximately, the plunge point stabilizes and the current advances with a bulge-shaped head and elongated body.

It is noted that when the upper layer vanishes, Eq. (2.46) for the lower layer reduces to a system of equations of a traditional shallow water hydrodynamic and sediment model for open-channel sediment-laden flows (e.g., Cao et al. 2011c), which differs from that of a single layer-averaged model for turbidity currents (Hu et al. 2012). This is exactly why the present double layer-averaged model can resolve the formation process of reservoir turbidity current, characterized by the transition from open-channel sediment-laden flow to subaqueous turbidity current.

To date, the authors are not aware of any previous layer-averaged models that can resolve the formation process of the turbidity currents due to sustained inflow, though systematic experimental observations are available (e.g., Lee and Yu 1997). Most plausibly, this is because the currently available single layer-averaged models (e.g., Choi 1998; Bradford and Katopodes 1999a, b; Sequeiros et al. 2009b; Hu et al. 2012; Lai and Wu 2013) simply do not have the capability of resolving the interactions between the open-channel sediment-laden flow input from the upstream and the ambient water in the reservoir, irrespective of whether the latter is static or flowing as dictated by the outflow in relation to the reservoir operation schemes. It is most telling that the present double layer-averaged is warranted if the whole processes of reservoir turbidity currents are to be sufficiently resolved. This is further demonstrated in the following subsections, as compared against the observed data of Lee and Yu (1997) and the analytical formulations of Dai and Garcia (2009) and Li et al. (2011). Presented below are the characteristics at the plunge point, the streamwise profiles of the thickness, mean velocity and sediment concentration of the turbidity currents, as well as the impacts of the outflow at the downstream.

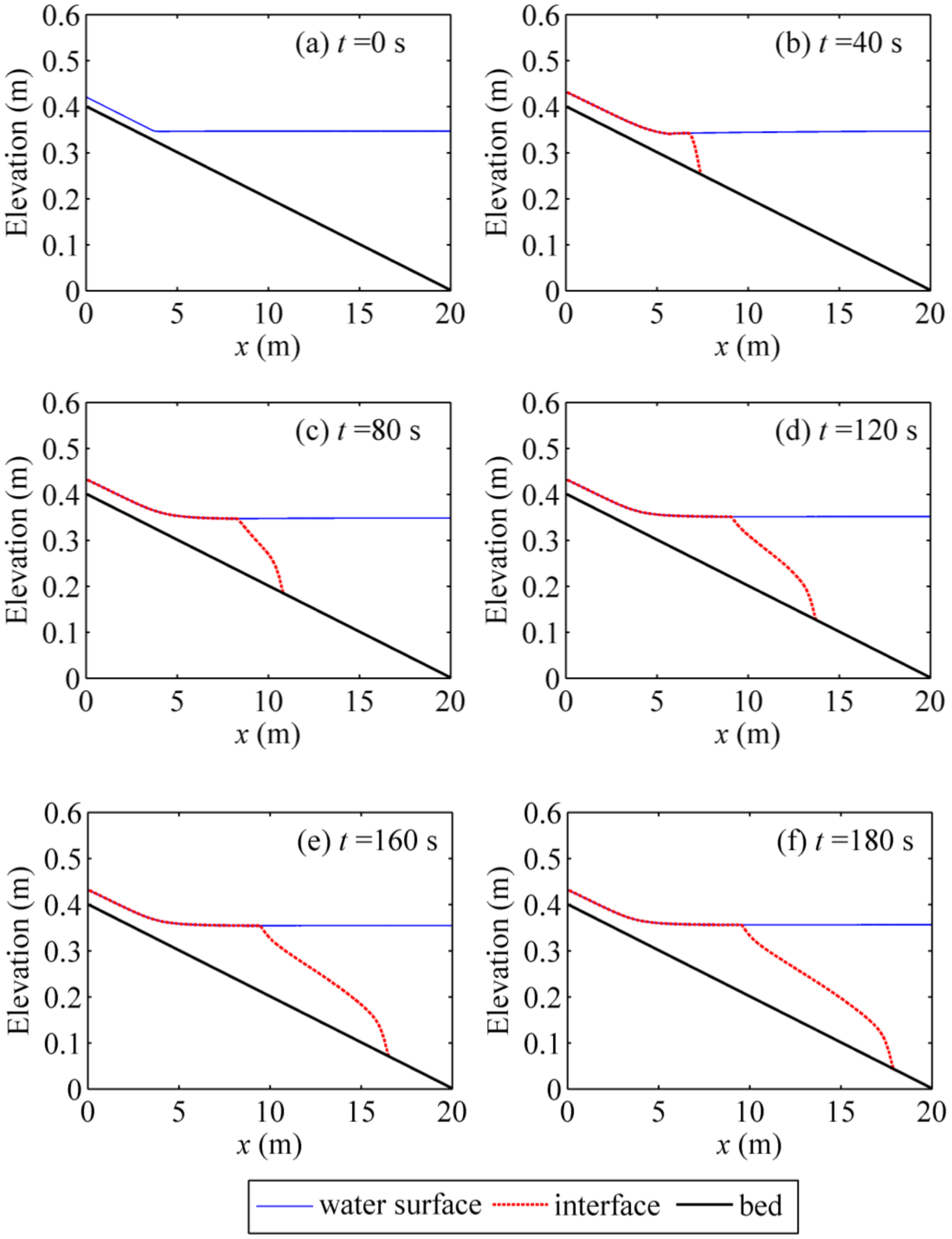

Figure 4.6 Turbidity current formation and propagation (Series C - TC 15)

4.3.2. Characteristics at the plunge point

Shown in Tables 4.2 and 4.3 are the parameters at the incipient and stable plunge points for Series B and Series C, corresponding to different inflow conditions. The analytical densimetric Froude number solution at the incipient plunge point developed by Li et al. (2011) is based on energy balance and includes the effects of the bed slope, sediment concentration and the discharge of the turbidity current. Dai and Garcia (2009) analyze the densimetric Froude number at the stable plunge point by taking into account the bed slope and inflow conditions. Tables 4.2 and 4.3 clearly illustrate that the computed results match the measured data and analytical results very well. It is shown that F_p at the incipient plunge point ranges approximately between 0.9 and 1.0, while the mean value of F_p at the stable plunge point varies around 0.6. Thus the incipient plunging occurs when F_p equals to 0.9~1.0, and F_p reduces as the plunge point migrates downstream. The plunge point finally reaches a stable condition, where F_p equals 0.6. And the h_p and F_p at the incipient plunge point as well as x_p, h_p and F_p at the stable plunge point increase with the increase of the inflow discharge, but decrease with the increase of sediment concentration. This is mainly because larger discharge or smaller sediment concentration corresponds to smaller value of Ri and thus induces more water entrainment.

Fig. 4.7 shows the computed relationship between h_p and $(q_p^2/g'_p)^{1/3}$ for Series B, including those not only at the incipient and stable plunge points, but also in between them. The theoretical results at the incipient plunge point according to Li et al. (2011) and at the stable plunge point due to Dai and Garcia (2009) are also included. The two dash lines represent respectively the incipient and stable plunge points, corresponding to $\mathrm{F}_p = 1.0$ and 0.6 proposed by Lee and Yu (1997). Echoing Tables 4.2 and 4.3, the computed results from the present model agree with the analytical results based on Li et al. (2011) and Dai and Garcia (2009) and also the observed data of Lee and Yu (1997) rather well. Fig. 4.8 shows the temporal variation of the plunge point location for three typical cases in Series B. It is seen that the location of the stable plunge point and also the time from the incipient to stable plunge point are distinct as the inflow discharge and sediment concentration vary. For a specific case (Series B- PP 4), the densimetric Froude number F_p decreases and the plunge depth h_p increases with time, and eventually both reach stable values (Fig. 4.9).

Table 4.2 Parameters at incipient and stable plunge points in relation to different inflow conditions (Series B)

RUN	Incipient				Stable			
	h_p (cm)		F_p		h_p (cm)		F_p	
	meas.	comp.	Li et al.	comp.	meas.	comp.	Dai & Garcia	comp.
PP 1	5.36	5.31	0.81	0.86	6.87	6.80	0.62	0.63
PP 2	7.40	7.37	0.96	0.97	9.28	9.39	0.65	0.62
PP 3	10.25	9.97	0.96	0.96	13.85	14.12	0.69	0.68
PP 4	12.56	12.48	1.02	1.03	17.15	17.25	0.64	0.64
PP 5	10.57	10.46	0.98	0.99	13.19	12.95	0.70	0.68
PP 6	13.54	13.63	0.95	0.97	16.32	16.40	0.72	0.69
PP 7	9.68	9.45	0.97	0.98	12.63	12.52	0.64	0.64
PP 8	12.84	12.43	0.97	0.99	14.37	14.60	0.66	0.67
PP 9	10.68	10.26	1.05	1.06	13.45	13.69	0.64	0.64
PP 10	12.68	12.38	0.94	1.03	18.09	17.95	0.68	0.67

Table 4.3 Parameters at incipient and stable plunge points in relation to different inflow conditions (Series C)

Run	Incipient		Stable					
	F_p		x_p		h_p		F_p	
	Li et al.	comp.	meas.	comp.	meas.	comp.	Dai & Garcia	comp.
TC 1	0.85	0.87	6.03	6.025	6.64	7.88	0.62	0.61
TC 2	0.89	0.90	5.52	5.50	5.62	6.43	0.64	0.63
TC 3	0.96	0.98	7.10	7.12	8.91	9.73	0.66	0.68
TC 4	0.95	0.94	6.29	6.31	7.17	7.94	0.65	0.67
TC 5	0.97	0.95	10.05	10.12	14.31	15.18	0.63	0.61
TC 6	0.99	0.96	10.05	10.12	14.31	15.18	0.63	0.61
TC 7	1.01	1.0	9.65	9.60	11.31	12.46	0.59	0.58
TC 8	0.98	0.99	8.05	8.03	10.53	11.13	0.65	0.62
TC 9	0.97	0.97	7.76	7.68	10.02	10.89	0.64	0.63
TC 10	0.99	0.96	11.24	11.26	17.04	17.85	0.66	0.65
TC 11	0.98	0.95	10.13	10.09	14.49	15.26	0.65	0.64
TC 12	1.02	1.03	9.46	9.56	12.97	13.69	0.64	0.66
TC 13	0.99	0.96	8.58	8.63	11.16	11.86	0.66	0.67
TC 14	0.98	0.97	10.96	10.98	16.51	17.20	0.67	0.65
TC 15	1.01	0.99	10.04	10.03	14.29	14.96	0.65	0.66
TC 16	0.99	0.98	9.55	9.68	13.18	14.29	0.67	0.64
TC 17	1.02	1.03	8.71	8.74	11.44	12.35	0.63	0.65
TC 18	0.99	0.96	9.68	9.78	9.68	10.03	0.67	0.65

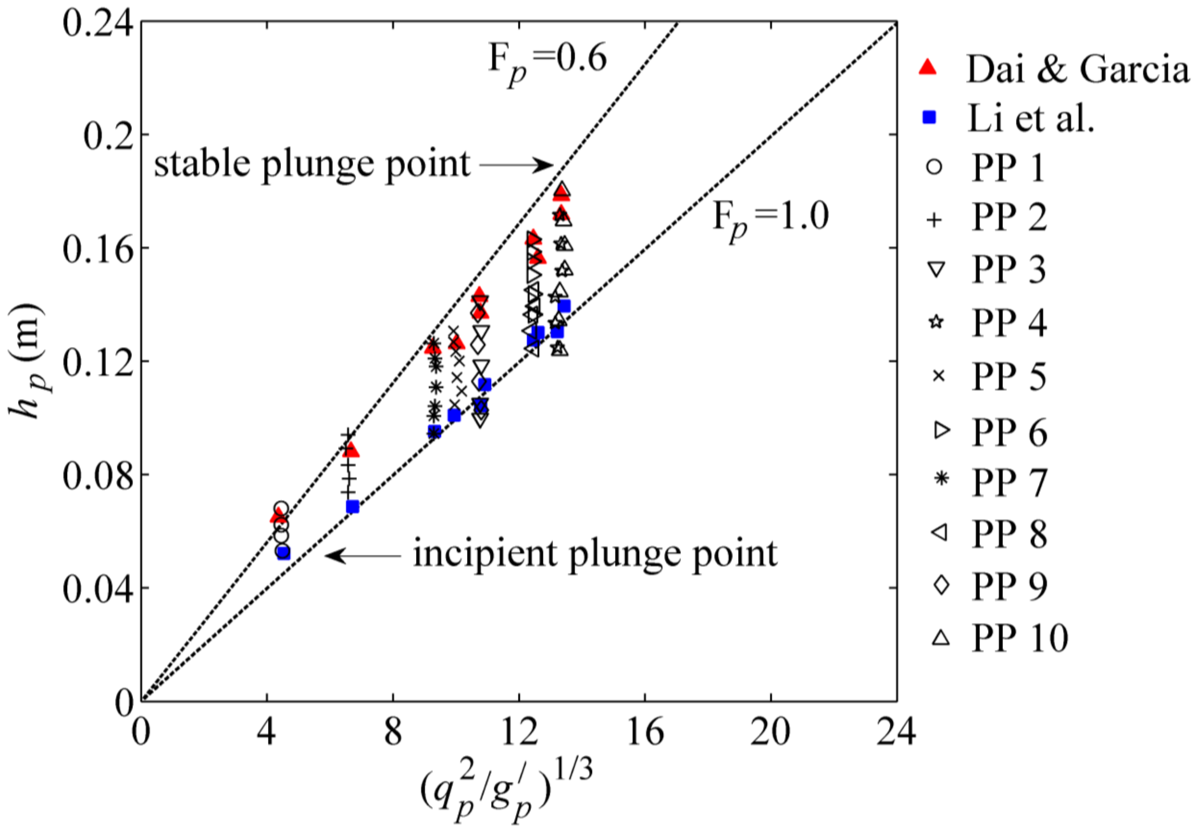

Figure 4.7 Computed turbidity current thickness at plunge point compared with analytical formulations, with two dash lines representing the incipient and stable plunge points due to Lee and Yu (1997)

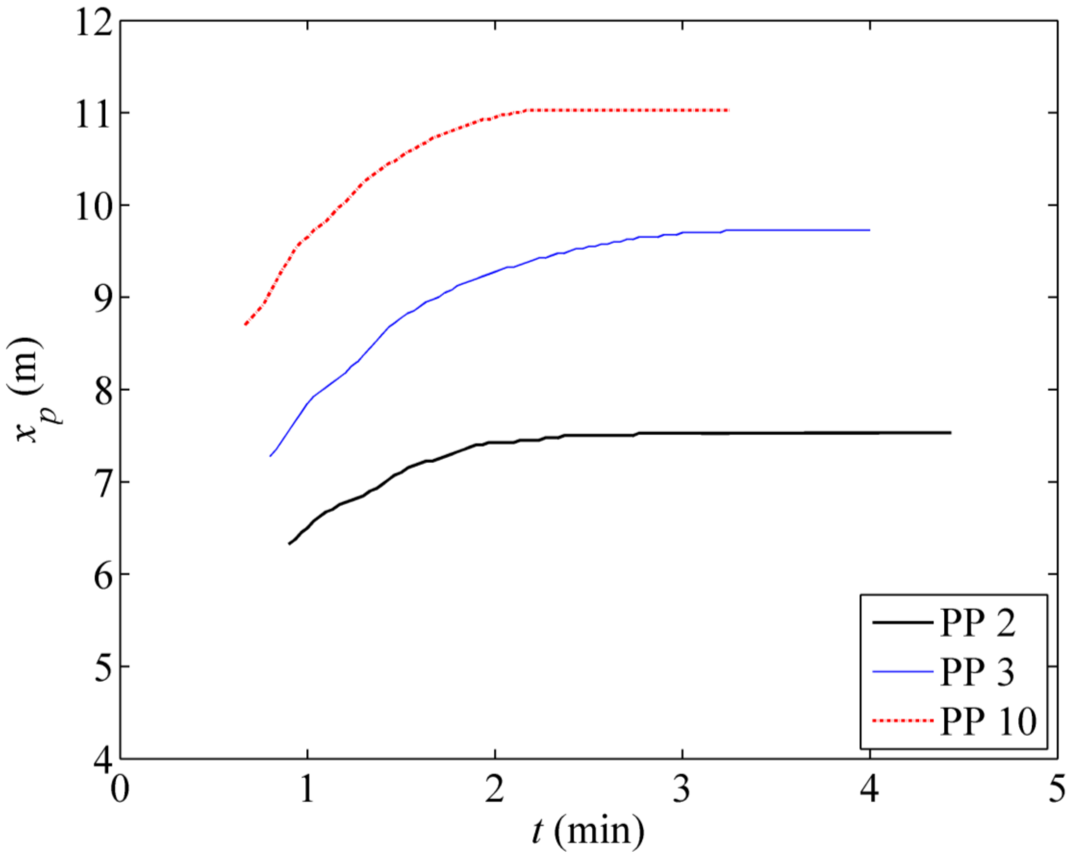

Figure 4.8 Temporal variation of plunge point location

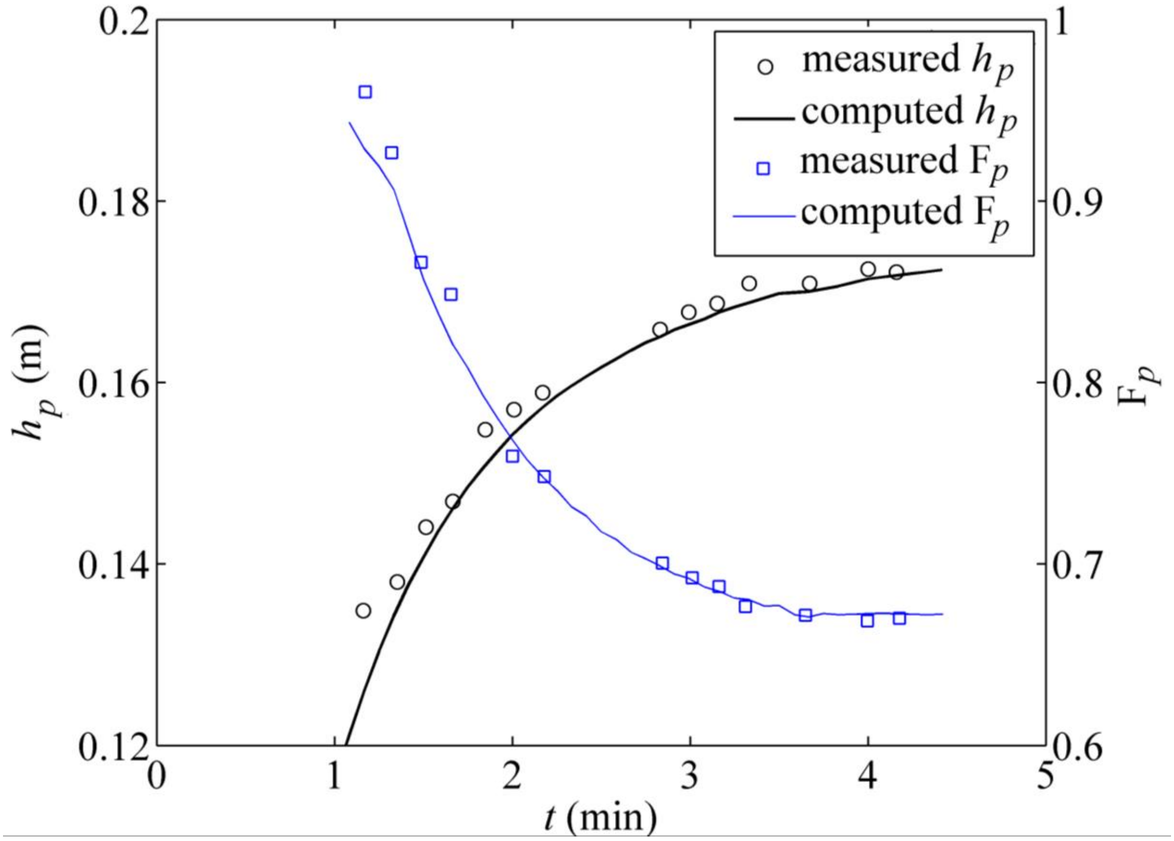

Figure 4.9 Computed densimetric Froude number and turbidity current thickness at plunge point compared with measured data (Series B-PP4)

4.3.3. Non-dimensional profiles of turbidity currents

Fig. 4.10 shows the spatial variation of dimensionless current thickness, velocity and sediment concentration computed by the present model along with measured data. Here, the data from Runs TC 5, TC 8, TC 12 and TC 15 at two selected cross-sections located at 11.3 m and 13.3 m respectively from the inlet of the flume are considered. Due to water entrainment, the discharge of the turbidity currents increases longitudinally and hence can be treated as an index of the distance from the plunge point. The data at $x =$ 11.3 m in run TC 5 are used as the reference values (i.e., $h_{s,x=11.3m}$, $u_{s,x=11.3m}$, $c_{s,x=11.3m}$, $q_{s,x=11.3m}$) to nondimensionalize the thickness, velocity, sediment concentration and discharge of the turbidity currents, which are represented by $\hat{h}_s$, $\hat{u}_s$, $\hat{c}_s$ and $\hat{q}_s$, respectively. It is seen from Fig. 4.10 that because of water entrainment, the thickness of turbidity currents increases longitudinally and thus the velocity and sediment concentration reduce accordingly. Overall, the observed non-dimensional thickness, velocity and sediment concentration profiles of the turbidity currents are well reproduced by the present model.

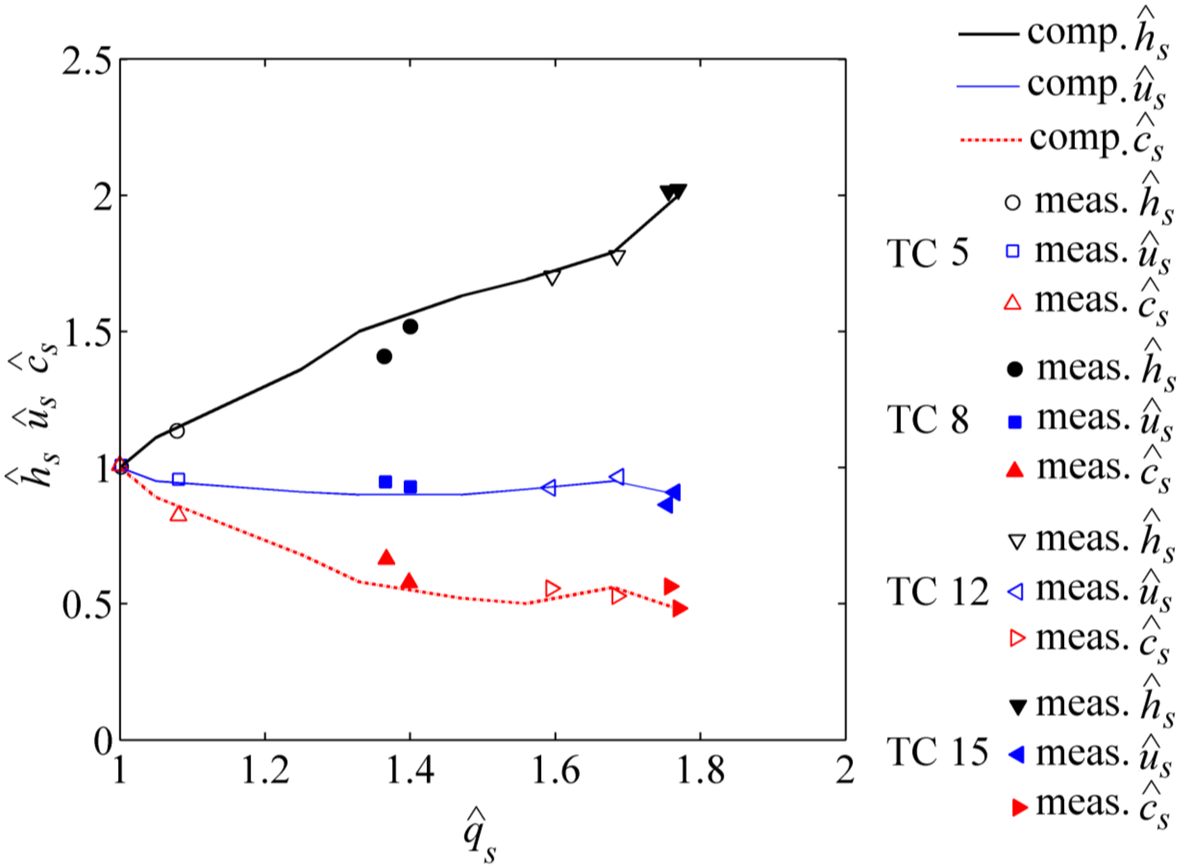

Figure 4.10 Computed dimensionless turbidity current thickness, velocity and sediment concentration compared with measured data

4.3.4. Impacts of downstream boundary conditions on turbidity currents

Fig. 4.11 illustrates the impacts of downstream boundary conditions on the turbidity currents in relation to Series B - PP4. The impacts are represented by variations in the plunge flow depth, plunge location and front location of the turbidity current. It is shown in Fig. 4.11 that if the outflow is cutoff from the initial state, the plunge point has not yet reached a stable state within the time period considered. Likewise, the stable plunge point becomes unstable as the outflow is terminated at 4.33 min. As the outflow increases, the water level in the reservoir will get lower. Most notably, an outflow of clear water in the upper layer generally leads to a decrease in the plunge depth [Fig. 4.11(a)], migration of the plunge location downstream [Fig. 4.11(b)], and acceleration of the propagation [Fig. 4.11(c)] of the turbidity current, and vice versa. Physically, a clear-water outflow facilitates a certain flow velocity of the upper layer, which leads to less interface resistance (Eq. 2.45) to the turbidity current and reduced water entrainment (Eq. 2.47).

From Figs. 4.7, 4.9, 4.10 and 4.11(a) as well as Tables 4.2 and 4.3, the computed results by the present model agree with measured values rather well, though subtle differences are spotted. This suggests that the turbidity currents are reasonably well resolved by the present model.

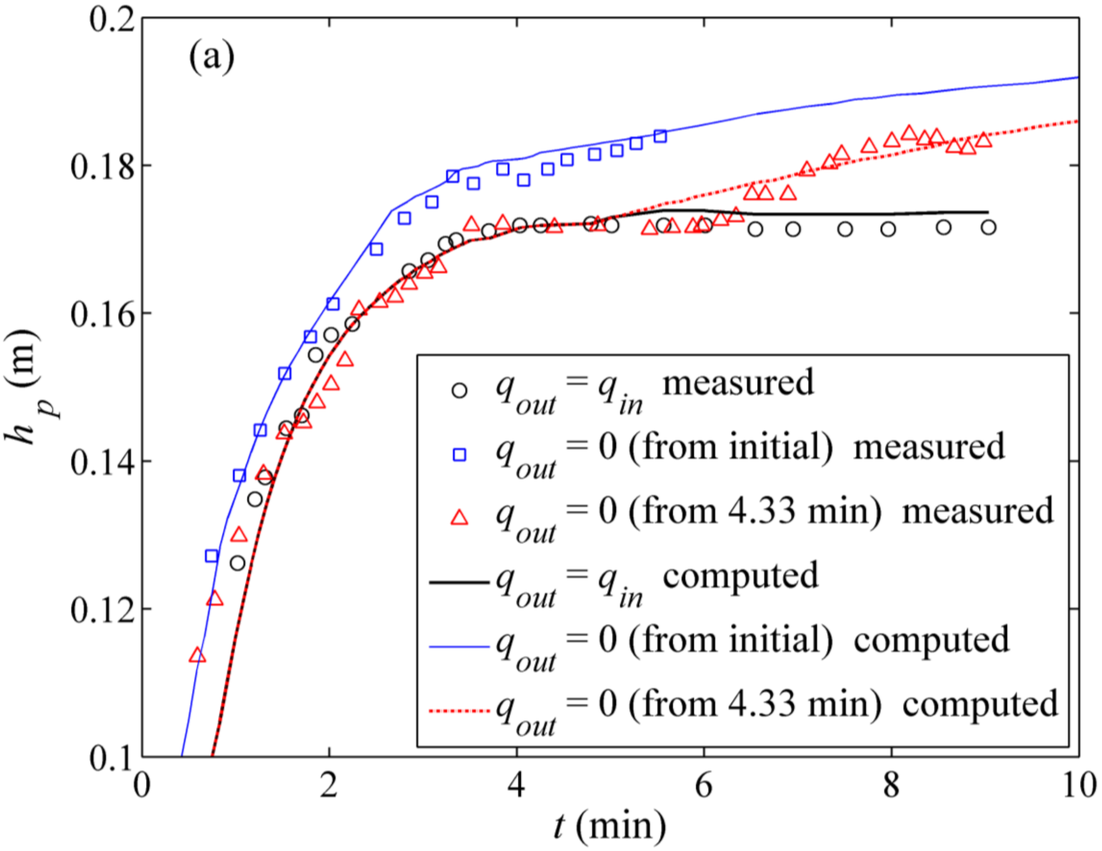
(a)
h_p (m)
0.2
0.18
0.16
0.14
0.12
0.1
0
2
4
6
8
10
t (min)
$q_{out} = q_{in}$ measured
$q_{out} = 0$ (from initial) measured
$q_{out} = 0$ (from 4.33 min) measured
$q_{out} = q_{in}$ computed
$q_{out} = 0$ (from initial) computed
$q_{out} = 0$ (from 4.33 min) computed

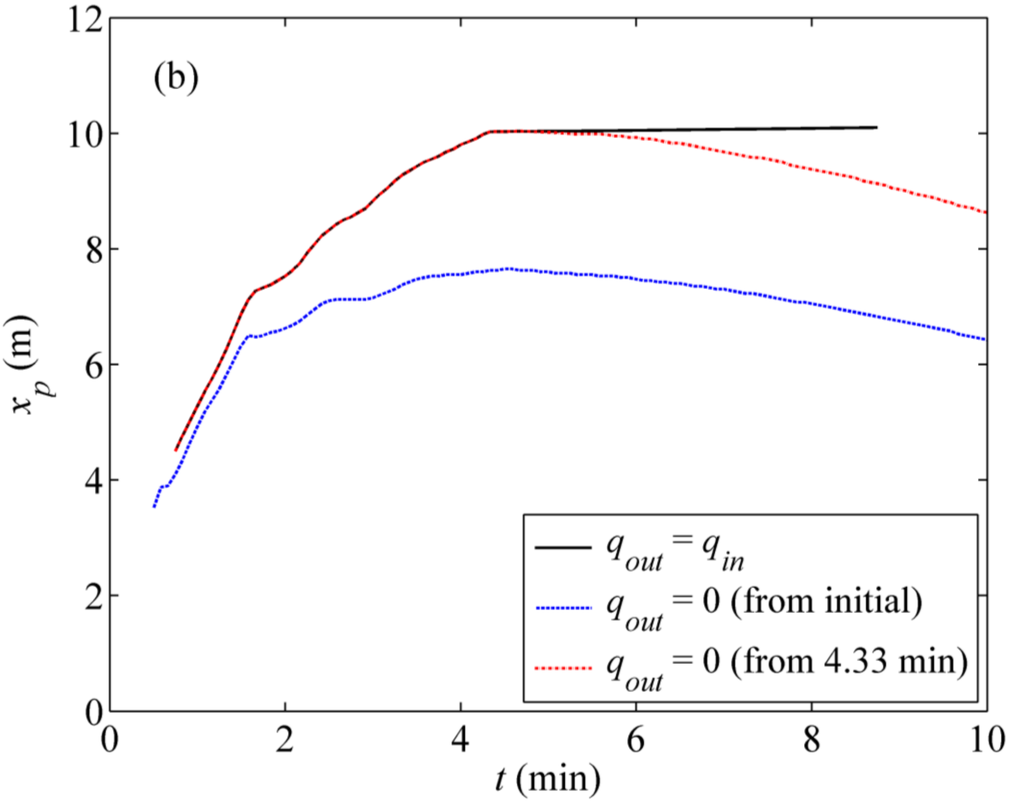
(b)
x_p (m)
12
10
8
6
4
2
0
0
2
4
6
8
10
t (min)
$q_{out} = q_{in}$
$q_{out} = 0$ (from initial)
$q_{out} = 0$ (from 4.33 min)

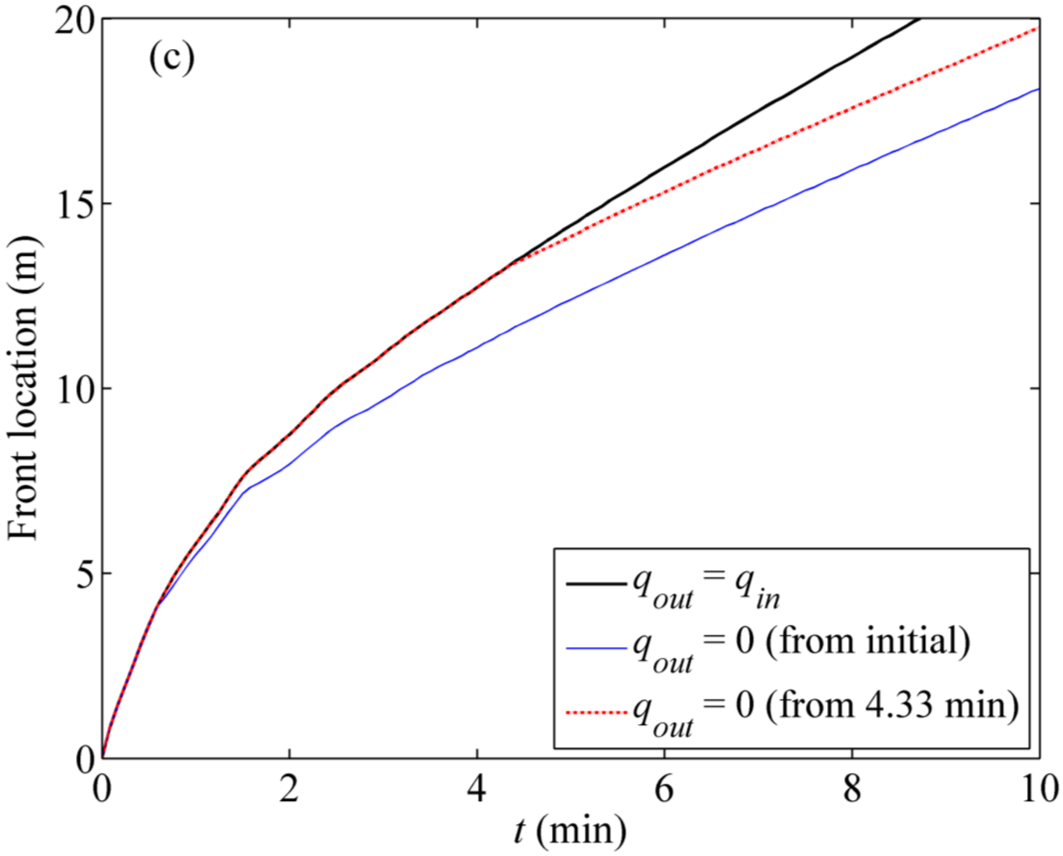

Figure 4.11 Impacts of downstream boundary conditions: (a) computed turbidity current thickness at plunge point compared with measured data, (b) computed plunge location, and (c) computed front location (Series B -PP 4)

4.3.5. Recession of turbidity current in an extended case

Here an extended case from Series B - PP 4 is numerically investigated to demonstrate the capability of the present model to reproduce the recession of turbidity currents. It is assumed that clear water inflow with a smaller unit-width discharge 40.0 cm^2/s, instead of sediment-laden open channel flow, is released when the plunge point reaches stable condition ($t >$ 4.33 min). And when the turbidity currents reach the downstream boundary, they are assumed to deposit within the receiving tank. Fig. 4.12 illustrates the formation, propagation and recession process of the turbidity current. Similar to the results above (Fig. 4.6), the turbidity current has been formed due to the sustained sediment-laden inflow at $t =$ 200 s [Fig. 4.12(a)]. After $t >$ 4.33 min, as clear water is released from the inlet, instead of sediment-laden inflow, the turbidity current continues to propagate downstream while its tail is rapidly replaced by the clear water released from upstream. Accordingly a complex flow regime is generated, which can be divided into five sections, as shown in Fig. 4.12(b). At the far upstream, there is a section of clear-water open-channel flow, which is followed by a section of "turbidity current", of which the density difference from the ambient water upstream is not enough compared to inertia and gravitational action to drive it flow upstream, in contrast to a traditional turbidity current. Next, a section of sediment-laden open-channel flow exists, and to the downstream is a section of turbidity current, followed by a section of clear-water flow. Later, the two sections of turbidity current merge, leading to the disappearance of the sediment-laden open-channel flow [Fig. 4.12(c)]. As time increases, the turbidity current recedes and is close to disappearance at $t =$ 2000 s [Fig. 4.12(d)].

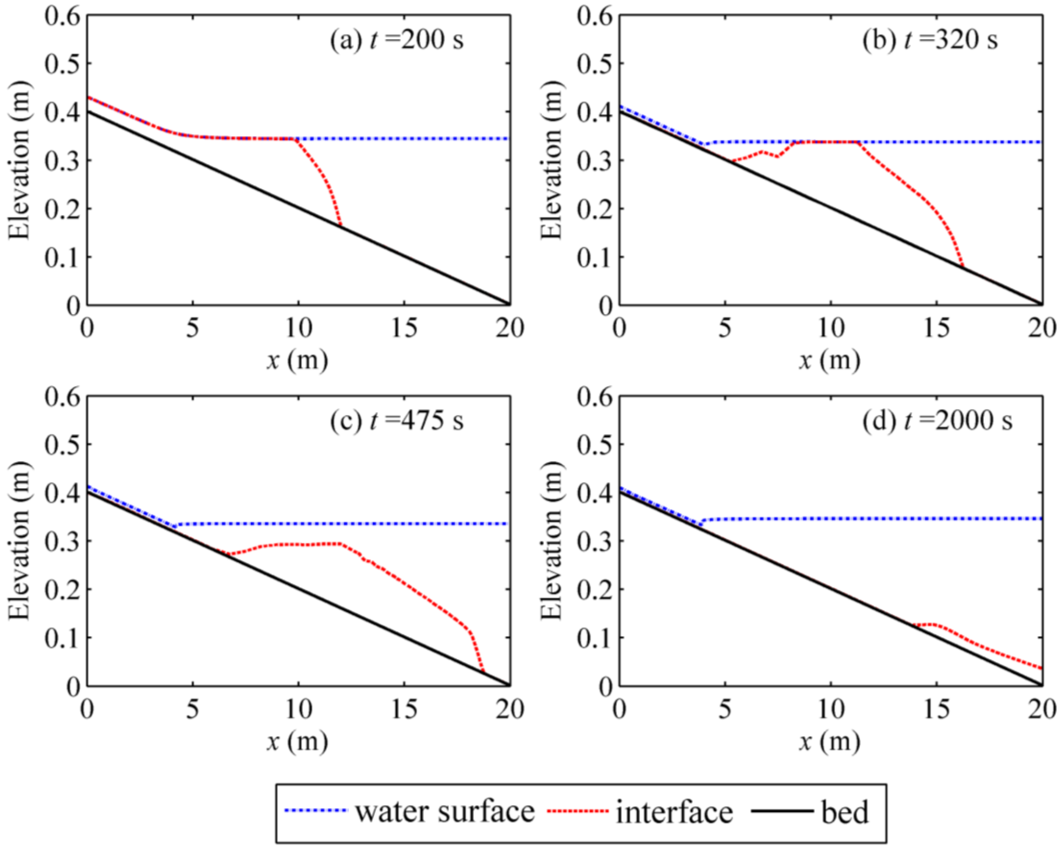

Figure 4.12 Turbidity current formation, propagation and recession (extended case from Series B - PP 4)

4.4. Implications and Discussions

It is interesting to evaluate the sediment flushing efficiency of a reservoir. In general, it is defined as the ratio of the bulk sediment volume V_{si} input from the inlet of the reservoir to that (V_{so}) carried away through the downstream boundary. Here V_{si} and V_{so} are calculated by

$$V_{si}(t) = \int (h_s u_s c_s)_{inlet} dt, \quad V_{so}(t) = \int (h_s u_s c_s)_{outlet} dt \qquad (4.1a, b)$$

It is noted that Lee and Yu (1997) focused on the turbidity currents without an evaluation of sediment flushing efficiency. In their experiments, there was no bottom outlet for sediment flushing at the downstream boundary (i.e., the end of the sloping section of the experimental flume). Here the experimental runs Series B - PP4 (Lee and Yu 1997) are extended to facilitate numerical investigation of the impacts of reservoir operation on sediment flushing. All the model parameters are kept the same as used in subsection just above (Fig. 4.11). It is assumed that at the downstream boundary, there is a 4 cm-high bottom outlet on the bed, which has a presumed maximum (unit-width) discharge of 42.55 cm^2/s. When the turbidity current reaches the downstream boundary, the bottom outlet is opened for sediment flushing, while the total outflow discharge (including clear-water flow and possibly turbidity current) remains the same as that in the experiments by Lee and Yu (1997). At the downstream boundary, before the arrival of the turbidity current, the depth and velocity of the clear-water flow layer are determined by the method of characteristics according to the total outflow discharge, as no downstream boundary condition is needed for the turbidity current. When the turbidity current has reached the bottom outlet, its respective discharge is equal to the maximum of the bottom outlet if the upper surface of the turbidity current is level with or higher than that of the bottom outlet; otherwise it is equal to a proportion of the maximum discharge of the bottom outlet calculated by the turbidity current thickness relative to the height of the bottom outlet. If the turbidity current is in the subcritical regime, its depth and velocity are determined by the method of characteristics in line with its respective outflow discharge (q_s); otherwise no downstream boundary condition is needed. Meanwhile the depth and velocity of the clear-water flow layer are determined by the method of characteristics based on its respective discharge $(= q_{out} - q_s)$.

Fig. 4.13 shows the sediment flushing efficiencies for the extended cases adapted from Series B - PP4 of Lee and Yu (1997). In general, sediment flushing commences as the turbidity current reaches the bottom outlet, and the flushing efficiency increases with time, which clearly requires sustained inputs of water and sediment from the inlet. If the clear-water outflow is cutoff from the initial state or after 4.33 min, the sediment flushing efficiency decreases. Generally, the sooner the clear-water outflow is cutoff, the less the sediment flushed out of the reservoir. Physically, the clear-water outflow accelerates the propagation of the turbidity current (Fig. 4.11c), which leads to an increase in the amount of sediment flushed out and therefore enhanced sediment flushing efficiency.

It follows that an appropriate clear-water outflow not only favors the turbidity current propagation (Fig. 4.11c), but also is conducive to improving sediment flushing efficiency (Fig. 4.13). This is undoubtedly of significance for developing optimal sediment management schemes for reservoirs on the Yellow River in China and others worldwide, which suffer from severe sedimentation problems. In a way, it adds to the current understanding of the effects of distinct reservoir operation schemes on sedimentation mitigation (Fan and Morris 1992a, b). Nevertheless, more detailed investigations are necessary to delimit quantitatively the impacts of reservoir operation schemes on sediment flushing by means of turbidity currents. This certainly holds for the Xiaolangdi Reservoir at the upstream end of the lower Yellow River, for which a case study is presented below. Particularly, it remains to be unraveled if an excessive clear-water outflow would spoil the turbidity currents that have already formed, as a result of Kelvin-Helmholtz instability.

Equally importantly, the impacts of the downstream boundary conditions on turbidity currents are in essence substantiated by the clear-water outflow through spillway and flood diversion, which is usually determined by the reservoir operation scheme. These significant impacts clearly tell that previous single layer-averaged models (e.g., Choi 1998; Bradford and Katopodes 1999a, b; Sequeiros et al. 2009b; Hu et al. 2012; Lai and

Wu 2013) are inadequate for applications in such cases because the clear-water flow is not modeled at all. The advantage (enhanced capability) of the present double layer-averaged model is evident.

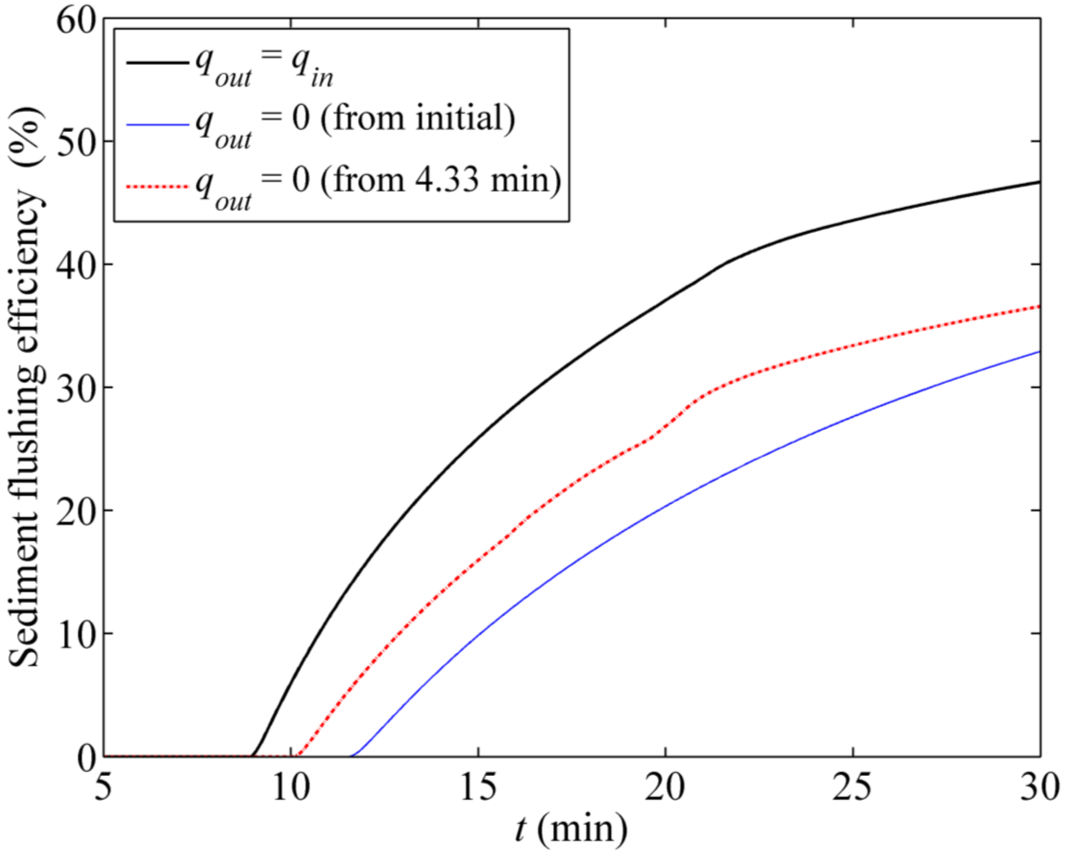

Figure 4.13 Sediment flushing efficiencies for extended cases

4.5. Conclusion

The present model is demonstrated to perform very well compared to a range of laboratory experimental turbidity current induced by lock-exchange and sustained inflow. It facilitates for the first time the whole-process of reservoir turbidity currents: formation, propagation and recession. Computational tests using the present model reveal that an appropriate clear-water outflow is favorable for the propagation of turbidity currents, and also conducive to enhancing sediment flushing efficiency. This is significant for optimal operations of reservoirs suffering from sedimentation problems. However, it remains to be unraveled if an excessive clear-water outflow would spoil the turbidity currents that have already formed, as a result of Kelvin-Helmholtz instability. Further investigations are conducted in Chapter 6 to delimit quantitatively the impacts of reservoir operation schemes on sediment flushing by means of turbidity currents.

CHAPTER 5 MODELLING RESERVOIR TURBIDITY CURRENTS AT PROTOTYPE-SCALE

5.1. Introduction

Flume experiments may be constrained by their relatively small spatial scales. Field observations of turbidity currents are relatively more abundant, as compared to those of dam-break flows. Ford et al. (1983) provide a detailed summary of observations of density currents in lakes and reservoirs. Nix et al. (1981) report turbidity current flows in DeGray Lake, and Hebbert et al. (1979) measured the inflow of low-temperature, high-salinity water into Wellington Reservoir in Western Australia. Alavian and Ostrowski (1992) made detailed velocity and temperature measurements in Watts Bar and Melton Hill reservoirs while routing a density current through the TVA reservoir system. In China, turbidity currents have been measured in many reservoirs built on heavily sediment-laden rivers, and even on rivers with low silt discharge. Specifically, in the Fengjiasha, Guanting and Liujiaxia Reservoirs, several turbidity currents were measured and documented, which provided valuable information to support the analysis of physical features of turbidity currents, including the plunging of muddy river flow at the head of the reservoir, the longitudinal and transverse variations in the density current as it flows towards the dam, the percentage of the sediment inflow that can be discharged by venting a density current through bottom sluices (Fan et al. 1959; Fan 1986). Especially, the ratio of sediment outflow to sediment inflow during a flood, termed the turbidity current venting efficiency, ranged from 18% to 36% in the Sanmenxia Reservoir with no backwater in the density current and no rising of pool water during flood periods. While in Fengjiashan Reservoir, the venting efficiency for flood peaks ranged from 23% to 65% derived from the 14 turbidity currents measured from 1976 to 1980. Most notably, the Yellow River of China, which is well known due to its extremely high sediment concentration, has long been suffering from serious sedimentation. The average annual sediment load of the Yellow River was approximated to reach as high as 1.6 billion tonnes in relation to the average annual runoff of about 43.2 billion m^3 (Qian and Wan 1983). Alternatively, the average volumetric sediment concentration exceeds 0.014. Consequently, a few hyperconcentrated sediment-laden flood events are usually formed in the annual flood season. Thus turbidity currents are frequently observed in the Yellow River, which simulate the awareness of reducing reservoir sedimentation by turbidity currents. The Xiaolangdi Reservoir is located in the lower Yellow River, about 130 km downstream of Sanmenxia Reservoir (Fig. 5.1). It controls 92.3% of the total basin area of the Yellow River and almost 100% of the sediment load. Severe sedimentation has occurred in the Xiaolangdi reservoir since its completion in 2001. Therefore a series of large field-scale water-sediment regulation experiments has been undertaken by the Yellow River Water Resources Commission (YRCC 2007) since 2002. Turbidity currents were formed in the Xiaolangdi Reservoir by plunging of the sediment-laden floods released from the Sanmenxia Reservoir at the upstream and believed to be the most important means for sediment flushing. A significant volume of hydrological data was collected, concerning the location of the front, average velocity and sediment concentration of the turbidity currents. The field experiments are certainly essential in support of not only practical sediment management, but also development and applications of analytical and computational models. However, most post-experimental analyses are built upon simple empirical relations, which cannot provide sufficient effective information to quantify the whole process of reservoir turbidity currents. In addition, there has been a lack of mathematical models available for the whole-process of the turbidity current, from formation and propagation. Notably, the work by Hu et al. (2012) modelled the propagation of turbidity currents while neglecting the impacts of the clear-water flow in the upper layer.

Here the present model was applied to a pilot study of prototype-scale turbidity currents in Xiaolangdi Reservoir, Yellow River in China. The present pilot study covers the whole process of the turbidity currents, from formation and propagation to recession, which is distinct from the work by Hu et al. (2012), which only modelled the propagation of turbidity currents while neglecting the impacts of the clear-water flow in the upper layer.

Figure 5.1 Sketch of the Yellow River

5.2. Turbidity currents in Xiaolangdi Reservoir

5.2.1. Case description

From 19th June to 13th July 2004, a water-sediment regulation experiment was conducted to make full use of the extra water storage to reduce sedimentation in the Yellow River. During the whole experiment, two separate turbidity current events were formed in the Xiaolangdi Reservoir by releasing sediment-laden inflows from the Sanmenxia and Wanjiazhai Reservoirs. Here the second event is revisited, as field data shows that the first turbidity current dissipated at about 6.5 km upstream of the Xiaolangdi dam (Li 2004; YRCC 2007) and thus is unsuitable for the whole-process modelling. This turbidity current occurred in the afternoon of 7th July, about 1 day after the end of the first event. Though indirectly, it was generated due to the water release from the Wanjiazhai Reservoir between the 2nd and 7th July. When this water flow entered the Sanmenxia Reservoir and thus increased its water storage, the flow discharge at Sanmenxia increased to approximately 5200 m^3/s, which induced a second sediment-laden flood and thus the second turbidity current in the Xiaolangdi Reservoir. There are 56 cross sections in the 130 km long main stream between Sanmenxia and Xiaolangdi dams. And the impacts of tributaries in between the two dams are tentatively neglected as they play a secondary role. The inflow discharge and its sediment concentration, which are actually released from the Sanmenxia Reservoir, are shown in Fig. 5.2 along with the outflow discharge through the Xiaolangdi dam. The inflow essentially relates to a hyperconcentrated flood modulated by the Sanmenxia Reservoir. The time $t =$ 0 h corresponds to 13:00 7th July, when the flow discharge at Sanmenxia reached its peak value. The computational time is 108 hours (from 13:00 7th July to 3:00 12th July). The total outflow discharge Q_{out}, including Q_s for the turbidity currents and Q_w for the clear water respectively, was kept constant and amounted to 2700 m^3/s. A total of 18 bottom outlets with the depth of 5 m are distributed at different locations under the dam. The maximum discharge for sediment flushing through the bottom outlets under the Xiaolangdi dam was 1500 m^3/s. At the upstream boundary, the discharge was specified, and the velocity and depth of the subaerial sediment-laden flow or clear-water flow were determined by the method of characteristics. The downstream boundary conditions are implemented in a similar manner to those in the subsection entitled Sediment flushing efficiency.

The initial bed topography is interpolated from 56 cross sections surveyed in May, 2004 (Fig. 5.3). The bed morphology resulting from the first event is not used because firstly there was no measurement of bed topography after its occurrence, and secondly the computed bed morphology from the first event is subject to uncertainty to an unknown extent. Initially there is no turbidity current on the river bed. The following parameters are specified with reference to the background of the Xiaolangdi Reservoir: $p =$ 0.4, $\rho_s =$ 2650 kg/m^3, and $d =$ 20 μm. In this subsection, the sediment transport is confined to a single size (i.e., the sediment size is kept at a single value, normally the median or mean sediment diameter, throughout the modeling), whilst the results of modelling using multiple sediment sizes are presented in a separate subsection below. Here the spatial step of 25 m is adopted. E_s is calculated through Eq. (2.43) following Hu et al. (2012). The Courant number C_r is set to be 0.4. The interface roughness n_i adopted is set to be 0.005 m$^{-1/3}$ s, following the calibrated value for the test cases related to the laboratory experiments in the previous section. The bed roughness n_b and the correction coefficient α need to be calibrated by fitting to the measured front location. It is found that bed roughness $n_b =$ 0.035 m$^{-1/3}$ s and correction coefficient $\alpha =$ 30 lead to satisfactory agreement with measured data. These calibrated parameters are appreciably different from those calibrated by Hu et al. (2012), which mostly can be ascribed to the limitation that the motion of the upper clear-water is not taken into account in the single layer-averaged model by Hu et al. (2012).

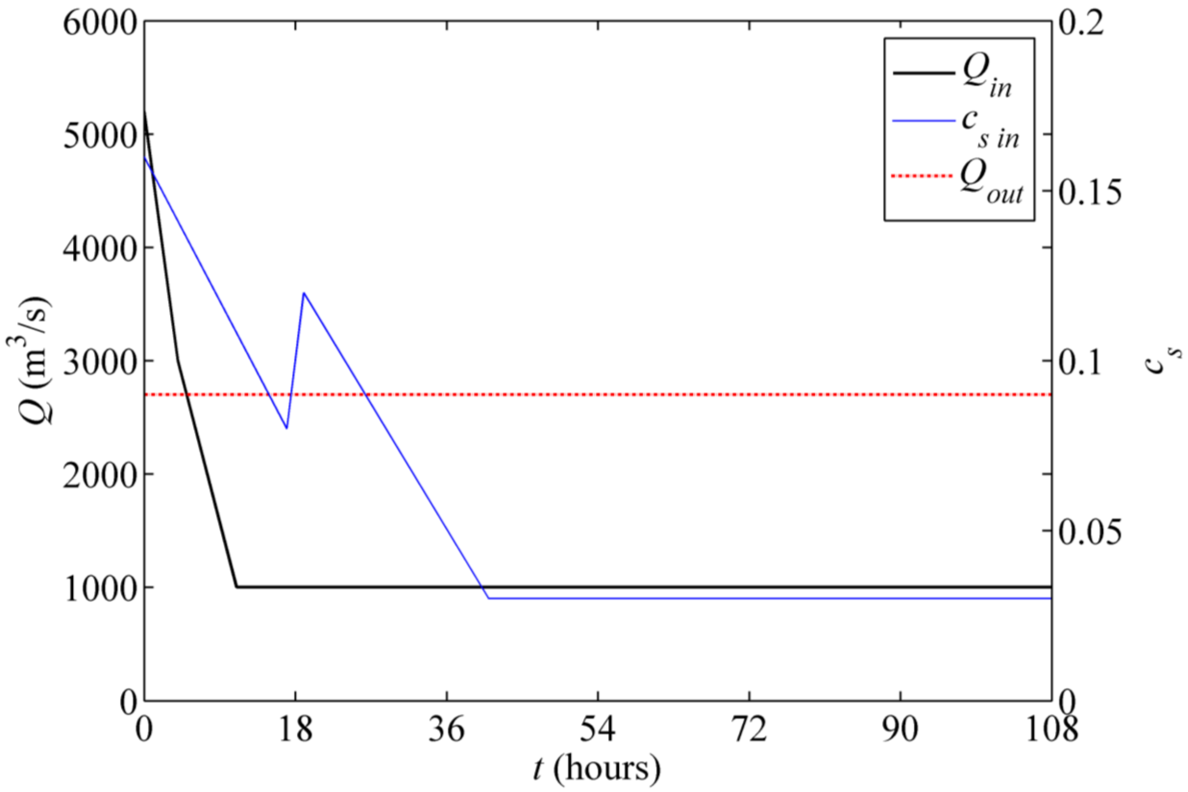

Figure 5.2 Time histories of Inflow discharge and sediment concentration along with outflow discharge in Xiaolandi Reservoir from 13:00 7th July to 3:00 12th July, 2004

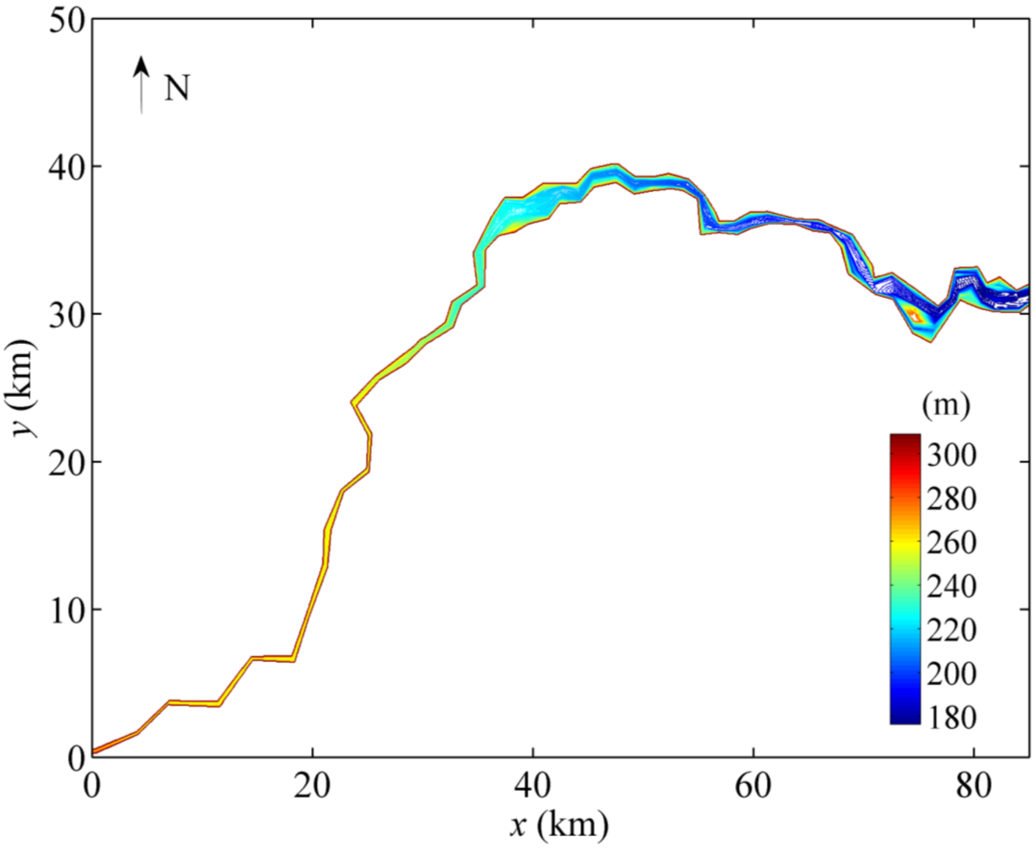

Figure 5.3 Contour of initial bed topography based on the survey in May 2004

5.2.2. Advance of turbidity currents

Information on current advance can facilitate timely operation of the bottom outlets under the dam so that sediment can be flushed out of the reservoir (Fan and Morris 1992a). If the bottom outlets are closed upon the arrival of the current, the turbidity currents may lead to severe sedimentation, or alternatively, if the bottom outlets are opened too early, stored water may be wasted. Shown in Fig. 5.4 is the computed front location of the sediment-laden flow (i.e., open-channel sediment-laden flow upstream the plunging point or the turbidity current downstream the plunging), measured along the course of the river. The measured data shown in Fig. 5.4 correspond to the arrival time (approximately t = 20 h) of the turbidity current at Xiaolangdi dam. In Fig. 5.4, the computed results with the fine grid (25 m) and a coarser grid (50 m) are included.

The difference between the two mesh resolutions is just marginally discernible, which demonstrates that the 25 m mesh resolution is sufficiently fine (i.e., mesh independence of the numerical solution is attained). From Fig. 5.4, the computed current propagation with n_b = 0.035 and α = 30 compares best with the measured data. The advance of the turbidity current front is mainly affected by the two parameters n_b and α. A faster advance is generally obtained with a larger correction coefficient α and a smaller bed roughness n_b. Physically, in relation to a larger correction coefficient α, bed sediment entrainment increases (Eq. 2.43), which leads to a higher sediment concentration and thus a larger driving force for the turbidity current. Therefore it propagates faster. The larger the bed resistance, as represented by n_b, the more energy the turbidity current dissipates and thus it propagates slower.

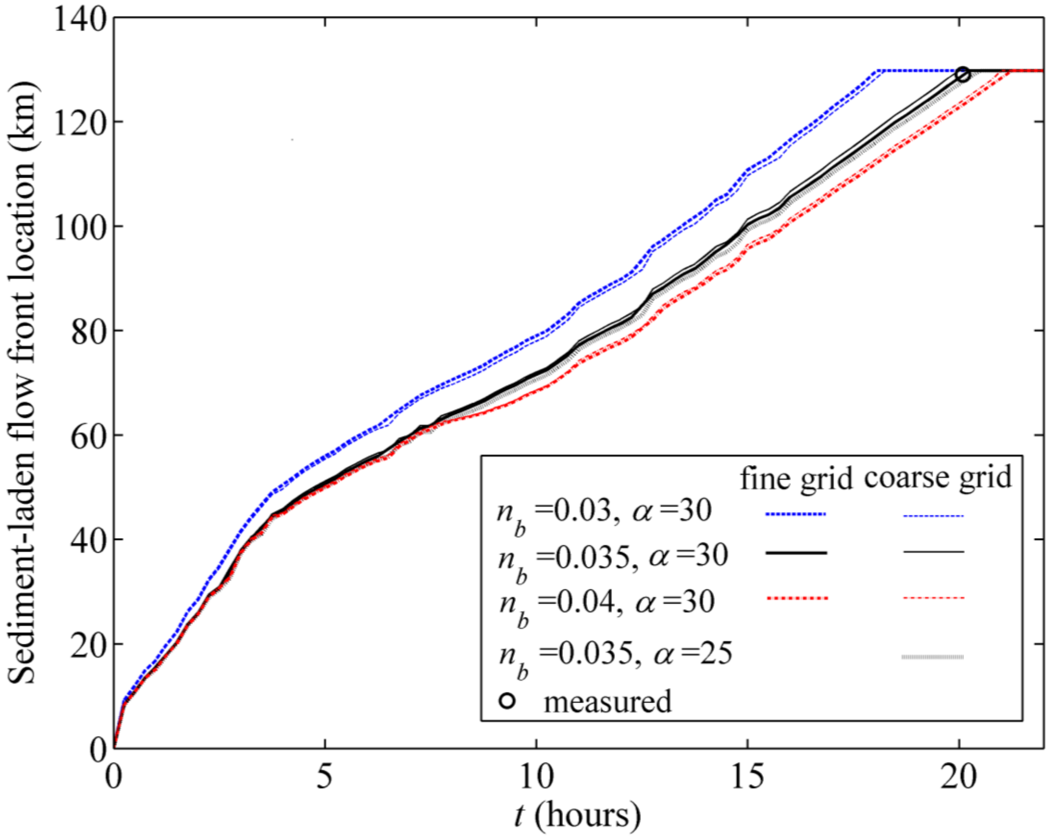

Figure 5.4 Computed front location of sediment-laden flow compared with measured data, measured along the course of the river

5.2.3. Whole process of turbidity currents

Figs. 5.5 and 5.6 demonstrate the formation, propagation and recession process of the turbidity current by virtue of the clear-water layer thickness h_w, turbidity current thickness h_s and sediment concentrations c_s respectively at four instants ($t =$ 4 h, 8 h, 20 h and 108 h). Also, Fig. 5.7 shows the whole process of the turbidity current by means of the water surface, interface and bed along the thalweg.

As illustrated in Figs. 5.5(a, b), 5.6(a) and 5.7(b), the flow at $t =$ 4 h is divided into two distinct sections, i.e., the open-channel sediment-laden flow upstream and the clear-water flow downstream. At about $t =$ 6.6 h, the open-channel sediment-laden flow advances to the cross section at approximately $x =$ 38 km, characterized by an abrupt increase in longitudinal bed slope (Fig. 5.3). Here the turbid water plunges into the clear water and begins to propagate as underflow, which marks the formation of turbidity current. Alternatively, the plunge point is located at roughly 56.5 km from the inlet along the course of the river, as shown in Fig. 5.7(c). From Fig. 5.6(b), a current with relatively high sediment concentration is formed and the highest sediment concentration occurs at current front.

After traveling about 13.5 hours since its formation, the turbidity current arrives at the Xiaolangdi dam [Fig. 5.4, Fig. 5.5(e, f), Fig. 5.6(c), Fig. 5.7(d)] and begins to be drained out through the bottom outlets; the largest turbidity current thickness occurs at the narrowest cross section (at $x =$ 65 km and $y =$ 35 km roughly); and the plunge point has hardly migrated downstream the plunging point at $x =$ 38 km [Fig. 5.7(d)]. As shown in Fig. 5.6(c), the sediment concentration starts to reduce gradually except in the section close to the inlet where sediment-laden flow continues to be released (Fig. 5.2).

After being vented through the bottom outlets for about 88 hours, the thickness of the turbidity current [Fig. 5.5(h)] and sediment concentration [Fig. 5.6(d)] have decreased considerably, along with a significant movement of the plunge point to the downstream [Fig. 5.7(f)]. In a way, this clearly reflects a state of recession of the turbidity current. It is rational to anticipate that the turbidity current would finally recede if clear water continues to be released at the Sanmenxia Reservoir and the turbidity current is allowed to flush through the bottom sluice gates under the Xiaolangdi dam.

These observations along with the reasonable agreement with observed data for the turbidity current advance suggest that the present model with properly specified parameters can properly resolve the whole process of turbidity currents in Xiaolangdi Reservoir.

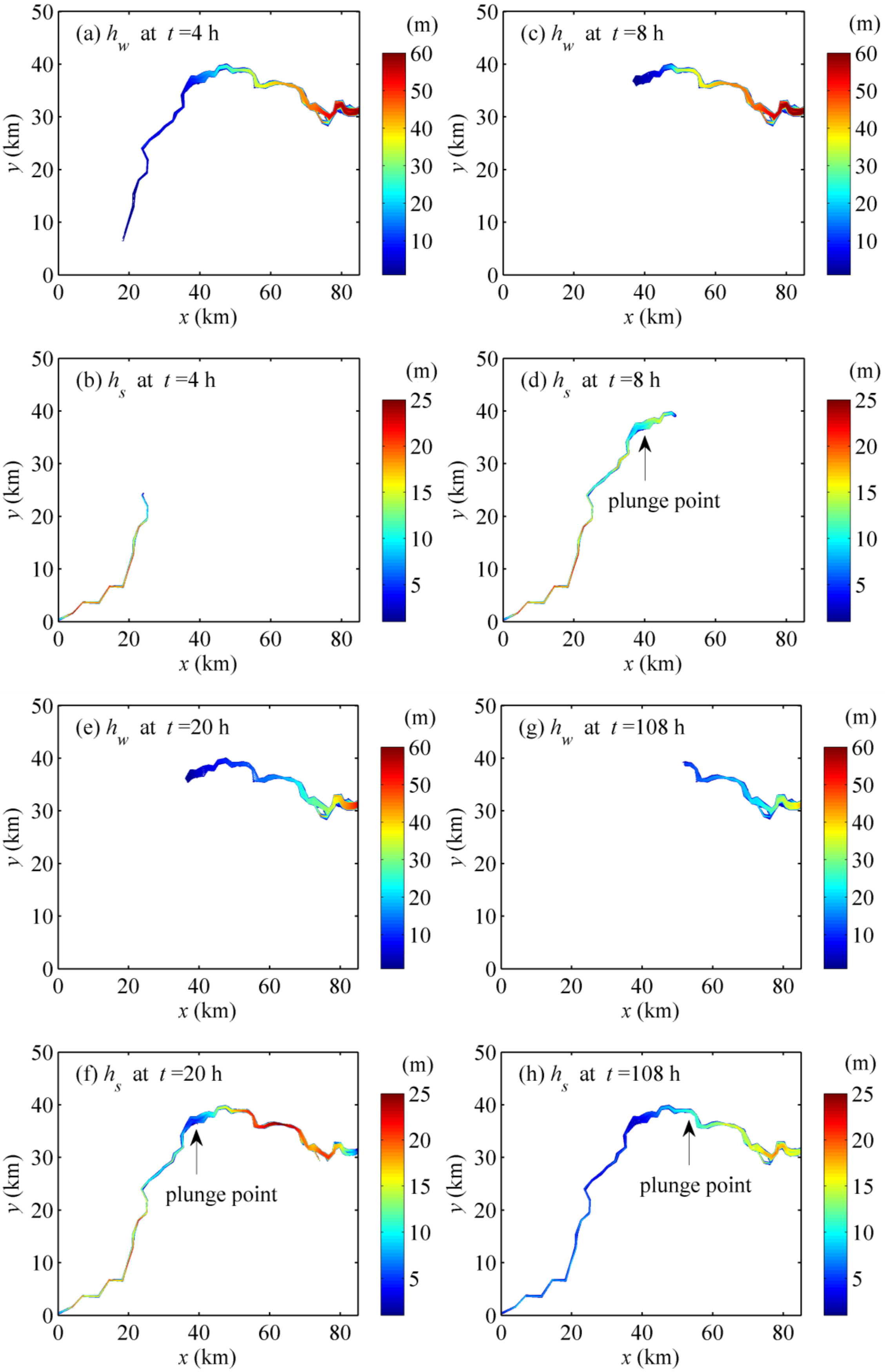

Figure 5.5 Distributions of turbidity current thickness and clear-water thickness in Xiaolandi Reservoir from 13:00 7th July to 3:00 12th July, 2004

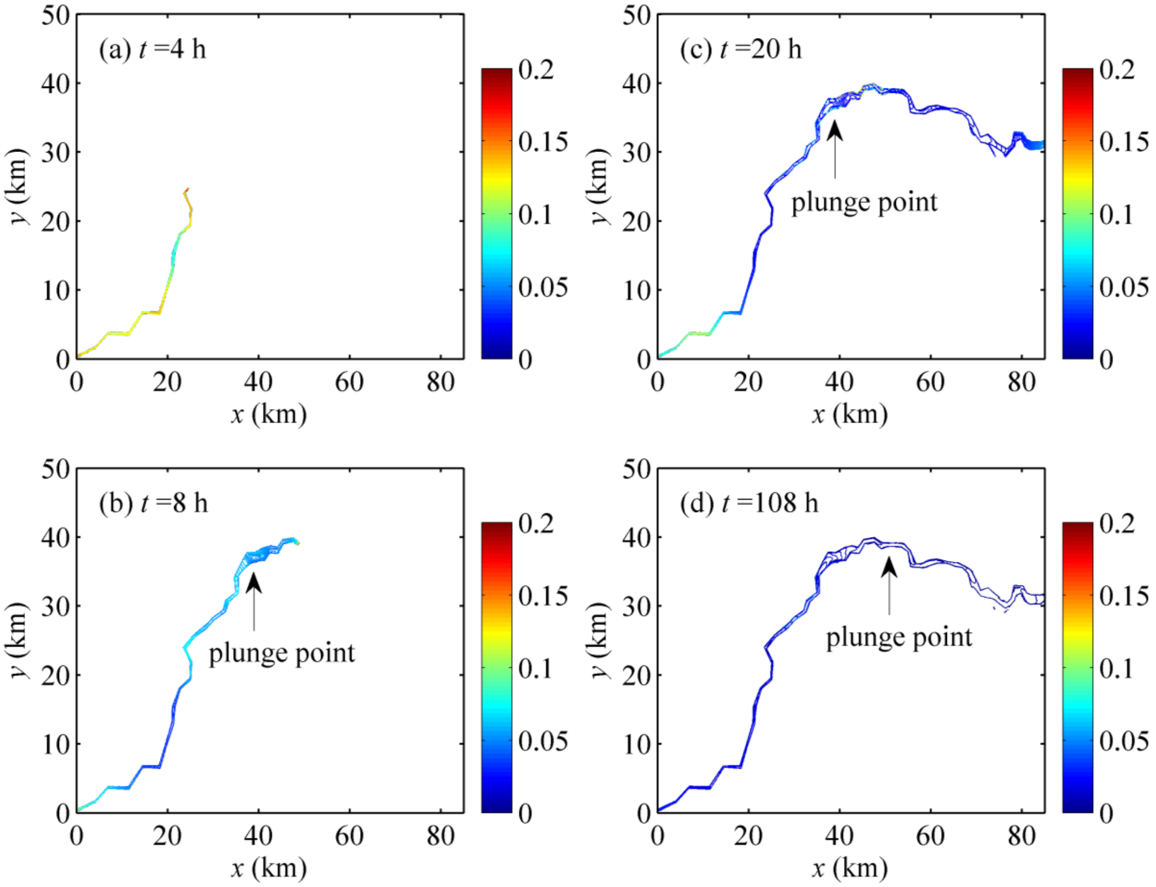

Figure 5.6 Distributions of volumetric sediment concentration in Xiaolandi Reservoir from 13:00 7th July to 3:00 12th July, 2004

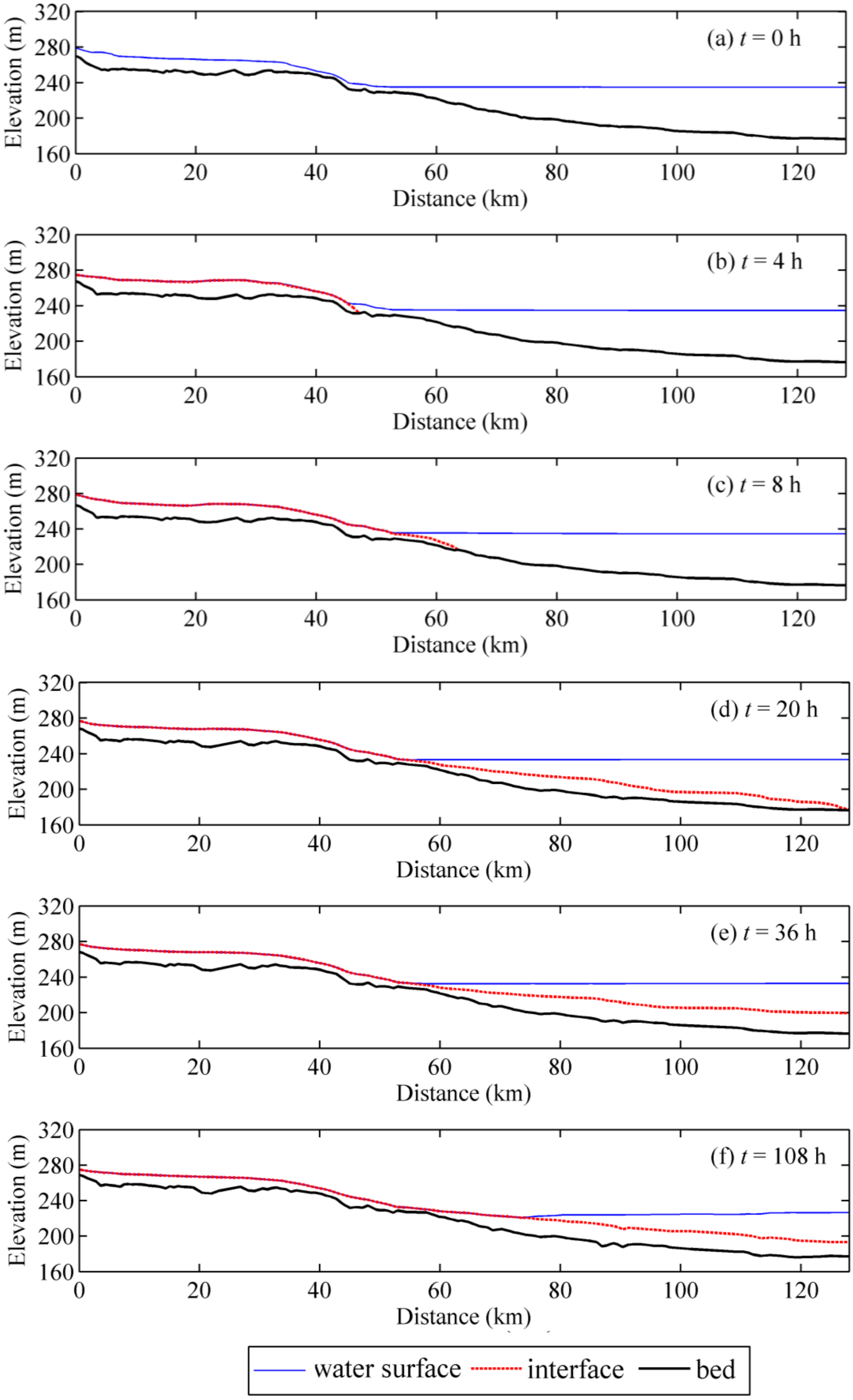

Figure 5.7 Water surface, interface and bed profiles along the thalweg in Xiaolandi Reservoir from 13:00 7th July to 3:00 12th July, 2004

5.2.4. Bed deformation and sediment mass conservation

Fig. 5.8 shows the bed scouring depth, defined as $z_b(x, y, 0) - z_b(x, y, t)$. The turbidity current appears to be erosive during the early stage, as indicated by the positive values of the bed scouring depth [Fig. 5.8(a, b)]. This is a clear manifestation of the occurrence of bed scour. Physically, this is attributable to the rather high discharge and sediment input released at the Sanmenxia Reservoir combined with the discharge through the Xiaolangdi dam (Fig. 5.2). As the inflow discharge and sediment concentration decrease gradually, bed aggradation occurs during the course of the turbidity current propagation towards the dam [Fig. 5.8(c, d)]. By t = 108 h, the whole domain of the Xiaolangdi reservoir sees bed aggradation, except locally narrow reaches [Fig. 5.8(d)].

For turbidity currents in an ocean environment, it has been suggested that self-accelerating mechanism exists (Parker et al. 1986). Specifically, the current entrains sediment from the bed, which leads to a higher sediment concentration, and thus a larger difference in its density from the ambient water. This essentially corresponds to an increase in the driving force for the current. Then, the current accelerates, and picks up more sediment from the bed, which further accelerates the current. Therefore, a self-reinforcing cycle is established. This mechanism cannot be precluded for the reservoir turbidity current in question, as the influence of the coefficient α in relation to bed sediment entrainment [Eq. (2. 43)] is marginally detectable (Fig. 5.4). Nevertheless, it is hard to isolate the effect of the self-accelerating mechanism from the control of the up- and downstream boundary conditions in the reservoir. This is also the case for the effect of sediment deposition out from the turbidity currents, which is opposite to the influence of the self-accelerating mechanism. Fortunately, all of those are properly incorporated in the present fully coupled model.

An evaluation of the global sediment mass conservation is certainly warranted as it can reveal not only the bulk aggradation or degradation in the Xiaolangdi Reservoir along with sediment flushing efficiency, but the performance of the present model. It accounts for the budget of the sediment that enters the Xiaolangdi Reservoir from the release at the Sanmenxia Reservoir, is flushed out at the Xiaolangdi Reservoir by means of turbidity current, and also the sediment content within the flow. For this purpose, the volume $V_{sc}(t)$ of the sediment contained within the flow is defined by

$$V_{sc}(t) = \int\int h_s c_s dxdy \tag{5.1}$$

and the volume of the sediment due to bed erosion or deposition by $V_{sb}(t)$,

$$V_{sb}(t) = (1-p)\int\int \left[z_b(x,y,0) - z_b(x,y,t)\right]dxdy \tag{5.2}$$

The volume $V_{si}(t)$ of the sediment input from the upstream, and that $V_{so}(t)$ carried away through the bottom outlets, respectively, are

$$V_{si}(t) = \int\int (h_s u_s c_s)_{inlet} dydt, \quad V_{so}(t) = \int\int (h_s u_s c_s)_{outlet} dydt \tag{5.3a, b}$$

The bulk mass conservation of the sediment phase provides that the residual sediment volume

$$R_s \equiv V_{si}(t) - V_{so}(t) + V_{sb}(t) - V_{sc}(t) + V_{sc}(0) = 0 \tag{5.4}$$

In a perfect case, R_s should vanish, but normally it does not due to numerical errors. It is an important indicator of the performance of a numerical model in the sense of mass conservation. A positive value of $V_{sb}(t)$ means bulk degradation and the reverse demonstrates a bulk aggradation.

The volumes of sediment input from the upstream boundary (V_{si}), carried away through the bottom outlets (V_{so}), scoured from or deposited at the bed (V_{sb}), and contained within the flow (V_{sc}) along with their residuals (R_s) are illustrated in Fig. 5.9. It is demonstrated that by $t = 18$ h, there is no sediment flushed out from the reservoir ($V_{so} = 0$) as the turbidity current has not yet arrived at the bottom outlets. Before $t = 18$ h, the sediment volume contained within the flow (V_{sc}) exceeds the sediment input from upstream (V_{si}), thus the sediment scoured from bed is considerable ($V_{sb} > 0$), echoing the occurrence of bed scour as illustrated in Fig. 5.8(a, b). Along with the gradual reduction of the sediment input rate, both V_{sc} and V_{sb} decrease, and especially V_{sb} reduces to be negative, which means a shift from bulk degradation to bulk aggradation in the Xiaolangdi Reservoir. At approximately $t = 20.5$ h, due to the arrival of the turbidity current, the bottom sluicing gates under Xiaolangdi dam are opened for sediment flushing, inducing sediment output. After $t = 60$ h, the sediment input rate becomes stable, V_{so} increases gradually, V_{sc} is little changed, while V_{sb} decreases further, characterizing continuous bulk aggradation. At $t = 108$ h, about 1.173×10^7 (m^3) of sediment has been flushed downstream by means of the turbidity current, while the bulk aggradation in the Xiaolangdi Reservoir amounts to 1.196×10^7 (m^3), which are respectively equivalent to 37.47% and 38.2% of the sediment input from the Sanmenxia Reservoir. The sediment flushing efficiency (37.47%) of this particular turbidity current is consistent with the empirical range (18% - 36%) for the Sanmenxia Reservoir (Fan and Morris 1992b) immediately upstream the Xiaolangdi Reservoir. Yet this sediment flushing efficiency is considerably lower than others that can be over 60% (Fan and Morris 1992b). Echoing the observations (Figs. 4.11, 4.12 and 4.13) derived from the computational tests in relation to the laboratory experiments by Lee and Yu (1997), further investigations are necessary to optimize the reservoir operation scheme in line with differing inflow and sediment inputs so that the sediment flushing efficiency can be maximized.

There has been no estimate of the bulk aggradation during the period of this particular turbidity current to confirm the present modelling in this regard. Yet according to YRCC (2007), the bulk aggradation was about 6.0×10^7 (m^3) over two months, during which two turbidity current events occurred, and the first (from 18:00 5th to 19:00 6th July 2004) did not manage to reach the Xiaolangdi dam and therefore the sediment released from the Sanmenxia Reservoir entirely deposited on the bed. Given this information and also that tributary contributions have been neglected in the present modelling, the amount of bulk aggradation (1.196×10^7 m^3) in connection with the particular turbidity current studied herewith is reasonable. Equally notably, the bulk residual (R_s) of sediment in the Xiaolangdi Reservoir is very small (Fig. 5.9), compared to the sediment volumes scoured from or deposited at the bed, input from the upstream or output through the bottom outlets. More specifically, the ratio of the residual R_s to V_{si} is only 1.61%. This further confirms the excellent performance of the present model to resolve reservoir turbidity currents.

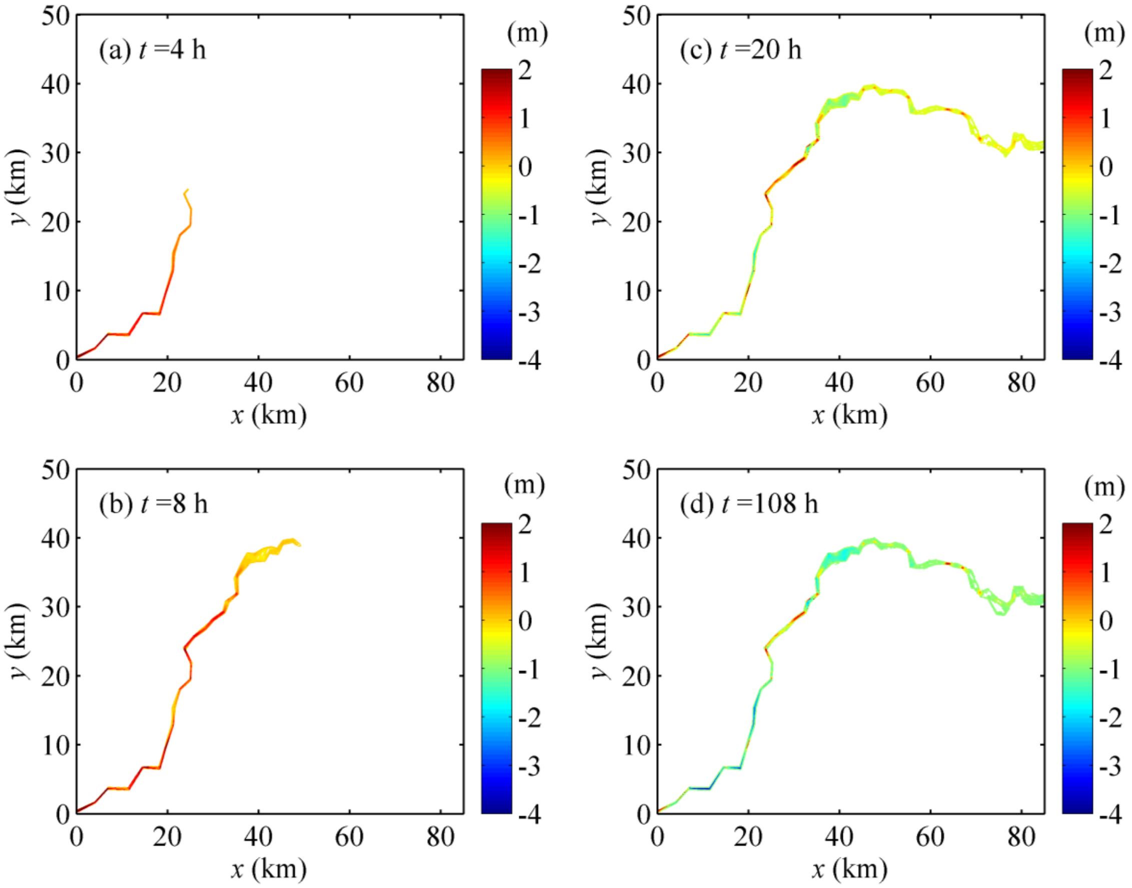

Figure 5.8 Distributions of bed scouring depth induced by turbidity current in Xiaolangdi Reservoir from 13:00 7th July to 3:00 12th July, 2004

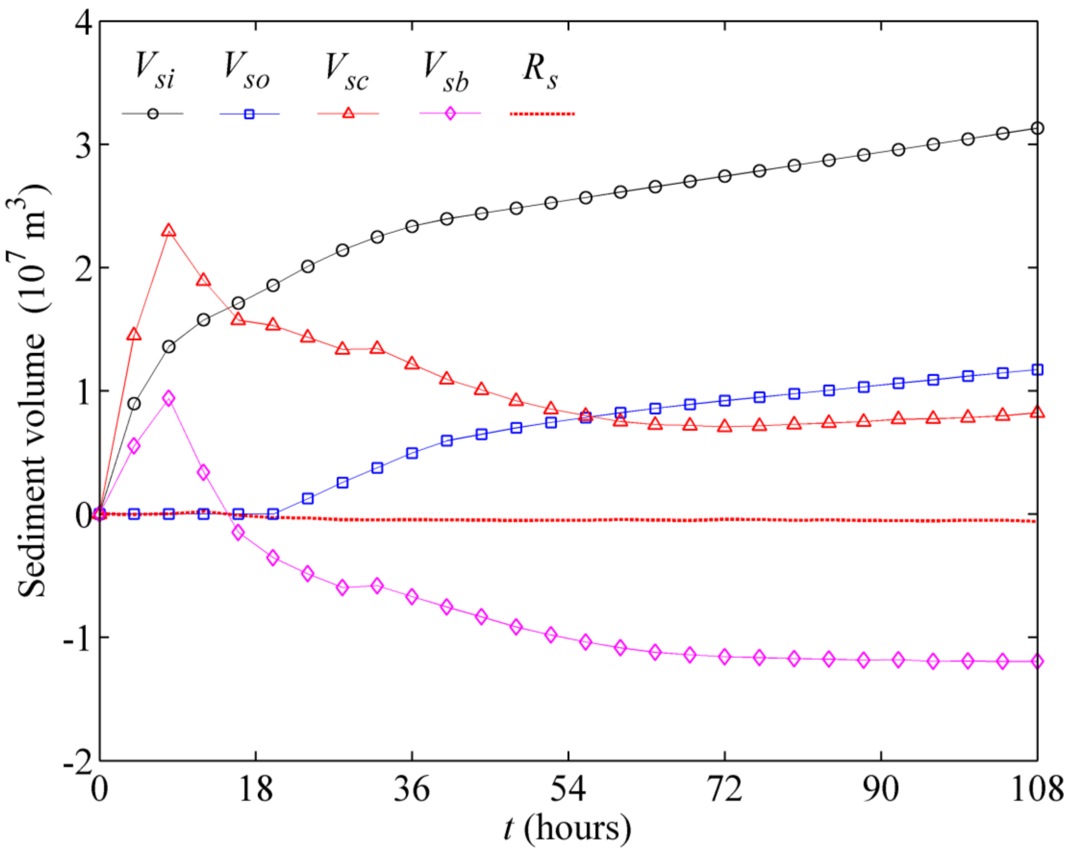

Figure 5.9 Sediment volumes input from the upstream, output through bottom outlets, scoured from or deposited at the bed, contained within the flow and their residuals in Xiaolandi Reservoir from 13:00 7th July to 3:00 12th July, 2004

5.3. Multi grain sizes versus single size of sediments

So far, the present double layer-averaged model is run by using a single size of sediments (i.e., the sediment size is kept at a single value, normally the median or mean sediment diameter, throughout the modeling). Whilst in practice sediments in debris flows may be heterogeneous. In this regard, the present model is evaluated as applied to modelling reservoir turbidity currents in Xiaolangdi Reservoir with multi grain sizes of sediments. The initial bed topography, the inflow discharge and its total sediment concentration released from Sanmenxia Reservoir along with the outflow discharge through Xiaolangdi dam are the same as in the case using a single size of sediments, as addressed above (Section 5.1). The fed material (sediment inflow) and bed material are composed of graded sediments with five size fraction, ranging from 9.12 μm to 55.9 μm. The detailed material composition is given in Table 5.1.

Table 5.1 Fed and bed material composition

d_k (μm)	9.12	12.2	21.2	38.7	55.9
%	10.0	22.0	43.0	20.0	5.0

Fig.5.10 shows the computed front location of the sediment-laden flow, which is also measured along the course of the river. The measured arrival time of the turbidity current at Xiaolangdi dam and the computed results using a single size of sediments are also included. From Fig. 5.10, the computed current propagation with n_b = 0.0375 and α = 20 compares best with the measured data. Similar to the cases with single-sized sediment transport, a faster advance is generally obtained with a larger correction coefficient α and a smaller bed roughness n_b. The turbidity current with multi grain sizes of sediments advances slower initially ($t < 8$ h), however then moves faster after the formation of turbidity currents, as compared to that using a single size of sediments.

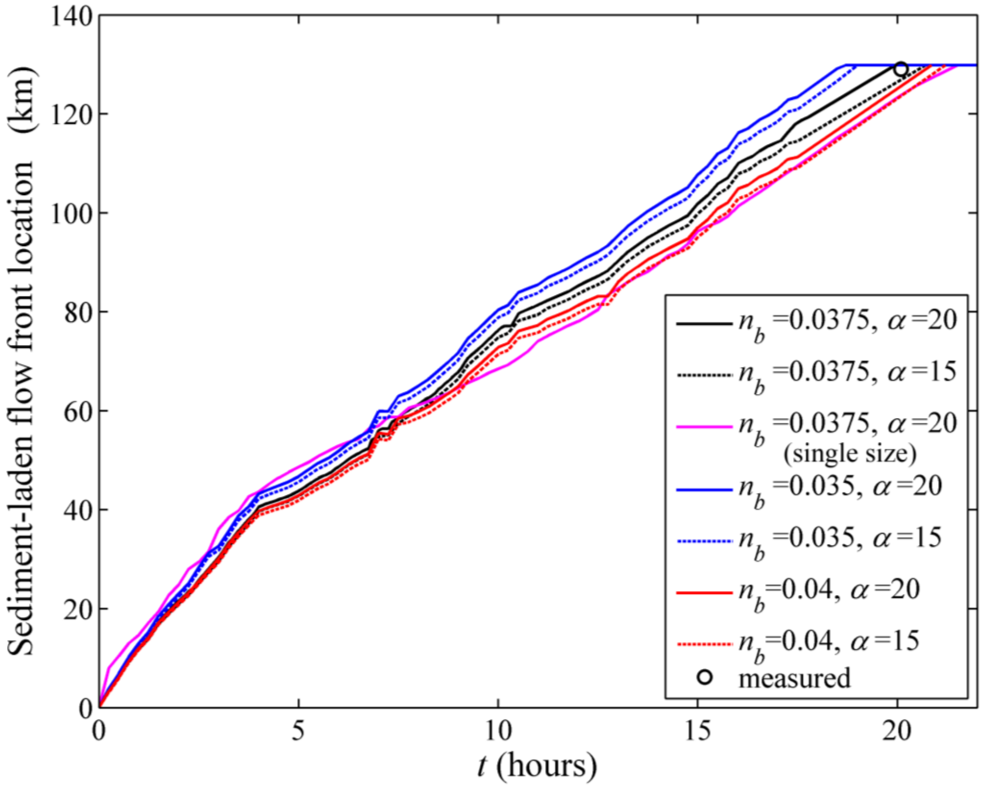

Figure 5.10 Computed sediment-laden flow location with measured data using multi grain sizes: measured through the course of the river

Figs. 5.11 and 5.12 illustrate the formation, propagation and recession process of the turbidity current using multi grain sizes of sediments as represented by the clear-water layer thickness h_w, turbidity current thickness h_s and total sediment concentration C_s respectively at four typical instants (t = 4 h, 8 h, 19.7 h and 108 h). Also, Fig. 5.13 shows the whole process of the turbidity current by virtue of the water surface, interface and bed along the thalweg. And the computed results using a single size of sediments is also incorporated. Similarly, the flow is divided into two distinct sections initially, i.e., the open-channel sediment-laden flow upstream and the clear-water flow downstream [Figs. 5.11a, b, 5.12a, 5.13b]. At approximately t = 6.75 h, the turbidity current is formed due to the plunging of turbid water into clear water. Seen from Fig. 5.12(b), at this stage, the sediment concentration of turbidity current is shown to be relatively high and the highest value occurs at the current front. After traveling about 13.0 hours since its formation, the turbidity current reaches the Xiaolangdi dam [Fig. 5.10, Fig. 5.11(e, f), Fig. 5.12(c), Fig. 5.13(d)] and begins to be flushed out through the bottom outlets; with the plunge point stabilizing at $x = 40$ km [Fig. 5.13(d)]. Likewise, after being vented through the bottom outlets for nearly 88 hours, the thickness of the turbidity current [Fig. 5.11(h)] and sediment concentration [Fig. 5.12(d)] have also decreased considerably, along with a significant movement of the plunge point to the downstream [Fig. 5.13(f)]. Comparatively, the plunge point in case using multi grain sizes of sediments migrates downstream less than that in case with single-sized sediment transport (shown in Fig. 5.14), which leads one to speculate that graded sediments may be conducive to the stabilization of plunge point.

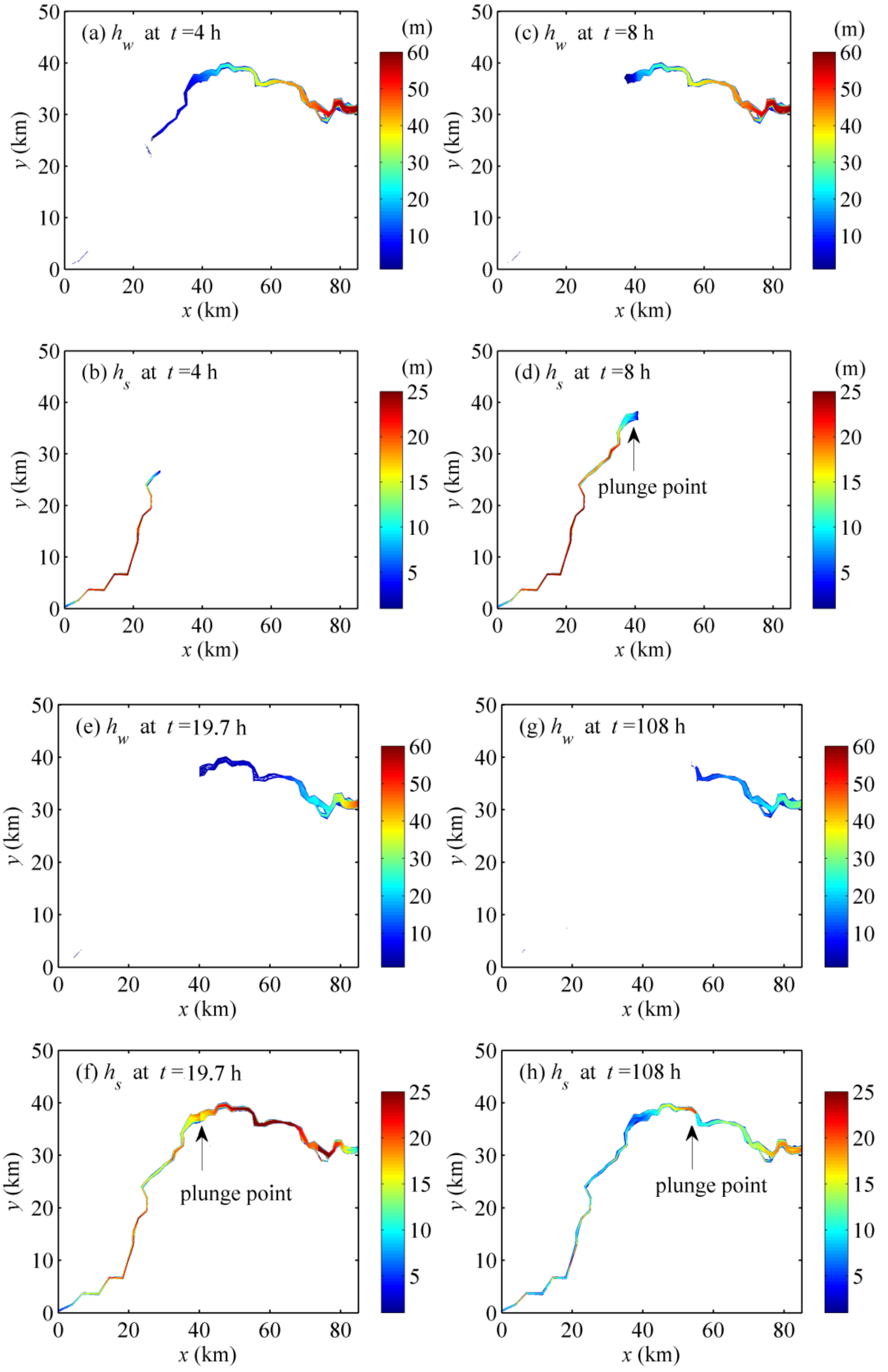

Figure 5.11 Distributions of turbidity current thickness and clear water thickness in Xiaolandi Reservoir from 13:00 7th July to 3:00 12th July, 2004

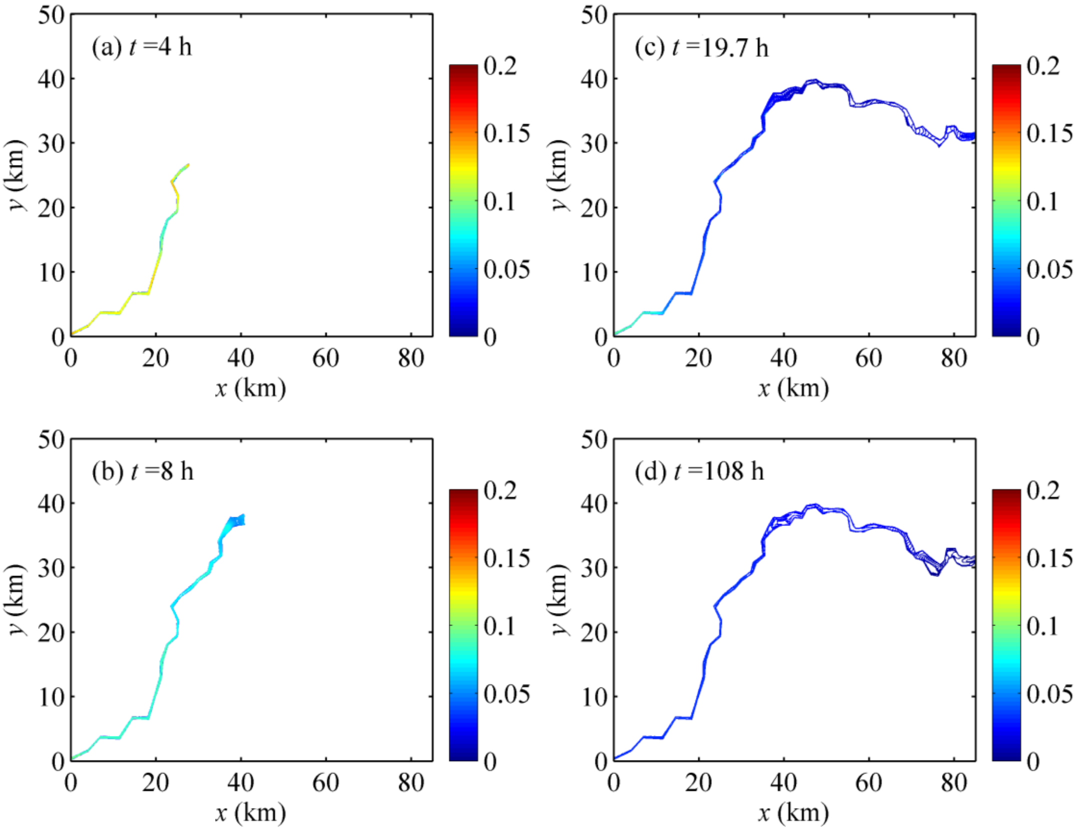

Figure 5.12 Distributions of volumetric sediment concentration in Xiaolandi Reservoir from 13:00 7th July to 3:00 12th July, 2004

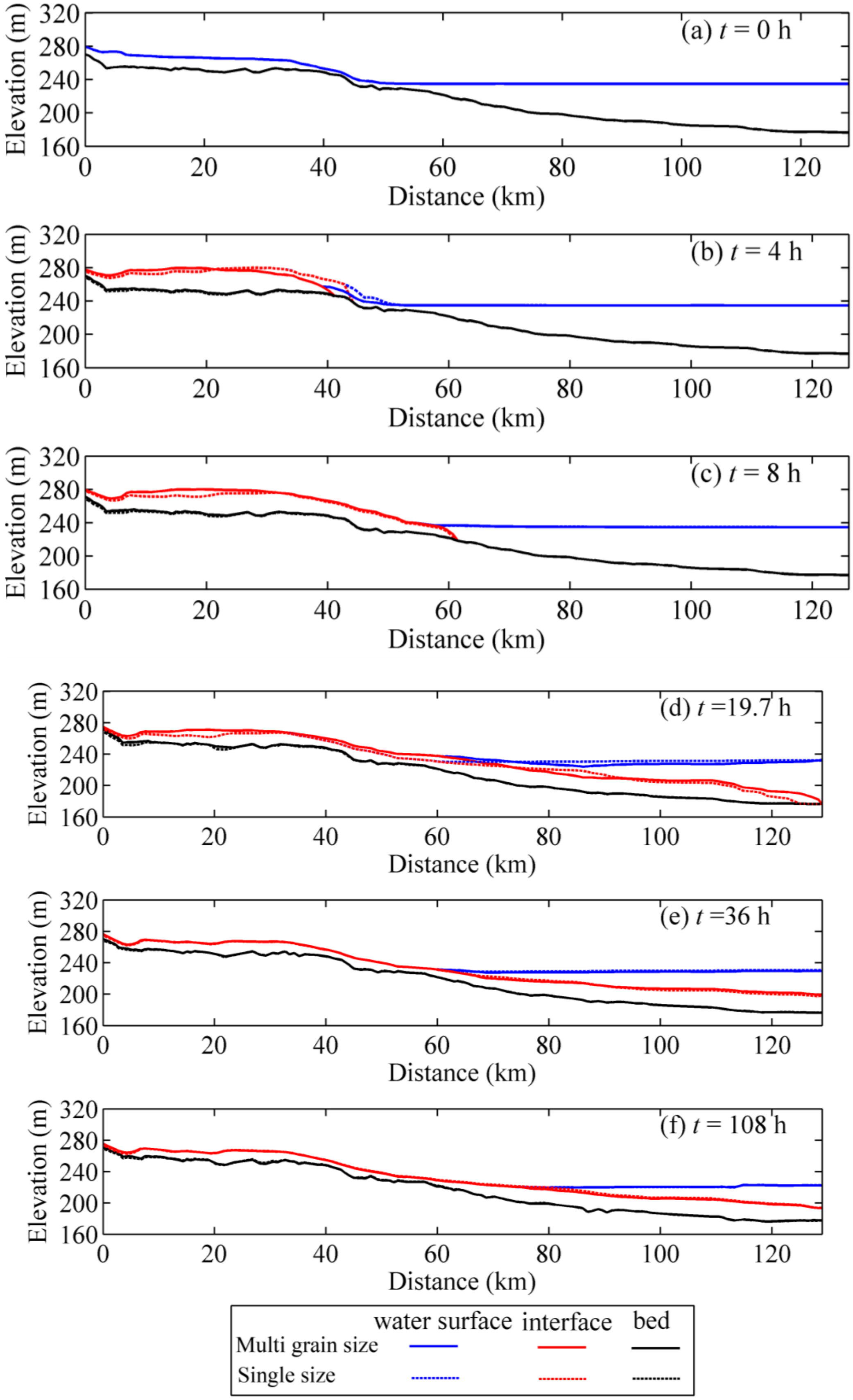

Figure 5.13 Water surface, interface and bed along the thalweg in Xiaolandi Reservoir from 13:00 7th July to 3:00 12th July, 2004

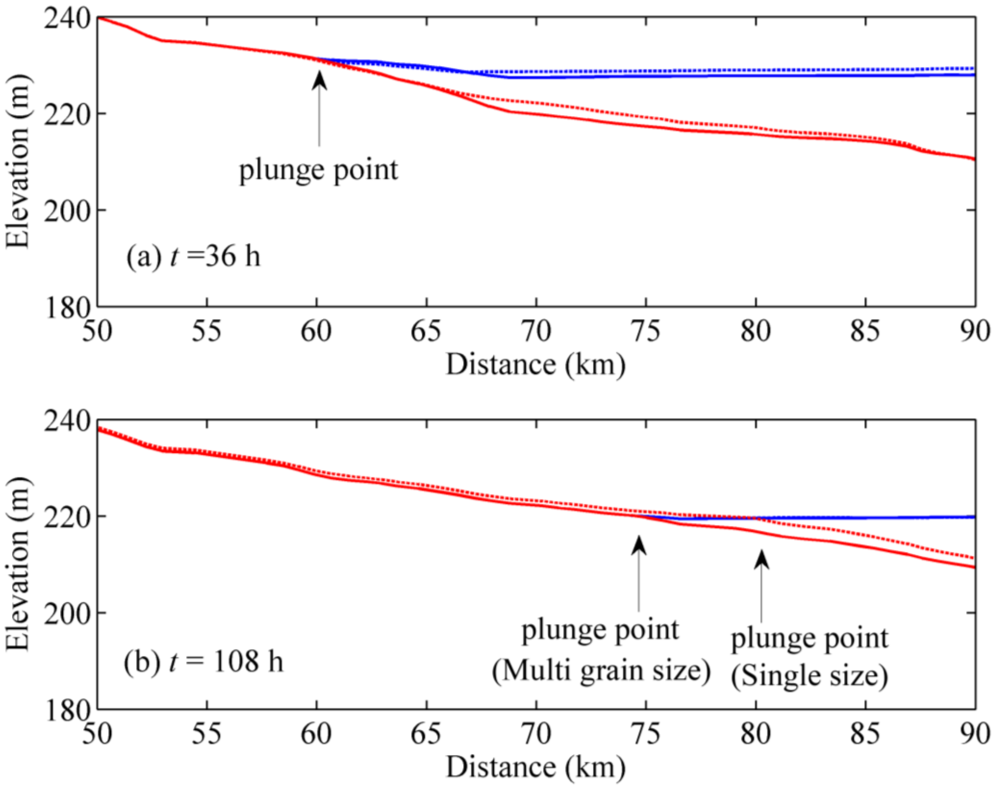

Figure 5.14 Movements of plunge point at specific instatns

Fig. 5.15 demonstrates the variations of the bed scouring depth. Initially, the turbidity current with multi grain sizes of sediments is also shown to be erosive [Fig. 5.15(a, b)], and then turns to be depositional as the time is going on [Fig. 5.15(c, d)]. By t = 108 h, the whole domain of the Xiaolangdi reservoir features bed aggradation, except locally narrow reaches [Fig. 5.15(d)]. Qualitatively, the reservoir sedimentation due to turbidity current with multi grain sizes of sediments is less serious than that in case using a single size of sediments. Figs. 5.16 and 5.17 illustrate the distributions of characteristic size D_{50}, D_{90} (the particle sizes at which 50% and 90% of the sediments are finer respectively). Seen from Figs. 5.16 and 5.17, the bed coarsening trend is demonstrated before the turbidity current arrives at the dam mainly due to the bed erosion caused by the turbidity current. After the arrival of the turbidity current, the bed is gradually fining due to the bed aggradation induced by the turbidity current.

Fig. 5.18 illustrates the volumes of sediment input from the upstream boundary (V_{si}), carried away through the bottom outlets (V_{so}), scoured from or deposited at the bed (V_{sb}), and contained within the flow (V_{sc}) along with their residuals (R_s). Similarly, it features the initial growth of V_{sc} due to mass gain from the bed erosion ($V_{sb} > 0$) before $t =$ 20.0 h, then the decrease of V_{sc} along with a shift from bulk degradation to bulk aggradation, and finally the gradual stabilization of V_{sc} along with the further increasing of V_{so} as well as the decrease of V_{sb}. Overall these results are qualitatively similar to those using a single size of sediments. Finally, about 1.299×10^7 (m^3) of sediment has been flushed out of the reservoir, while the bulk aggradation in the Xiaolangdi Reservoir amounts to 1.067×10^7 (m^3), which are respectively equivalent to 41.51% and 34.07% of the sediment input from the Sanmenxia Reservoir. As compared to the counterparts of the case using a single size of sediments, the sediment flushing efficiency has increased slightly and the bulk aggradation decreases accordingly, echoing the qualitative observation through Fig. 5.15(d). Fig. 5.19 illustrates the size-specific sediment flushing volume through the bottom outlets. Seen from Fig. 5.19, the flushing volume of grain size $D = 21.1$ μm and $D = 55.9$ μm feature respectively the maximum and minimum values, and those of other sizes lie in between them. In general, the sequence of the flushing volume of different grain size is consistent with that of the material composition.

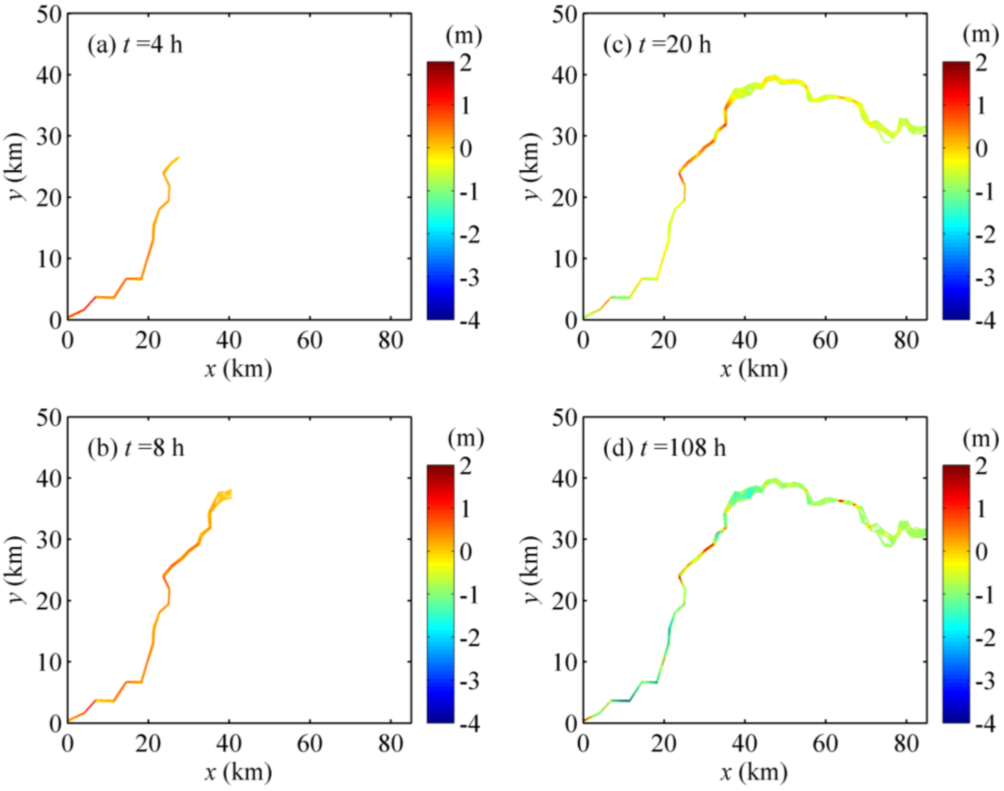

Figure 5.15 Distributions of bed scouring depth induced by turbidity current in Xiaolandi Reservoir from 13:00 7th July to 3:00 12th July, 2004

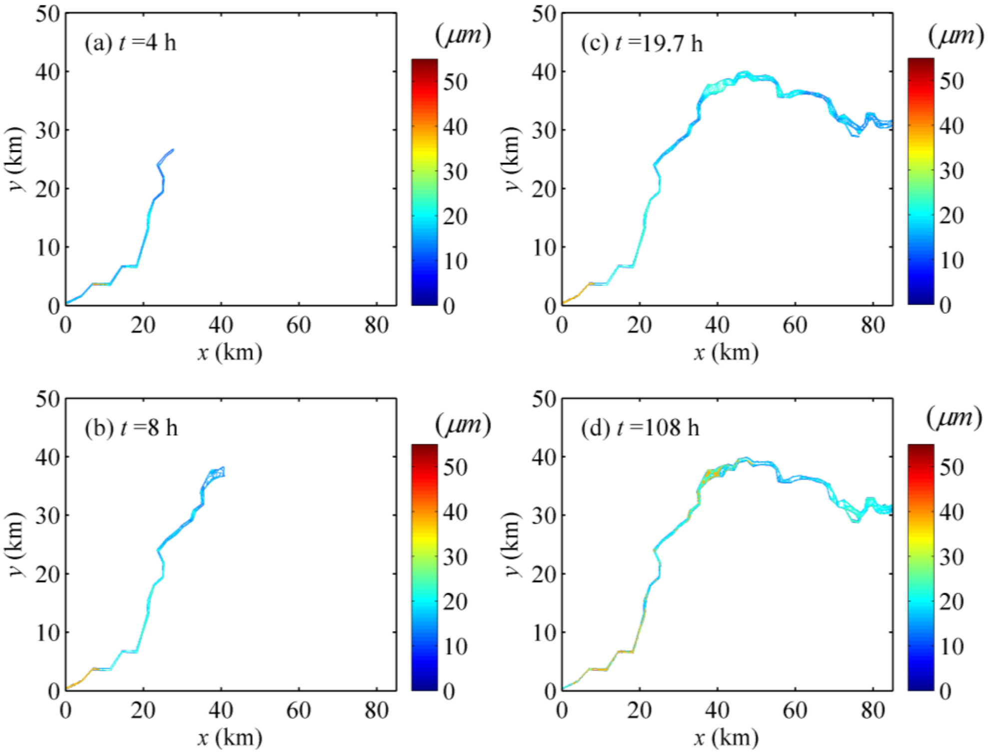

Figure 5.16 Distributions of D_{50} of the bed sediments in Xiaolandi Reservoir from 13:00 7th July to 3:00 12th July, 2004

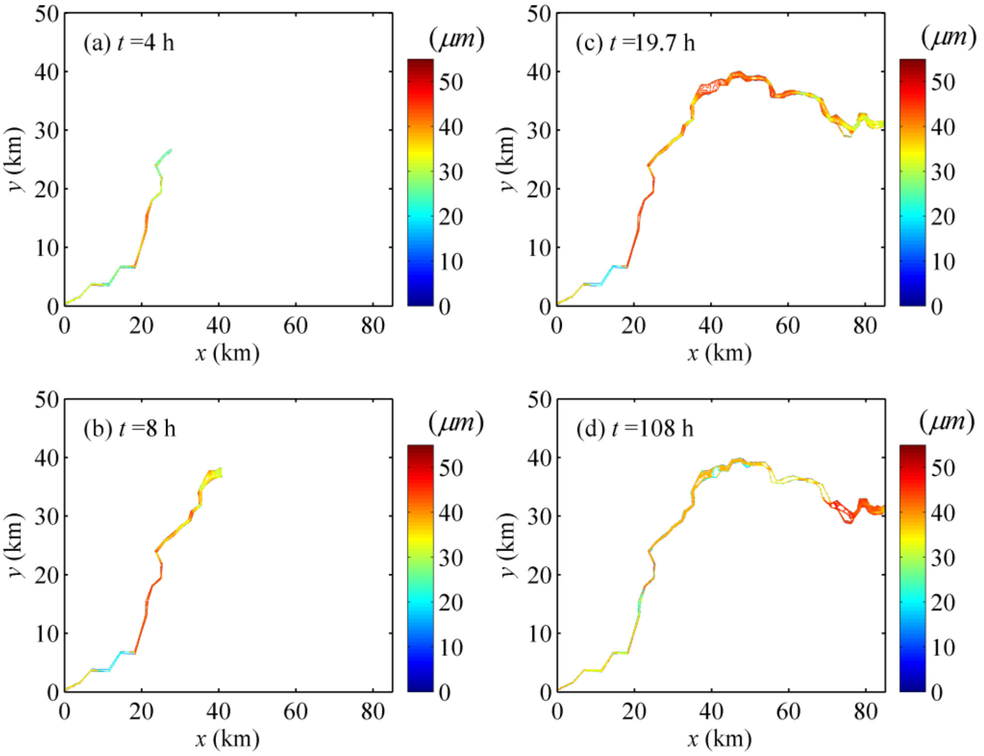

Figure 5.17 Distributions of D_{90} of the bed sediments in Xiaolandi Reservoir from 13:00 7th July to 3:00 12th July, 2004

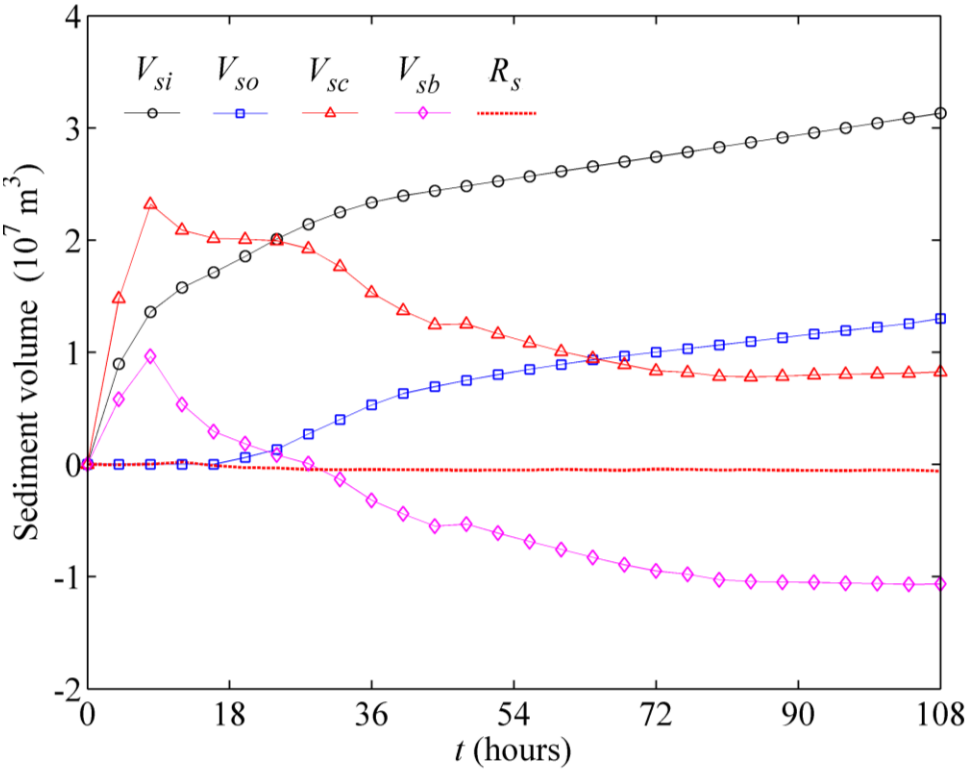

Figure 5.18 Sediment volumes input from the upstream, output through bottom outlets, scoured from or deposited at the bed, contained within the flow and their residuals in Xiaolandi Reservoir from 13:00 7th July to 3:00 12th July, 2004

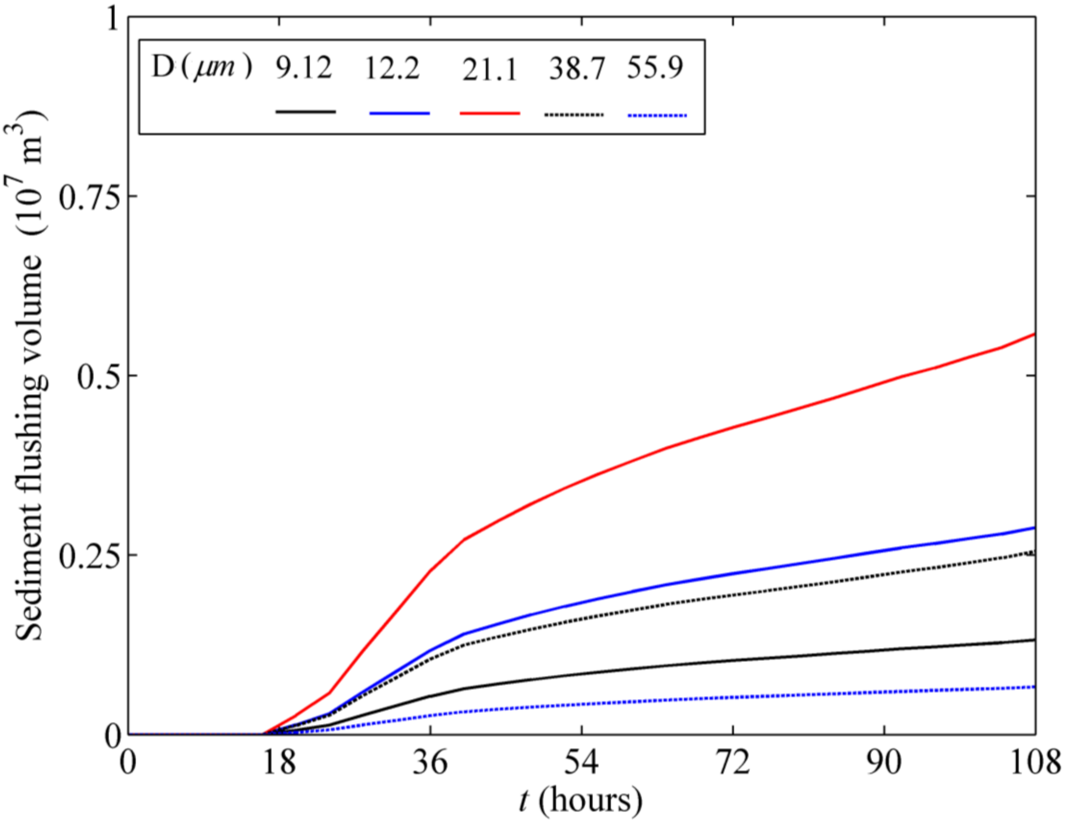

Figure 5.19 Size-specific sediment flushing volume through the bottom outlets in Xiaolandi Dam from 13:00 7th July to 3:00 12th July, 2004

5.4. Conclusion

The prototype-scale turbidity current in the Xiaolangdi Reservoir, Yellow River in China is reproduced by the present model. The model successfully resolves the whole process from formation and propagation to recession. And the advance of the current is captured by the model fairly well when compared to the measured data. It is also demonstrated that turbidity current with multi grain sizes of sediments features faster propagation, more stable plunge point and less sedimentation, as compared to that using a single size of sediments. The present work facilitates a viable and promising framework for whole-process modelling of turbidity currents, in support of reservoir sediment management.

CHAPTER 6 HYPERBOLICITY ANALYSIS AND ITS IMPLICATIONS FOR RESERVOIR OPERATION

6.1. Introduction

In the present study, the governing equations for each layer are cast into a non-homogeneous hyperbolic system, whilst the inter-layer interactions are represented as source terms as they are negligible compared to inertia and gravitation. The two reduced-order hyperbolic systems of the governing equations for the two layers are solved separately and simultaneously. The present model solved by the proposed numerical solution has demonstrated rather good performance when tested against a spectrum of experimental cases including dam-break flows and turbidity currents (Li et al. 2013; Cao et al. 2015). Although the proposed numerical solution is demonstrated to be effective and satisfactorily accurate post priori, it is essential to carry out hyperbolicity analysis systematically by analyzing and comparing the eigenvalues of the governing equations when respectively cast into a single system or two reduced-order hyperbolic systems. Hyperbolicity analysis of the present model is conducted in the present chapter as related to typical stratified sediment-laden flows featuring dam-break flows and reservoir turbidity currents. Computational tests for reservoir turbidity currents are also carried out to reveal whether an excessive clear-water outflow would spoil the turbidity current and thus induce the linked Kelvin-Helmholtz instability.

6.2. Eigenvalue Analysis

It is easy to verify that the eigenvalues (w^+ , w^- , s^+ , s^- , λ_s) associated with the

Jacobian matrix of the two reduced-order systems (RS) composed of Eqs. (2.12)- (2.16) if $N = 1$ are given by

$$w^{+} = u_w + \sqrt{gh_w}\ ,\ w^{-} = u_w - \sqrt{gh_w} \tag{6.1a, b}$$

$$s^{+} = u_s + \sqrt{gh_s}\ ,\ s^{-} = u_s - \sqrt{gh_s}\ ,\ \lambda_s = u_s \tag{6.2a, b, c}$$

To evaluate the eigenvalues of the full set of governing equations of the two layers as a single system (SS), the inter-layer interactions terms and variable sediment concentration term are put into the LHS of the non-homogeneous equations. Accordingly, the governing equations of two layers can be rewritten in primitive variables

$$\frac{\partial \mathbf{W}}{\partial t} + \mathbf{A}(\mathbf{W})\frac{\partial \mathbf{W}}{\partial x} = \mathbf{G} \tag{6.3}$$

$$\mathbf{W} = \begin{bmatrix} h_w \\ u_w \\ h_s \\ u_s \\ c \end{bmatrix},\quad \mathbf{A} = \begin{bmatrix} u_w & h_w & 0 & 0 & 0 \\ g & u_w & g & 0 & 0 \\ 0 & 0 & u_s & h_s & 0 \\ \beta g & 0 & g & u_s & 0.5sgh_s \\ 0 & 0 & 0 & 0 & u_s \end{bmatrix} \tag{6.4a, b}$$

$$\mathbf{G} = \begin{bmatrix} -E_w \\ -\tau_w/\rho_w h_w - g\,\partial z/\partial x \\ E_w + (E-D)/1-p \\ (\tau_w - \tau_b)/\rho_c h_s - g\,\partial z/\partial x - \rho_0 (E-D)u_s/\rho_c h_s(1-p) + \rho_w E_w (u_w - u_s)/\rho_c h_s \\ (1-p-c)(E-D)/h_s(1-p) - cE_w/h_s \end{bmatrix}$$

(6.5c)

where $\beta = \rho_w/\rho_c$.

Indeed, the five eigenvalues λ_i $(i = 1,...,5)$ can be computed by $|\boldsymbol{A} - \lambda \boldsymbol{I}| = 0$ ($\boldsymbol{I}$ is the unit matrix) and thus are the roots of the characteristic polynomial below,

$$(\lambda - u_s)[((\lambda - u_w)^2 - gh_w)((\lambda - u_s)^2 - gh_s) - \beta g^2 h_w h_s] = 0 \tag{6.6}$$

From Eq. (6.6), it is easy to calculate one eigenvalue $\lambda_5 = u_s$ which is associated with the sediment continuity equation, i.e., Eq. (2.16). Indeed the exact solutions of the rest four eigenvalues can be obtained analytically. A detailed procedure is described in Lawrence (1990) and a short derivation is given below. Generally two external eigenvalues are always real, while the other two internal eigenvalues may become complex conjugate, which is related to hyperbolicity loss and the Kelvin-Helmholtz instability.

The following quantities are defined: $H = h_s + h_w$ is total flow depth; $\alpha = 4h_w h_s / H$ the depth ratio; $\bar{u} = \frac{1}{2}(u_s + u_w)$ the arithmetic mean velocity; $\hat{u} = (u_w h_s + u_s h_w)/H$ the "hat" velocity; $\varepsilon = \frac{\rho_c - \rho_w}{\rho_c}$ the relative density velocity; $F_w = \frac{u_w}{\sqrt{\varepsilon g h_w}}$ and $F_s = \frac{u_s}{\sqrt{\varepsilon g h_s}}$ are the densimetric Froude numbers of two layers respectively; $G^2 = F_w^2 + F_s^2 - \varepsilon F_w^2 F_s^2$ is the composite Froude number; $F_\Delta^2 = \frac{(u_w - u_s)^2}{\varepsilon g H}$ the stability Froude number.

With the above definitions, the characteristic polynomial may be rewritten:

$$\sum_{m=0}^{4} a_m \lambda^m = 0 \tag{6.7}$$

where $a_0 = u_w^2 u_s^2 - gh_w u_s^2 - gh_s u_w^2 + \varepsilon g^2 h_w h_s = \varepsilon g^2 h_w h_s (1 - G^2)$; $a_1 = -4u_w u_s \bar{u} + 2gH\hat{u}$; $a_2 = 4\bar{u}^2 + 2u_w u_s - gH$; $a_3 = -4\bar{u}$; $a_4 = 1$.

The first step of the solution procedure is reduce Eq. (6.7) by making a substitution of variables, considering an observer moving at the arithmetic mean velocity $\bar{u}$, i.e., $\lambda = y + \bar{u}$, yielding the reduced quartic equation:

$$y^4 + dy^2 + ey + f = 0 \tag{6.8}$$

where $d = \frac{1}{2} gH(2 + \varepsilon F_\Delta^2)$; $e = 2gH(\hat{u} - \bar{u})$; $f = (\frac{1}{4} gH)^2 [4\varepsilon(\alpha - F_\Delta^2) + \varepsilon^2 F_\Delta^4]$.

The four solutions of the reduced quartic equation above are $y_{1,2} = \xi z_1^{1/2} \pm (z_2^{1/2} + z_3^{1/2})$ $y_{3,4} = -\xi z_1^{1/2} \pm (z_2^{1/2} - z_3^{1/2})$. Thus the expressions of the eigenvalues are

$$\lambda_{1,2} = \bar{u} + \xi z_1^{1/2} \pm (z_3^{1/2} + z_2^{1/2}) \tag{6.9a}$$

$$\lambda_{3,4} = \bar{u} - \xi z_1^{1/2} \pm (z_3^{1/2} - z_2^{1/2}) \tag{6.9b}$$

where $\xi = \mathrm{sgn}(u_s - u_w)$, and z_1 , z_2 , z_3 are the solutions of the normalized cubic equation

$$z^3 + rz^2 + sz + t = 0 \tag{6.10}$$

where $r = -(\frac{1}{4} gH)(2 + \varepsilon F_\Delta^2)$, $s = (\frac{1}{4} gH)^2 [1 + \varepsilon(2F_\Delta^2 - \alpha)]$, $t = -\varepsilon(\frac{1}{4} gH)^3 (1 - \alpha) F_\Delta^2$

The solutions of this normalized cubic equation can be obtained through Tartaglia Equation and also depend on the value of its discriminant:

$$D_z = (\frac{1}{3} p)^3 + (\frac{1}{2} q)^2 \tag{6.11}$$

where $p = \frac{1}{3}(3s - r^2)$, $q = \frac{1}{27}(2r^3 - 9rs + 27t)$.

If $D_z \le 0$, z_1, z_2 and z_3 are real and thus the eigenvalues are all real.

If $D_z > 0$, z_1 remains real , but z_2 and z_3 are complex conjugate. Being conjugate, the combination $(z_3^{1/2} + z_2^{1/2})$ remains real also, so that the eigenvalues $\lambda_{1,2}$ are always real. On the contrary, the combination $(z_3^{1/2} - z_2^{1/2})$ is purely imaginary, leading to $\lambda_{3,4}$ that are complex conjugate.

In the analysis below, the five eigenvalues computed by two respective frameworks SS and RS are compared and analyzed. Specifically, the two external eigenvalues λ_1, λ_2 are compared to w_+, w_-, whilst the two internal eigenvalues λ_3, λ_4 are compared to s_+, s_-. And λ_5 matches λ_s as they are both equal to the layer-averaged velocity of the sediment-laden flow layer u_s. This strategy is adopted in all the cases. Besides, a logical parameter Φ is introduced to better describe the hyperbolicity of the present double layer-averaged model. If all the eigenvalues computed by SS are real, then $\Phi =$ 1, meaning hyperbolicity preservation; whilst if two internal eigenvalues are complex conjugate, then $\Phi =$ -1, meaning hyperbolicity loss; besides if double-layer structure does not exist, i.e., either the clear-water layer or the sediment-laden flow layer exists, then $\Phi =$ 0.

Hyperbolicity analysis of the present model is carried out as related to typical experimental cases concerning progressive failure of a single landslide dam (Cao et al. 2011b) and turbidity currents due to sustained inflow (Lee and Yu 2007). For practical applications, computational tests for reservoir turbidity currents are also presented to reveal whether an excessive clear-water outflow would spoil the turbidity current and thus induce the linked Kelvin-Helmholtz instability. All the modelling parameters are kept the same as their counterparts above.

6.3. Progressive Failure of a Single Landslide Dam

Fig. 6.1 presents comparisons of the five eigenvalues computed by RS and SS. The five eigenvalues calculated by SS are all real, indicating the hyperbolicity preservation. λ_5 is always equal to λ_s. At t = 430 s, when the water flows over the top of the dam and starts to erode the toe of the dam [Fig. 3.6(b1)], the difference between λ_1 and w_+ is trivial [Fig. 6.1(a)], but the discrepancies of the other three pairs of mutually compared eigenvalues are discernible [Fig. 6.1(a2-a4)]. When t = 600 s, at the instant clearly characterized by the rather smooth water surface and fully developed sediment-laden flow layer [Fig. 3.6(d1)], the discrepancies between all the four pairs of eigenvalues can be obvious. Even so, the positivity and negativity of the eigenvalues computed by SS and RS at the inlet and downstream are consistent, which demonstrates the consistency of the implementations of the boundary conditions by the two frameworks. The distributions of the logical parameter Φ shown in Fig.6.2 apparently verify the hyperbolicity preservation of the present model equations when applied to this case because the values of the parameter Φ are always displayed as “1” if the double-layer structure exists during the whole process.

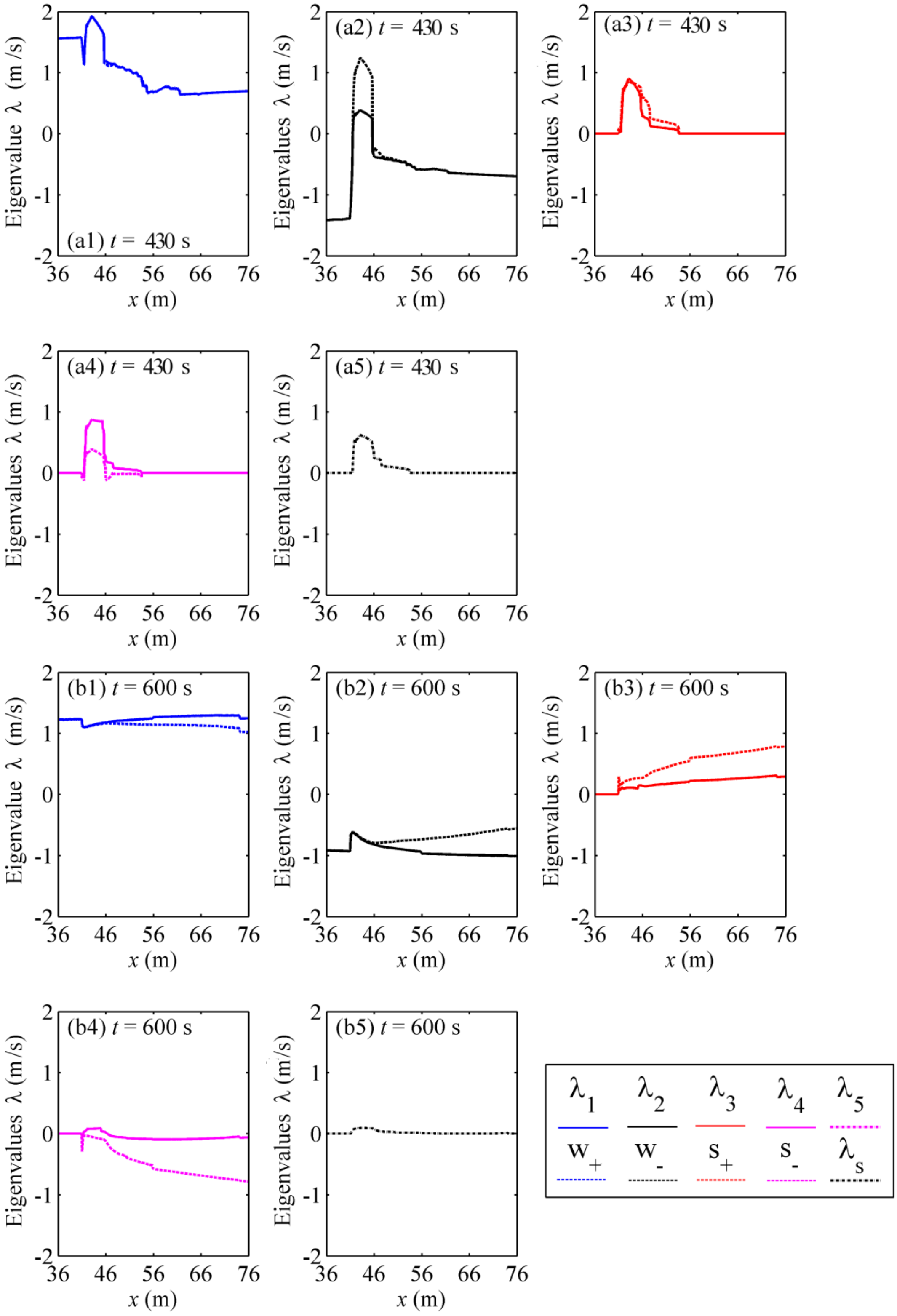

Figure 6.1 Comparisons of the eigenvalues computed by SS and RS

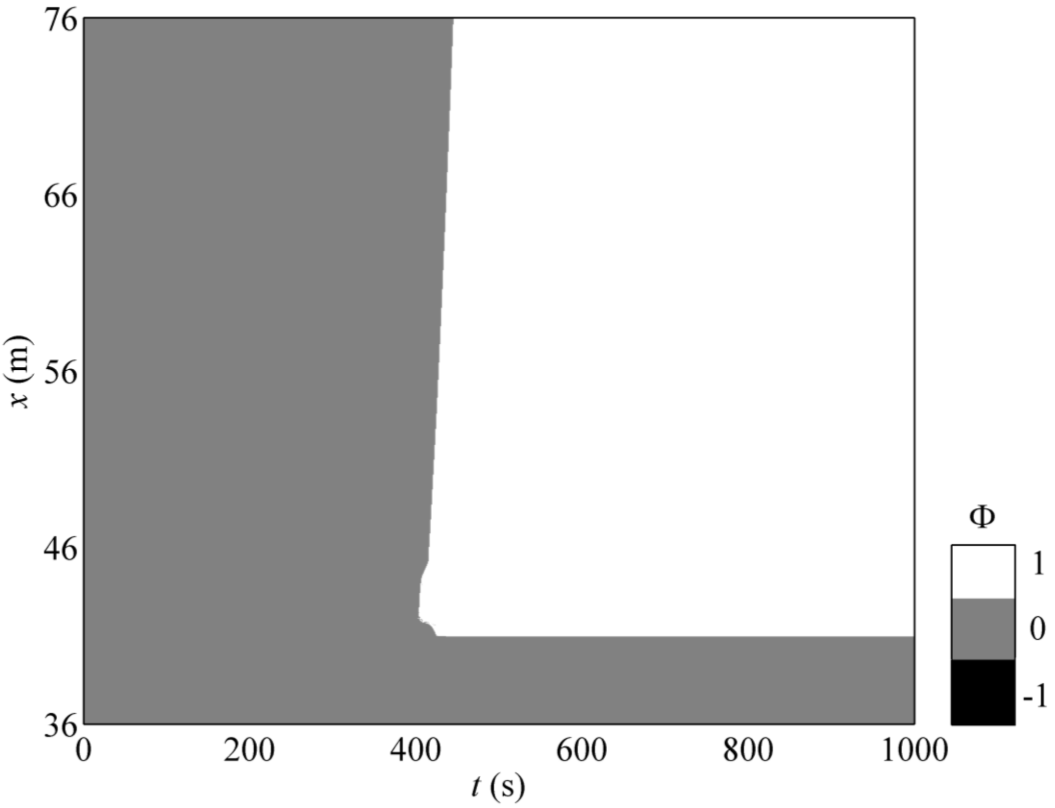

Figure 6.2 Distributions of Φ during the whole process for a single landslide dam failure

6.4. Turbidity Currents Due to Sustained Inflow

When the model is applied to turbidity currents due to sustained flow, the comparisons of the eigenvalues computed by frameworks SS and RS are presented in Fig. 6.3. The five eigenvalues by SS are all shown to be real. Initially the flume is filled with moving clear water, thus only two pairs of the eigenvalues (i.e., λ_1 and w_+, λ_2 and w_-) related to the clear-water flow layer, are not equal to zero and are the same [Fig. 6.3(a1-a5)]. When $t = 25$ s, the turbid water is released from upstream but has not plunged to the bottom. At this stage, the whole flow is divided by a pronounced separation (approximately located 3.68 m from the inlet) into two sections including the open channel sediment-laden flow at the far upstream and the following clear-water flow. After this location w_+ and w_- are the same as λ_1 and λ_2 respectively [Fig. 6.3(b1-b2)], while ahead of this location s_+ and s_- are amount to λ_3 and λ_4 [Fig. 6.3(b3-b4)]. When $t > 450$ s, the plunge point stabilizes and the current advances with a bulge-shaped head and elongated body. Due to the fully developed double-layer structure, the effects of non-conservative products are more profound and thus the discrepancies of the eigenvalues computed by SS and RS frameworks become rather obvious [Fig. 6.3(c1-c4)]. In addition, the positivity and negativity of the eigenvalues computed by SS and RS are the same, indicating that no difference exists between the implementations of the boundary conditions of these two frameworks. Fig. 6.4 illustrates the distributions of Φ during the whole process for the turbidity currents. It is noted that Φ are displayed as "non-negative value" during the whole process, which further corroborates the preservation of hyperbolicity.

Overall the hyperbolicity analysis above demonstrates that the present double layer-averaged model solved by the proposed numerical solution would preserve hyperbolicity and thus avoids exhibiting the linked Kelvin-Helmholtz instability as the eigenvalues generic to SS and RS are all real although the appreciable discrepancies are observed.

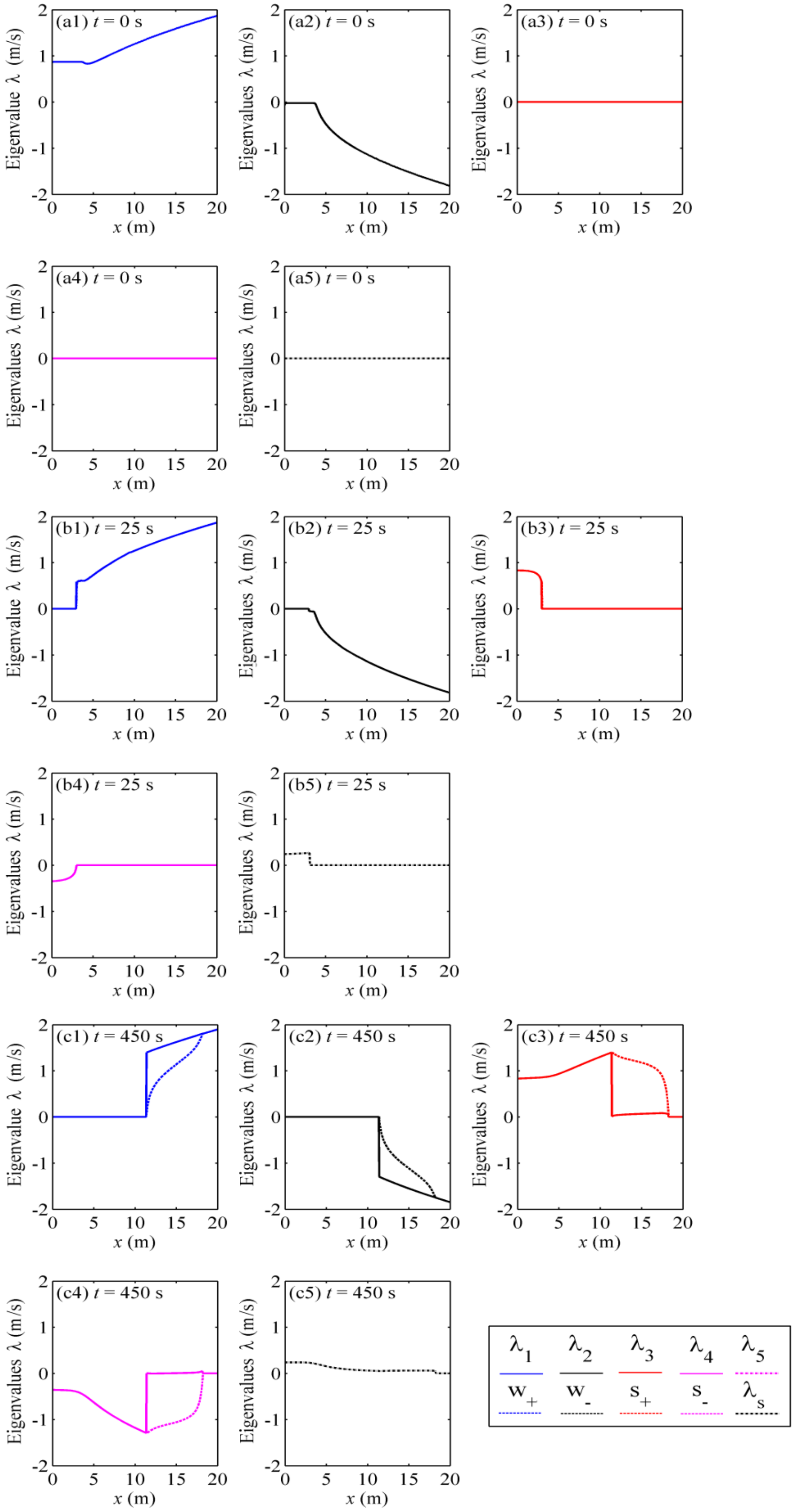

Figure 6.3 Comparisons of the eigenvalues computed by SS and RS for turbidity currents

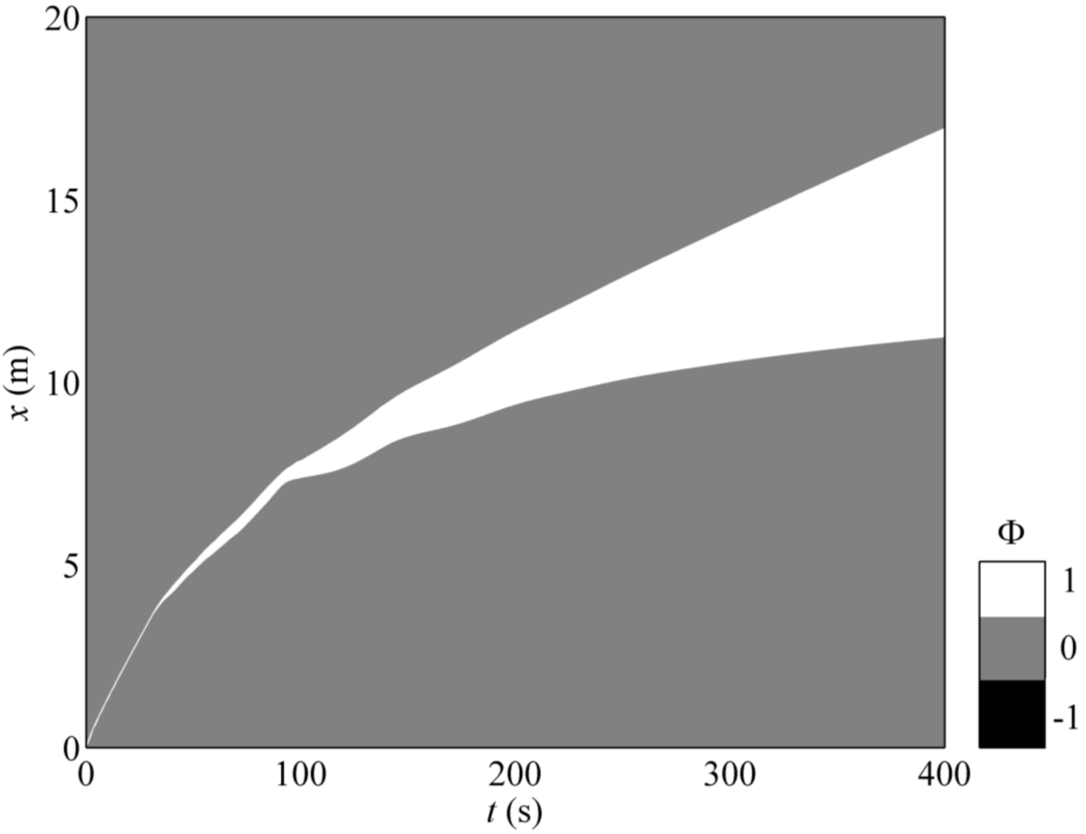

Figure 6.4 Distributions of Φ during the whole process for the turbidity currents

6.5. Implications for Reservoir Operation

It remains to be unraveled if an excessive clear-water outflow would spoil the turbidity currents that have already formed, as a result of Kelvin-Helmholtz instability (Cao et al. 2015). Here the experimental run Series B- PP4 is extended to facilitate the impacts of excessive clear-water outflow on turbidity currents. All the modelling parameters are kept the same as used in Subsection 4.3. It is assumed after the plunge point reaches stable state ($t >$ 4.33 min), the outflow discharge would alter according to the outflow conditions as summarized in Table 6.1. Similar to Subsection 4.3.5, at the outlet, a 4 cm-high bottom outlet on the bed, which has a presumed maximum (unit-width) discharge of 42.55 cm^2/s. The upstream and downstream boundary conditions are determined in a similar way to those in Subsection 4.3.5.

Fig. 6.5 illustrates the turbidity current evolution for Run EC 2, from subaqueous sediment-laden underflow [Fig. 6.5(a)] to open-channel sediment-laden flow [Fig. 6.5(d)]. By t = 250 s, the plunge point reaches a stable state and current advances with a bugle-shaped head and elongated body [Fig. 6.5(a)]. After this stage, the total outflow discharge has doubled (Table 6.1). Due to the increasing outflow along with the subsequent turbidity current venting, the stable plunge point becomes unstable and its location mitigates downstream significantly [Fig. 6.5(b and c)]. More notably, the water level declines sharply. As times goes on, the clear water has been completely drained out, leading to the vanishing of clear-water layer and the appearance of open-channel sediment-laden flow [Fig. 6.5(d)]. Clearly, no interface instability is exhibited during the whole process.

Fig. 6.6 illustrates the distributions of Φ during the whole process for EC 1-4, characterized by gradual growth of outflow discharge. The appearance of non-negative values of Φ clearly indicates hyperbolicity preservation for all these cases and thus demonstrates that the turbidity current would not be spoiled and keeps flow stability when the outflow discharge is increased appropriately. Generally it is suggested increasing outflow discharge appropriately would avoid causing the water body muddy due to the breakdown of turbidity current.

Fig. 6.7 shows the sediment flushing efficiencies for EC 2-5. In general, sediment flushing commences as the turbidity current reaches the bottom outlet, and the flushing efficiency increases with time, which clearly requires sustained inputs of water and sediment from the inlet. And the final efficiency increases greatly along with the growth of outflow discharge. It is also noted that during later stage, specifically when the subaqueous underflow has turned into open-channel sediment-laden flow [see Fig. 6.5(d)], the profiles in Fig. 6.7 indeed represents the sediment flushing efficiency by open-channel sediment-laden flow other than turbidity current. Specifically, the final efficiencies for EC 1-5 are approximately 47%, 52%, 58%, 63% and 70% respectively. Notably the efficiencies have raised 5%, 11%, 16% and 23%, corresponding to the outflow discharge increased by 50%, 100%, 150% and 200%. Physically, the clear-water outflow accelerates the propagation of the turbidity current, which leads to an increase in the amount of sediment flushed out and therefore enhanced sediment flushing efficiency (Cao et al. 2015).

It follows that an excessive clear-water outflow not only keeps the turbidity current from being spoiled (Figs. 6.5 and 6.6), but also is conducive to improving sediment flushing efficiency (Fig. 6.7). This is undoubtedly theoretically and practically critical to develop optimal sediment management schemes for reservoirs worldwide, which suffer from severe sedimentation problems. In a way, it further adds to the current understanding of the effects of distinct reservoir operation schemes on sedimentation mitigation (Fan and Morris 1992a, b).

Table 6.1 Summary of inflow and outflow conditions for extended cases

Run	Inflow discharge q_{in} (cm^2/s)	Sediment Concentration c_{in}	Outflow discharge q_{out} (cm^2/s)
EC 1	q_0	c_0	q_0
EC 2	q_0	c_0	$1.5\,q_0$
EC3	q_0	c_0	$2.0\,q_0$
EC4	q_0	c_0	$2.5\,q_0$
EC 5	q_0	c_0	$3.0\,q_0$

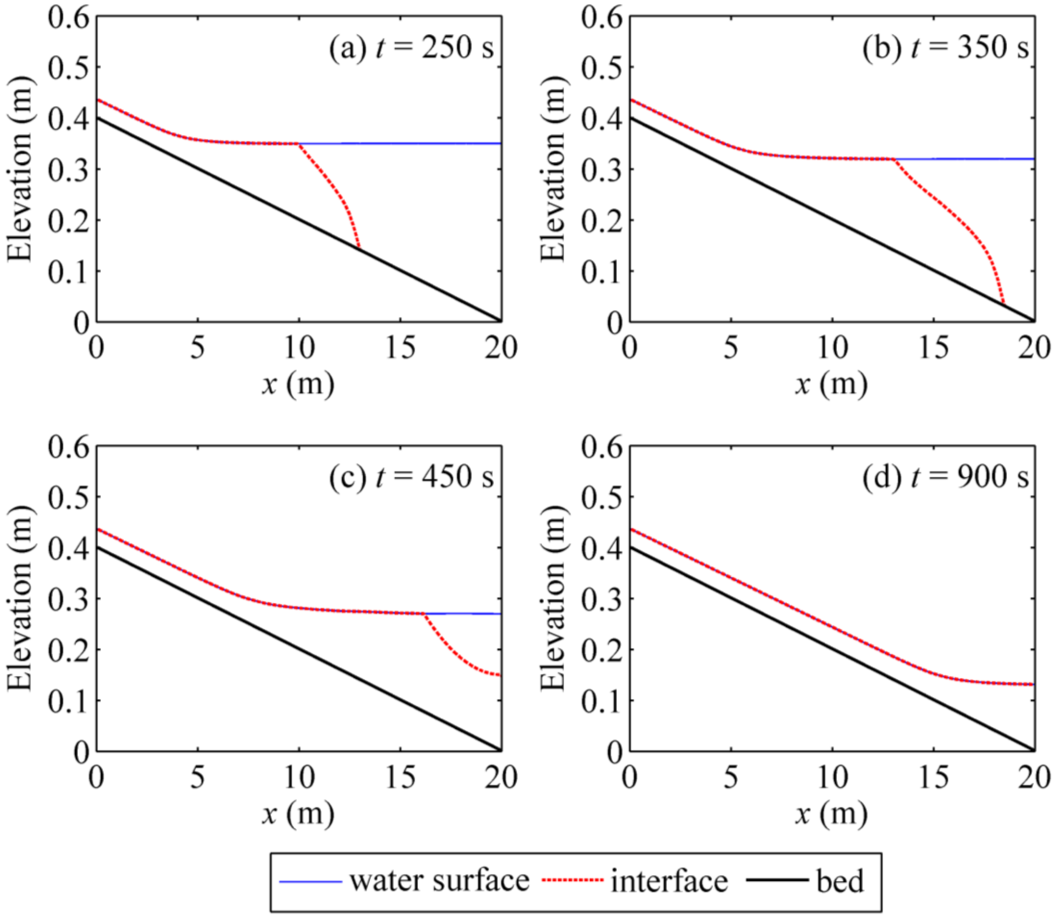

Figure 6.5 Turbidity current evolution (EC 3)

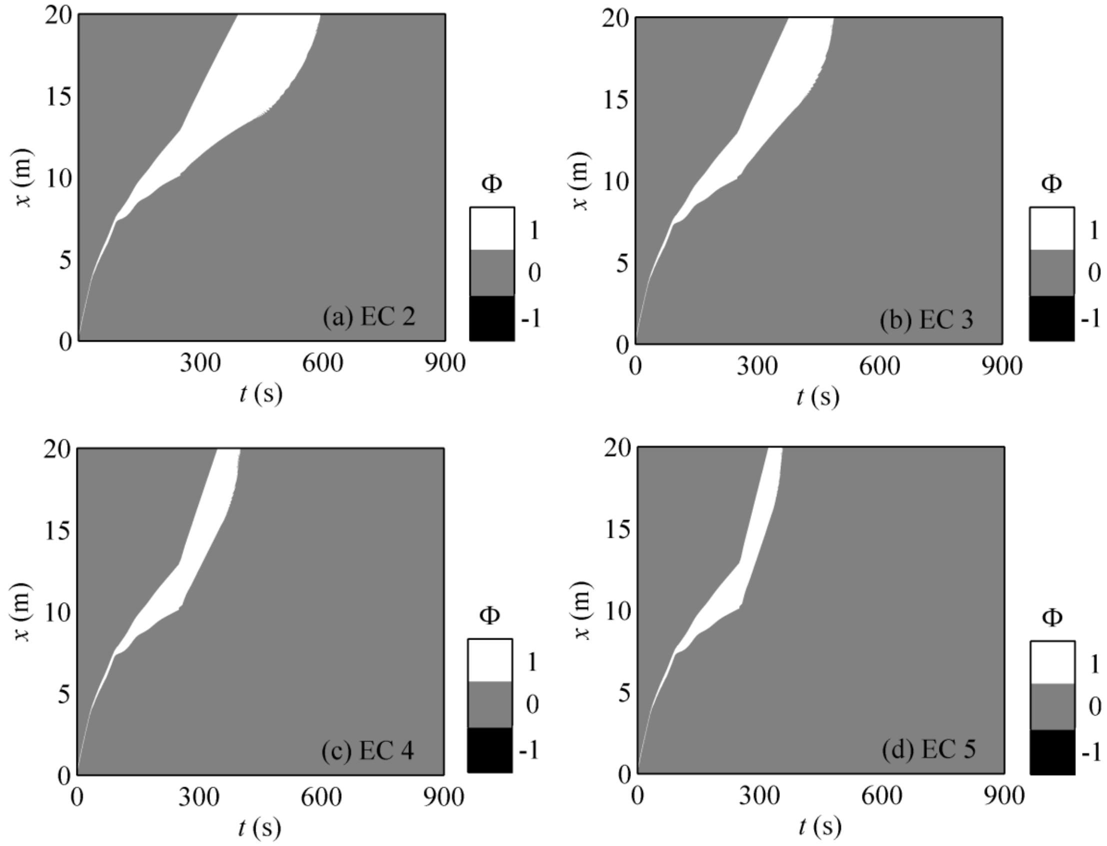

Figure 6.6 Hyperbolicity analysis by distributions of Φ for EC 2-5

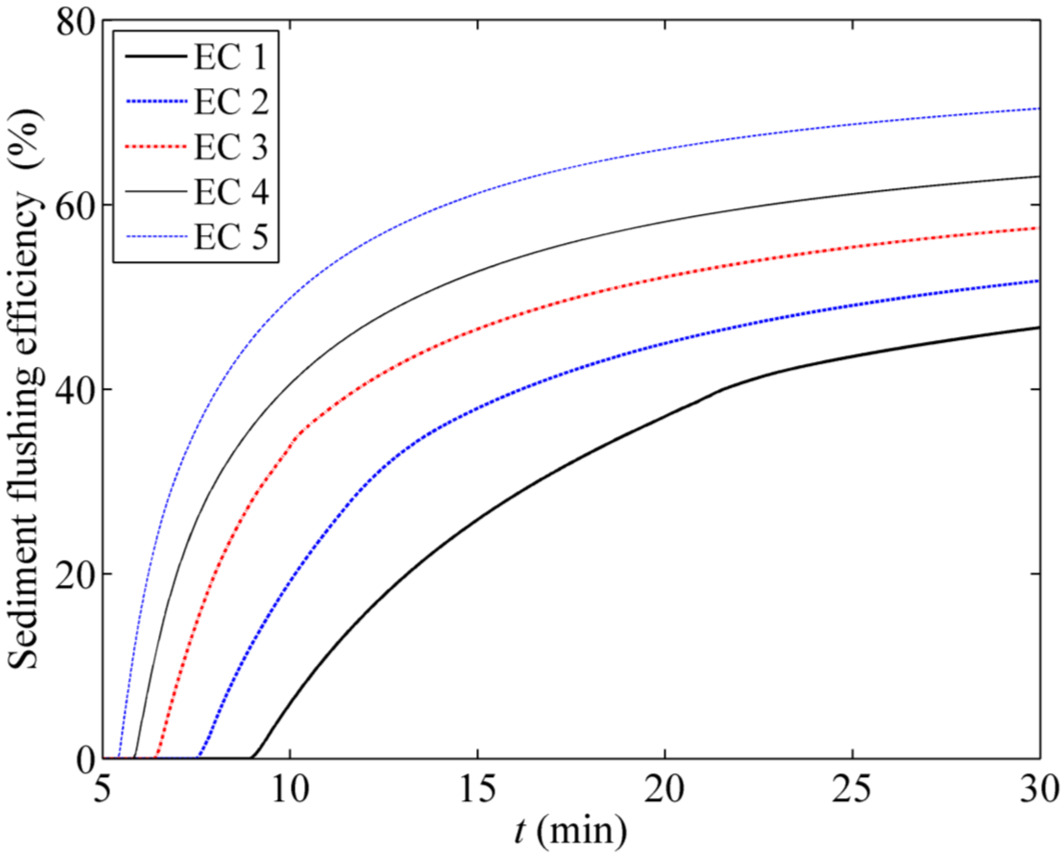

Figure 6.7 Sediment flushing efficiencies for EC 1-5

6.6. Conclusion

The hyperbolicity analysis of the model equations has been conducted by analysing and comparing the eigenvalues of the governing equations when cast into a single system (SS) or two reduced-order hyperbolic systems (RS) respectively. When applied to typical stratified sediment-laden flows featuring dam-break flows and reservoir turbidity currents, the model can preserve hyperbolicity and thus avoid Kelvin-Helmholtz instability as the eigenvalues generic to two frameworks are all real although appreciable discrepancies can be observed. Computational tests for reservoir turbidity currents reveal that an excessive clear-water outflow would keep the turbidity current from being spoiled, and improves sediment flushing efficiency correspondingly. This further adds to the understanding of optimizing reservoir operation schemes.

CHAPTER 7 CONCLUSIONS AND PERSPECTIVES

7.1. Conclusions

Sediment-laden flows in open channels can be sharply stratified vertically, characterized by a vertical double-layer flow structure composed of subaqueous sediment-laden flow layer immediately over the bed and an upper clear-water flow layer. However, existing double layer-averaged models have either partly or completely ignored the primary features of stratified open-channel sediment-laden flows and thus are not generally suitable. In the present thesis, a new coupled two-dimensional double layer-averaged model is developed, explicitly incorporating flow stratification, inter-layer exchange, sediment transport and morphological evolution and thus generally applicable for sharply stratified sediment-laden flow in open channels. The two hyperbolic systems of the governing equations for the two layers are solved separately and synchronously. With this numerical solution, the model is applied to two typical kinds of stratified sediment-laden flows in open channel featuring dam-break flows and reservoir turbidity currents respectively. The hyperbolicity of the model equations is further analyzed as related to dam-break flows and reservoir turbidity currents. The following conclusions are drawn.

- The present work justifies the physical necessity to incorporate the sediment mass conservation in lieu of the assumption of constant sediment concentration generic to previous simplified double layer-averaged models. The present model satisfactorily resolves typical dam-break cases involving the instantaneous full dam break and progressive failure of a single and cascade landslide dams, and features the improved performance over existing models when compared to experimental measurements. In contrast, the simplified double layer-averaged model demonstrates significant sensitivity to the presumed constant sediment concentration. Most notably, when applied to progressive failure of landslide dams, the simplified double layer-averaged model exhibits serious non-physical oscillations and performs rather poorly. Theoretically, the failure of numerical computation arises from the assumption of constant sediment concentration in the lower layer, which essentially breaks the fundamental mass conservation law for sediment and should be eliminated.

- The present model facilitates for the first time the whole-process modelling of reservoir turbidity currents over erodible, irregular bed, i.e., formation, propagation and recession. It has been demonstrated to perform very well when compared to a spectrum of experimental cases, including turbidity currents due to lock-exchange and sustained inflow. It is revealed that an appropriate clear-water outflow is favourable for turbidity current propagation, and also conducive to improving sediment flushing efficiency. This is definitely significant for optimizing reservoir operation schemes. As applied to prototype-scale turbidity currents in the Xiaolangdi Reservoir in the Yellow River, China, the model successfully resolves the whole process from formation to recession and also reproduces the advance of current fairly well. It is found that the turbidity current with multi grain sizes of sediments features faster propagation, more stable plunge point and less sedimentation, as compared to that with single-sized sediment transport. The present work facilitates a viable and promising framework for whole process modelling of turbidity currents, in support of reservoir sediment management.

- The present model is demonstrated to preserve hyperbolicity and thus avoid Kelvin-Helmholtz instability when applied to dam-break flows and reservoir turbidity currents. When the governing equations are cast into a single system (SS) or two reduced-order hyperbolic systems (RS), the eigenvalues generic to these two frameworks are all shown to be real although the appreciable discrepancies can be observed. Computational tests for reservoir turbidity currents reveal that an excessive clear-water outflow would keep the turbidity current from being spoiled, and improves sediment flushing efficiency correspondingly. This further adds to the understanding of optimizing reservoir operation schemes.

7.2. Perspectives

- Uncertainty of the model primarily arises from the estimations of the interface and bed resistances as well as bed sediment entrainment, which are related to the flow evolution and morphological changes. The interface and bed resistances have been approximated by the constant Manning roughness coefficients respectively, which may give rise to uncertainties to some extent. Moreover, the mechanism of sediment entrainment by turbulent flow has so far remained poorly understood although there has been a plethora of empirical relationships available for the determination of sediment entrainment flux. Certainly systematic fundamental investigations of the mechanisms, in relation to boundary resistances as well as bed sediment entrainment in sediment-laden flows, are warranted. Currently, uncertainty can be dealt with by empiricism that can be accrued through practice using more measured datasets.

- The sediment-laden flow layer with high contents of fine sediments may behave as non-Newtonian fluids, featuring the transition and propagation characteristics deviating substantially from the Newtonian fluid. Indeed a plethora of rheological models have been proposed, including power law, viscoplastic, Bingham plastic, Herschel–Bulkley, etc. However, it is very difficult to carry out systematic experiments to verify or test any of these conceptual models, therefore much further work needs to be done in this area before a good scientific understanding is to be obtained (Huppert 2006). Overall the non-Newtonian rheology necessitates the physical enhanced constitutive relationships to be incorporated in the model.

- Technically, the great computational costs can hinder the wide applications of the present double layer-averaged model in prototype-scale domains as a fixed uniform mesh is adopted and a separate continuity equation for each grain size has to be solved. In general, for prototype-scale hydro-sediment-morphodynamics modelling, the need for a high-resolution mesh exists only in a relatively small portion of the entire domain, while a locally coarse mesh suffices over the majority area of the domain. In this regard, the technique of adaptive mesh refining (AMR) can be incorporated, which can greatly save computational time and concurrently maintain the accuracy of the model. These are reserved for future studies.

REFERENCES

Abbott, M. B. (1979). *Computational hydraulics. Elements of the theory of free surface flows*. Pitman, London.

Abgrall, R., and Karni, S. (2009). "Two-layer shallow water systems: a relaxation approach." *SIAM Journal of Scientific Computing*, **31**, 1603-1627.

Adduce, C., Sciortino, G., and Proietti, S. (2012). "Gravity currents produced by lock exchanges: experiments and simulations with a two-layer shallow-water model with entrainment." *Journal of Hydraulic Engineering*, **138**(2), 111-121.

Akiyama, J., and Stefan, H. G. (1984). "Plunging flow into a reservoir: Theory." *Journal of Hydraulic Engineering*, **110**(4), 484-499.

Alavian, V., and Ostrowski, P., Jr. (1992). "Use of density current to modify thermal structure of TVA Reservoirs." *Journal of Hydraulic Engineering*, **118**(5), 688-706.

Altinakar, M., Graf, W., and Hopfinger, E. (1996). "Flow structure of turbidity currents." *Journal of Hydraulic Research*, **34**(5), 713-718.

Amy, L., Hogg, A., Peakall, J., and Talling, P. (2005). "Abrupt transitions in gravity currents." *Journal of Geophysical Research: Earth Surface*, **110**(F3). 1-19.

An, S., and Julien, P. (2014). "Three-dimensional modeling of turbid density currents in Imha Reservoir, South Korea." *Journal of Hydraulic Engineering*, 140(5), 05014004, DOI: 10.1061/(ASCE)HY.1943-7900.0000851.

Armanini, A., and di Silvio, G. (1988). "A one-dimensional model for the transport of a sediment mixture in non-equilibrium conditions." *Journal of Hydraulic Research*, IAHR, **26**(3), 275-292.

Armi, L. (1986). "The hydraulics of two flowing layers with different densities." *Journal of Fluid Mechanics*, **163**, 27-58.

Baas, J., McCaffrey, W. D., Haughton, P. D. W., and Choux, C. (2005). "Coupling between suspended sediment distribution and turbulence structure in a laboratory turbidity current." *Journal of Geophysical Research-Oceans*, **110**(C11), DOI: 10.1029/2004JC002668.

Balmforth, N. J., Von Hardenberg, J., Provenzale, A., and Zammett, R. (2008). “Dam breaking by wave-induced erosional incision.” *Journal of Geophysical Research: Earth Surface*, **113**(F1), 1-12.

Balmfroth, N. J., von Hardenberg J, Zammett R (2009). “Dam-breaking seiches.” *Journal of Fluid Mechanics*, **628**, 1-21.

Bonnecaze, R. T., Huppert, H. E., and Lister, J. R. (1993). “Particle-driven gravity currents.” *Journal of Fluid Mechanics*, **250**, 339-369.

Bonnecaze, R. T., Hallworth, M. A., Huppert, H. E., and Lister, J. R. (1995). “Axisymmetric particle-driven gravity currents.” *Journal of Fluid Mechanics*, **294**, 93-121.

Bouchut, F., and Morales, T. (2008). “An entropy satisfying scheme for two-layer shallow water equations with uncoupled treatment.” *ESAIM: Mathematical Modelling and Numerical Analysis*, **42**(04), 683-698.

Bournet, P. E., Dartus, D., Tassin, B., and Vincon-Leite, B. (1999). “Numerical investigation of plunging density current.” *Journal of Hydraulic Engineering*, **125**(6), 584-594.

Bradford, S. F., and Katopodes, N. D. (1999a). “Hydrodynamics of turbid underflows. I: Formulation and numerical analysis.” *Journal of Hydraulic Engineering*, **125**(10), 1006-1015.

Bradford, S. F., and Katopodes, N. D. (1999b). “Hydrodynamics of turbid underflows. II: Aggradation, avulsion, and channelization.” *Journal of Hydraulic Engineering*, **125**(10), 1016-1028.

Brooks, G. R. and Lawrence, D. E. (1999). “The Drainage of the Lake Ha!Ha! Reservoir and Downstream Geomorphic Impacts Along Ha!Ha! River, Saguenay Area, Quebec, Canada”. *Geomorphology*, **28**(1-2), 141-168.

Cao, Z., and Carling, P. (2002). Mathematical modelling of alluvial rivers: reality and myth. Part II: special issues. *Proceedings of the ICE-Water and Maritime Engineering*, **154**(4), 297-307.

Cao, Z., Li, J., Pender, G., and Liu, Q. (2015). “Whole-process modeling of reservoir turbidity currents by a double layer-averaged model.” *Journal of Hydraulic Engineering*, **141**(2), 04014069.

Cao, Z., Pender, G., Wallis, S., Carling, P. (2004). Computational dam-break hydraulics over erodible sediment bed. *Journal Hydraulic Engineering*, **130**(7), 689-703.

Cao, Z., Yue, Z., and Pender, G. (2011a). “Flood hydraulics due to cascade landslide dam failure.” *Journal of Flood Risk Management*, **4**(2), 104-114.

Cao, Z., Yue, Z., and Pender, G. (2011b). “Landslide dam failure and flood hydraulics. Part I: experimental investigation.” *Natural Hazards*, **59**(2), 1003-1019.

Cao, Z., Yue, Z., and Pender, G. (2011c). “Landslide dam failure and flood hydraulics. Part II: coupled mathematical modelling.” *Natural Hazards*, **59**(2), 1021-1045.

Capart, H. (2000). *Dam-Break Induced Geomorphic Flows and the Transition from Solid- to Fluid-Like Behaviour Across Evolving Interfaces*. PhD Thesis, Université catholique de Louvain.

Capart, H., and Young, D. (1998). “Formation of a jump by the dam-break wave over a granular bed.” *Journal of Fluid Mechanics*, **372**, 165-187.

Capart, H., and Young, D. (2002). Two-layer shallow water computations of torrential geomorphic flows. Proc. Int. Conf. *River Flow* Louvain-la-Neuve, 1003-1012. Balkema, Rotterdam NL.

Castro, M. J., Fernández-Nieto, E. D., González-Vida, J. M., and Parés-Madroñal, C. (2011). “ Numerical treatment of the loss of hyperbolicity of the two-layer shallow-water system.” *Journal of Scientific Computing*, **48**(1-3), 16-40.

Castro, M., Frings, J., Noelle, S., Pares, C., and Puppo, G. (2010). “On the hyperbolicity of two- and three-layer shallow water equations.” Proc. Int. Conf. *Hyperbolic Problems* Beijing, 657-664.

Chen, S. C., and Peng, S. H. (2006). “Two-dimensional numerical model of two-layer shallow water equations for confluence simulation.” *Advance in Water Resources*, **29**(11), 1608-1617.

Chen, Y. H., and Simons, D. B. (1979). “An Experimental Investigation of Hydraulic and Geomorphic Changes in an Alluvial Channel Induced by Failure of a Dam”. *Water Resources Research*, **15**, 1183-1188.

Chen Y. J., Zhou F., Feng Y., and Xia Y. C. (1992). “Breach of a naturally embanked dam on Yalong River.” *Canadian Journal of Civil Engineering*, **19**(5), 811-818.

Chien, N., and Wan, Z. H. (1999). *Mechanics of sediment transport*. ASCE Press, New

York.

Chinnarasri, C., Tingsanchali, T., Weesakul, S., and Wongwises, S. (2003). “Flow patterns and damage of dike overtopping.” *International Journal of Sediment Research*, **18**(4), 301-309.

Choi, S. U. (1998). “Layer-averaged modelling of two-dimensional turbidity currents with a dissipative-Galerkin finite element method. Part I: Formulation and application example.” *Journal of Hydraulic Research*, **36**(3), 339-362.

Coleman, S. E., Andrews, D. P., and Webby, M. G. (2002). “Overtopping breaching of noncohesive homogeneous embankments.” *Journal of Hydraulic Engineering*, **128**(9), 829–838.

Cossu, R., and Wells, M. G. (2012). “A comparison of the shear stress distribution in the bottom boundary layer of experimental density and turbidity currents.” *European Journal of Mechanics B/Fluids*, **32**, 70-79.

Costa, J. E. and Schuster, R. L. (1988). “The Formation and Failure of Natural Dams”. *Geological Society of America Bulletin*, **100**, 1054-1068.

Dade, W. and Huppert, H. (1995). “Runout and fine-sediment deposits of axisymmetric gravity currents.” *Journal of Geophysical Research*, **100**(C9), 18597-18609.

Dai, A., and Garcia, M. H. (2009). “Analysis of plunging phenomena.” *Journal of Hydraulic Research*, **47**(5), 638-642.

Dalton, R. (2010). “Floods linked to San Andreas quakes.” *Nature*, **463**, 16.

Davies, T. R., Manville, V., Kunz, M., and Donadini, L. (2007). “Modeling landslide dam break flood magnitudes: case study.” *Journal of Hydraulic Engineering*, **133**(7), 713-720.

De Cesare, G., Schleiss, A., and Hermann, F. (2001). “Impact of turbidity currents on reservoir sedimentation.” *Journal of Hydraulic Engineering*, **127**(1), 6-16.

De Rooij, F., and Dalziel, S. B. (2009). “Time-and space-resolved measurements of deposition under turbidity currents.” In *Particulate Gravity Currents*, 207-215, Wiley, New York.

Egashira, S. (1980). Basic research on the flow and mechanism of mixing of density-stratified fields. *PhD thesis*, Kyoto University, Japan.

Eggenhuisen, J. T., and McCaffrey, W. D. (2012). “The vertical turbulence structure of experimental turbidity currents encountering basal obstructions: implications for vertical suspended sediment distribution in non-equilibrium currents." *Sedimentology,* **59**(3), 1101-1120.

Fan, J. (1960). "Experimental studies on density currents." *Scientia Sinica*, **9**(2), 275-303.

Fan, J. (1986). "Turbid density currents in reservoirs." *Water International*, 11(3), 107-116.

Fan, J., and Morris, G. L. (1992a). "Reservoir sedimentation. I: Delta and density current deposits." *Journal of Hydraulic Engineering*, **118**(3), 354-369.

Fan, J., and Morris, G. L. (1992b). "Reservoir sedimentation. II: Reservoir desiltation and long-term storage capacity." *Journal of Hydraulic Engineering*, **118**(3), 370-384.

Fan, J., Wang, H., Huang, Y., Wu, D., and Shen, S. (1959). *Studies on density currents and their applications,* Water Resources and Power Press, Beijing, China (in Chinese).

Fang, H. W., and Wang, G. Q. (2000). "Three-dimensional mathematical model of suspended-sediment transport." *Journal of Hydraulic Research*, **126**(8), 578-592.

Fukushima, Y., Parker, G., and Pantin, H. M. (1985). "Prediction of ignitive turbidity currents in Scripps Submarine Canyon." *Marine Geology*, **67**(1-2), 55-81.

Ford, D. E., and Johnson, M. C. (1983). *An assessment of reservoir density currents and inflow processes.* Ford Thornton Norton and Associates LTD, Vicksburs Ms.

Fraccarollo, L., and Capart, H. (2002). "Riemann wave description of erosional dam-break flows." *Journal of Fluid Mechanics*, **461**, 183-228.

Fraccarollo, L., Capart, H., and Zech, Y. (2003). "A Godunov method for the computation of erosional shallow water transients." *International Journal for Numerical Methods in Fluids*, **41**(9), 951-976.

Fraccarollo, L., and Toro, E. F. (1995). "Experimental and numerical assessment of the shallow water model for two-dimensional dam-break type problems." *Journal of Hydraulic Research*, **33**(6), 843-864.

Garcia, M., and Parker, G. (1993). "Experiments on the entrainment of sediment into suspension by a dense bottom current." *Journal of Geophysical Research*, **98**(C3), 4793-4807.

Georgoulas, A. N., Angelidis, P. B., Panagiotidis, T. G., and Kotsovinos, N. E. (2010). “3D numerical modelling of turbidity currents. Environ.” *Fluid Mechanics*, **10**(6), 603-635.

Gladstone, C., Phillips, J. C., and Sparks, R. S. J. (1998). “Experiments on bidisperse, constant-volume gravity currents: propagation and sediment deposition.” *Sedimentology*, **45**(5), 833-844.

Gladstone, C., and Pritchard, D. (2010). “Patterns of deposition from experimental turbidity currents with reversing buoyancy.” *Sedimentology*, **57**(1), 53-84.

Gottlieb, S., and Shu, C. W. (1998). “Total variation diminishing Runge-Kutta schemes.” *Mathematics of Computation of the American Mathematical Society*, **67**, 73-85.

Goutière, L., Soares-Frazão, S., and Zech, Y. (2011). “Dam-break flow on mobile bed in abruptly widening channel: experimental data.” *Journal of Hydraulic Research*, **49**(3), 367-371.

Greco, M., Iervolino, M., Leopardi, A. (2008). “Two-phase depth-integrated model for unsteady river flow.” *Proc. Int. Conf. Hydro-Science and Engineering Nagoya*, 1126-1135.

Guo, J. (2002). “Logarithmic matching and its application in computational hydraulics and sediment transport.” *Journal of Hydraulic Research*, **40**(5), 555-565.

Hallworth, M. A., and Huppert, H. E. (1998). “Abrupt transitions in high-concentration, particle-driven gravity currents.” *Physics of Fluids*, **10**(5), 1083-1087.

Hallworth, M. A., Huppert, H. E., and Ungarish, M. (2003). “On inwardly propagating high-Reynolds-number axisymmetric gravity currents.” *Journal of Mechanic Fluids*, **494**, 255-274.

Hallworth, M. A., Phillips, J., Huppert, H., and Sparks, S. (1993). “Entrainment in turbulent gravity currents.” *Nature*, **362**, 829-831.

Hebbert, B., Imberger, J., Loh, I., and Patterson, J. (1979). “Collie river underflow into the Wellington reservoir.” *Journal of the Hydraulics Division*, **105**(5), 533-545.

Hirano, M. (1971). “River bed degradation with armouring.” *Transactions of the Japan Society of Civil Engineers*, **195**, 55-65 (in Japanese).

Hirsch, C. (1990). *Computational methods for inviscid and viscous flows: Numerical computation of internal and external flows*. Wiley, New York.

Hoey, T. B., and Ferguson, R. (1994). “Numerical simulation of downstream fining by selective transport in gravel bed rivers: Model development and illustration.” *Water Resources Research*, **30**(7), 2251–2260.

Hsu, H. C., Torres-Freyermuth, A., Hsu, T. J., Hwung, H. H., and Kuo, P. C. (2014). “On dam-break wave propagation and its implication to sediment erosion.” *Journal of Hydraulic Research*, **52**(2), 205-218.

Huang, H., Imran, J., and Pirmez, C. (2007). “Numerical modeling of poorly sorted depositional turbidity currents.” *Journal of Geophysical Research*, **112**, 1-15.

Huang, H., Imran, J., and Pirmez, C. (2008). “Numerical study of turbidity currents with sudden-release and sustained-inflow mechanisms.” *Journal of Hydraulic Research*, **134**(9), 1199-1209.

Hu, P., and Cao, Z. (2009). “Fully coupled mathematical modeling of turbidity currents over erodible bed.” *Advance in Water Resources*, **32**(1), 1-15.

Hu, P., Cao, Z., Pender, G., and Tan, G. (2012). “Numerical modelling of turbidity currents in the Xiaolangdi reservoir, Yellow River, China.” *Journal of Hydrology*, **464**, 41-53.

Huppert, H. E. (2006). “Gravity currents: a personal perspective.” *Journal of Fluid Mechanics*, **554**, 299-322.

Huppert, H. and Simpson, J. (1980). “The slumping of gravity currents.” *Journal of Fluid Mechanics*, **99**, 785-799.

Hürzeler, B. E., Imberger, J., and Ivey, G. N. (1996). “Dynamics of turbidity current with reversing buoyancy.” *Journal of Hydraulic Engineering*, **122**(5), 230-236.

Kassem, A., and Imran, J. (2001). “Simulation of turbid underflows generated by the plunging of a river.” *Geology*, **29**(7), 655-658.

Kassem, A., Imran, J., and Khan, J. A. (2003). “Three-dimensional modeling of negatively buoyant flow in diverging channels.” *Journal of Hydraulic Engineering*, **129**(12), 936-947.

Keevil, G. M., Peakall, J., Best, J. L., and Amos, K. J. (2006). “Flow structure in sinuous submarine channels: velocity and turbulence structure of an experimental submarine channel.” *Marine Geology*, **229**, 241-257.

Keevil, G. M., Peakall, J., and Best, J. L. (2007). "The influence of scale, slope and channel geometry on the flow dynamics of submarine channels." *Marine and Petroleum Geology*, **24**, 487-503.

Khan, S. M., Imran, J., Bradford, S., and Syvitski, J. (2005). “Numerical modeling of hyperpycnal plume.” *Marine Geology*, **222**, 193-211.

Kim, J., and LeVeque, R. J. (2008). “Two-layer shallow water system and its applications.” *Proc., Int. Conf. Hyperbolic Problems*, Maryland, 737-743.

Kneller, B. C., Bennett, S. J., and McCaffrey, W. D. (1997). “Velocity and turbulence structure of density currents and internal solitary waves: potential sediment transport and the formation of wave ripples in deep water.” *Sedimentary Geology*, **112**(3-4), 235-250.

Kneller, B. C., Bennett, S. J., and McCaffrey, W. D. (1999). "Velocity structure, turbulence and fluid stresses in experimental gravity currents." *Journal of Geophysical Research-Oceans*, **104**(C3), 5381-5391.

Lai, Y. G., and Wu, K. (2013). “Modeling of turbidity current and evaluation of diversion plans at Shihmen Reservoir in Taiwan.” *World Environment and Water Resources Congress 2013: showcasing the future*, ASCE, 1736-1746.

La Rocca, M., Adduce, C., Sciortino, G., Pinzon, A. B., and Boniforti, M. A. (2012). “A two-layer shallow-water model for 3D gravity currents.” *Journal of Hydraulic Research*, **50**(2), 208-217.

Lawrence, G. A. (1990). “On the hydraulics of Boussinesq and non-Bousinesq two-layer flows.” *Journal of Fluid Mechanics*, **215**, 457-480.

Leal, J. G. A. B., Ferreira, R.M.L. and Cardoso, A.H. (2002). “Dam-Break Waves on Movable Bed”. In: Bousmar, D. and Zech,Y. (eds), *River Flow 2002, Proceedings of the 1st IAHR Institute Conference on Fluvial Hydraulics*, Louvain-la-Neuve, Belgium, Balkema, 981-990.

Leal, J. G. A. B., Ferreira, R. M. L., and Cardoso, A. H. (2006). “Dam-Break wave-front celerity.” *Journal of Hydraulic Research*, **132**(1), 69-76.

Leal, J. G. A. B., Ferreira, R. M. L., and Cardoso, A. H. (2010a). “Geomorphic dam-break flows. Part I: conceptual model.” *Proceedings of the ICE-Water Management*, **163**(6), 297-304.

Leal, J. G. A. B., Ferreira, R. M. L., and Cardoso, A. H. (2010b). “Geomorphic dam-break flows. Part II: numerical simulation.” *Proceedings of the ICE-Water Management*, **163**(6), 305-313.

Lee, H. Y., and Yu, W. S. (1997). “Experimental study of reservoir turbidity current.” *Journal of Hydraulic Research*, **123**, 520-528.

Lee, W. K., Borthwick, A. G., and Taylor, P. H. (2014). “Tracer dynamics in two-layer density-stratified estuarine flow.” *Proceedings of the ICE - Engineering and Computational Mechanics*, **167**(1), 41-49.

Li, G. Y. (2004). “The third test of water and sediment regulation conducted on the Yellow River.” *Yellow River*, **26**(10), 1-8 (in Chinese).

Li, G., Wei, H., Yue, S., Cheng, Y., and Han, Y. (1998). Sedimentation in the Yellow River delta, part II: suspended sediment dispersal and deposition on the subaqueous delta. *Marine Geology*, **149**(1), 113-131.

Li, J., Cao, Z., Pender, G., and Liu, Q. (2013). “A double layer-averaged model for dam-break floods over erodible bed.” *Journal of Hydraulic Research*, **51**(5), 518-534.

Li, T. C., Schuster, R. L., and Wu, J. S. (1986). Landslide dams in south-central China. In: Schuster R (ed) Landslide dams: processes, risk and mitigation. Geotechnical Special Publication No. 3, ASCE, pp 146–162

Li, Y., Zhang, J., and Ma, H. (2011). “Analytical Froude number solution for reservoir density inflows.” *Journal of Hydraulic Research*, **49**(5), 693-696.

Liang, Q. (2010). “Flood simulation using a well-balanced shallow flow model.” *Journal of Hydraulic Engineering*, **136**(9), 669-675.

Macías, J., Parés, C., and Castro, M. J. (1999) Improvement and generalization of a finite element shallow water solver to multi-layer systems. *International Journal of Numerical Methods in Fluids*, **31**, 1037–1059.

Marsooli, R., and Wu, W. (2014). “Three-dimensional numerical modeling of dam-break flows with sediment transport over movable beds.” *Journal of Hydraulic Engineering*, **141**(1), 04014066. Doi: 10.1061/(ASCE)HY.1943-7900.0000947.

Meyer-Peter, E., Müller, R. (1948). "Formulas for bed-load transport." Proc. 2nd *IAHR Congress* Stockholm Appendix 2, 39-64.

Mulder, T., Syvitski, J. P., Migeon, S., Faugeres, J. C., and Savoye, B. (2003). Marine hyperpycnal flows: initiation, behavior and related deposits. A review. *Marine and Petroleum Geology*, **20**(6), 861-882.

Nix, J. (1981). "Contribution of hypolimnetic water on metalimnetic dissolved oxygen minima in a reservoir." *Water Resources Research*, **17**(2), 329-332.

Nourmohammadi, Z., Afshin, H., and Firoozabadi, B. (2011). "Experimental observation of the flow structure of turbidity currents." *Journal of Hydraulic Research*, **49**(2), 168-177.

Özgökmen, T. M., Iliescu, T., Fischer, P. F., Srinivasan, A., and Duan, J. (2007). "Large eddy simulation of stratified mixing in two-dimensional dam-break problem in a rectangular enclosed domain." *Ocean Modelling*, **16**(1), 106-140.

Parker, G. (1991a). "Selective sorting and abrasion of river gravel. I: Theory." *Journal of Hydraulic Engineering*, **117**(2), 113-149.

Parker, G. (1991b). "Selective sorting and abrasion of river gravel. II: Applications." *Journal of Hydraulic Engineering*, **117**(2), 150-171.

Parker, G., Fukushima, Y., and Pantin, H. M. (1986). "Self-accelerating turbidity currents." *Journal of Fluid Mechanics*, **171**, 145-181.

Parker, G., and Toniolo, H. (2007). "Note on the analysis of plunging of density flows." *Journal of Hydraulic Engineering*, **133**(6), 690-694.

Pitman, E. B., and Le, L. (2005). "A two-fluid model for avalanche and debris flows." *Proceedings of the Royal Society A: Mathematical, Physical and Engineering Science*, **363**, 1573-1602.

Pontillo, M., Schmocker, L., Greco, M., and Hager, W. H. (2010). "1D numerical evaluation of dike erosion due to overtopping." *Journal of Hydraulic Research*, **48**(5), 573-582.

Pudasaini, S. P. (2012). "A general two-phase debris flow model." *Journal of Geophysical Research*, **117**, F03010, DOI: 10.1029/2011JF002186.

Qian, N., and Wan, Z. (1983). *Mechanics of sediment transport*. Science Press, Beijing, China.

Richardson, J., Zaki, W. (1954). “Sedimentation and fluidisation: Part 1.” *Transactions of the Institution of Chemical Engineers,* **32**, 35-53.

Rottman, J. W., and Simpson, J. E. (1983). “Gravity currents produced by instantaneous releases of a heavy fluid in a rectangular channel.” *Journal of Fluid Mechanics,* **135**, 95-110.

Rozov, A. L. (2003). “Modeling of washout of dams.” *Journal of Hydraulic Research,* **41**(6), 565-577.

Savage, S. B., and Brimberg, J. (1975). “Analysis of plunging phenomena in water reservoirs.” *Journal of Hydraulic Research,* **13**(2), 187-205.

Savary, C. and Zech, Y. (2007). “Boundary conditions in a two-layer geomorphological model: application to a hydraulic jump over a mobile bed.” *Journal of Hydraulic Research,* **45**(3), 316-332.

Schmocker, L., and Hager, W. H. (2009). “Modelling dike breaching due to overtopping.” *Journal of Hydraulic Research,* **47**(5), 585-597.

Schmocker, L., and Hager, W. H. (2012). “Plane dike-breach due to overtopping: effects of sediment, dike height and discharge.” *Journal of Hydraulic Research,* **50**(6), 576-586.

Sequeiros, O. E., Cantero, M. I., and Garcia, M. H. (2009a). “Sediment management by jets and turbidity currents with application to a reservoir for flood and pollution control in Chicago, Illinois.” *Journal of Hydraulic Research,* **47**(3), 340-348.

Sequeiros, O. E., Cantelli, A., Viparelli, E., White, J. D., García, M. H., and Parker, G. (2009b). “Modeling turbidity currents with nonuniform sediment and reverse buoyancy.” *Water resources research,* **45**(6), W06408, DOI: 10.1029/2008WR007422.

Sequeiros, O., Spinewine, B., Beaubouef, R., Sun, T., Garcia, M., Parker, G. (2010). “Characteristics of velocity and excess density profiles of saline underflows and turbidity currents flowing over a mobile bed.” *Journal of Hydraulic Engineering,* **136**(7), 412-433.

Simpson, J. E. (1997). *Gravity currents in the environment and laboratory*. Cambridge University Press, Cambridge, England.

Singh, B., and Shah, C. R. (1971). “Plunging phenomenon of density currents in reservoirs." *La Houille Blanche,* **26**(1), 59-64.

Spinewine, B. and Zech, Y. (2002). "Dam-Break Waves Over Movable Beds: A 'Flat Bed' Test Case." In: *EC Contract EVG1-CT-2001-00037 IMPACT Investigation of Extreme Flood Processes and Uncertainty, Proceeding 2nd project workshop,* Mo-i-Rana, Norway.

Spinewine B. (2005a). Two-layer flow behaviour and the effects of granular dilatancy in dam-break induced sheet-flow. *PhD Thesis*, Department of Civil Engineering, Université Catholique de Louvain, Belgium.

Spinewine, B. (2005b). Two-layer shallow water modelling of fast geomorphic flows and experimental validation on idealized laboratory dam-break waves. Proc. 31st *IAHR Congress* Seoul 2, 1437–1439.

Spinewine, B., and Zech, Y. (2007). Small-scale laboratory dam-break waves on movable beds. *Journal of Hydraulic Research*, **45**(1), 73-86.

Stone, R. (2008). "Three Gorges Dam: into the unknown." *Science,* **321**, 628-632.

Stoker, J. J. (1957). *Water waves*. Wiley-Interscience, New York.

Sumer, B. M., Kozakiewicz, A., Fredsøe, J., and Deigaard, R. (1996). "Velocity and concentration profiles in sheet-flow layer of movable bed." *Journal of Hydraulic Engineering*, **122**(10), 549-558.

Toro-Escobar, C. M., Paola, C., and Parker, G. (1996). "Transfer function for the deposition of poorly sorted gravel in response to streambed aggradation." *Journal of Hydraulic Research*, **34**(1), 35–53.

Toro, E. F. (2001). *Shock-capturing methods for free-surface shallow flows*. John Wiley & Sons, Chichester.

Ungarish, M., and Zemach, T. (2005). "On the slumping of high Reynolds number gravity currents in two-dimensional and axisymmetric configurations." *European Journal of Mechanics-B/Fluids*, **24**(1), 71-79.

Wong, M., and Parker, G. (2006). "Reanalysis and correction of bed load relation of Meyer-Peter and Muller using their own database." *Journal of Hydraulic Engineering*, **132**(11), 1159-1168.

Wright, L. D., Yang, Z. S., Bornhold, B. D., Keller, G. H., Prior, D. B., and Wiseman, W. J. (1986). "Hyperpycnal plumes and plume fronts over the Huanghe (Yellow River) delta front.” *Geo-Marine Letters*, **6**(2), 97-105.

Wright, L. D., Wiseman, W. J., Bornhold, B. D., Prior, D. B., Suhayda, J. N., Keller, G. H., Yang, Z.-S., and Fan, Y. B. (1988). “Marine dispersal and deposition of Yellow River silts by gravity-driven underflows.” *Nature*, **332**, 629–632.

Wright, L. D., Wiseman, W. J., Yang, Z.-S., Bornhold, B. D., Keller, G. H., Prior, D. B., Suhayda, J. N. (1990). “Processes of marine dispersal and deposition of suspended silts off the modern mouth of the Huanghe (Yellow River).” *Continental Shelf Research*, **10**(1), 1–40.

Wu, W. (2007). *Computational River Dynamics*. Taylor & Francis, London.

Wu, W., Rodi, W., and Wenka, T. (2000). “3D numerical modeling of flow and sediment transport in open channels.” *Journal of Hydraulic Engineering*, **126**(1), 4-15.

Wu, W., and Wang, S. (2007). “One-dimensional modeling of dam-break flow over movable beds.” *Journal of Hydraulic Engineering*, **133**(1), 48-58.

Xia, J., Lin, B., Falconer, R. A., and Wang, G. (2010). “Modelling dam-break flows over mobile beds using a 2D coupled approach.” *Advance in Water Resources*, **33**(2), 171-183.

Yellow River Conservancy Commission (YRCC). (2007). *The Third Test of Water and Sediment Regulation Conducted on the Yellow River*. Yellow River Conservancy Press, Zhengzhou, China (in Chinese).

Zech, Y., Soares-Frazão, S., Spinewine, B., and Grelle, N. (2008). “Dam-break induced sediment movement: Experimental approaches and numerical modelling.” *Journal of Hydraulic Research*, **46**(2), 176-190.

Zech, Y., Soares-Frazão, S., Spinewine, B., Savary, C., and Goutière, L. (2009). “Inertia effects in bed-load transport models.” *Canadian Journal of Civil Engineering*, **36**(10), 1587-1597.

Zhang, R., and Xie, J. (1993). *Sedimentation research in China- systematic selections.* China Water Power Press, Beijing, China (in Chinese).